SCHOOL OF SCIENCE

Department of Industrial Chemistry "Toso Montanari"

Master Degree in

Industrial Chemistry

Class LM-71 – Science and Technology in Industrial Chemistry

Surface characterization of electrosynthesized Nickel Hexacyanoferrate and other Prussian Blue Analogues

Experimental Thesis

CANDIDATE

Francesca Bia

SUPERVISOR

Illustrious Professor Marco Giorgetti

CO-SUPERVISORS

Illustrious Professor Dr. Reinhard Denecke

Dr. Elisa Musella

M. Sc. Thomas Ruf

Academic Year 2018-2019

Abstract

Prussian Blue Analogues (PBAs) are a class of inorganic compounds characterized by a porous, open and three-dimensional framework and that present several important electrochemical properties. In this work, a potentiodynamic protocol was adopted to synthesize nickel hexacyanoferrate films on a porous and low-cost substrate, Ni-foam. Performance of such films on Ni-foam as electrocatalysts in Oxygen Evolution Reaction (OER) was studied and evaluated – as development of cheap yet active OER catalysts is crucial for hydrogen production from the water splitting reaction.

X-Ray Photoelectron Spectroscopy (XPS) was employed to study electrodeposited NiHCF films and a set of PBAs powders, which included both hexacyanoferrates and nitroprussides. This other last piece of work was valuable in finding out interesting features about plausible degradation process and structural differences in PBAs.

Acknowledgments

I wish to thank my supervisor Marco Giorgetti for his help, encouragement and, above all, the opportunities he gave me, such as being an Erasmus student and letting me visit Elettra Synchrotron. I can sincerely say that choosing his “squad” – an inward joke only a few will understand – to carry out this thesis was one of the best decisions I could ever have made and I feel there is no better compliment.

I thank Prof. Denecke for being my co-supervisor, providing me with feedback and, along with the other members of Wilhelm Ostwald Institut, for giving me access to the equipment needed for this work.

I deeply thank Elisa Musella for guiding me from day one and probably teaching me the most about research and work ethic in general. I am grateful I could learn from a person truly willing to teach her interns something valuable everyday.

I also want to thank Thomas Ruf, for being both my supervisor and the wise, fun and reliable boyfriend I have always wanted. Working daily side by side was what made every day of my experience abroad genuinely happy.

I wish to thank all my friends, several of them old, some others found and some others lost, for providing me with much needed distraction, fun and great times together over these five years. Each of you has given me something different which I’ll take with me wherever I go.

A special mention must be done to Diego Grazia, not only for being my friend, but my partner-in-crime, whose wit has never failed to lighten up my day. A “Best of…” book of our shared jokes would be and shall be endless.

Last but not least, I want to thank my parents, Alberto and Luana, for supporting me unconditionally and being the warm, loving and safe family nucleus I always long to return to and which I desire to create for myself in my life.

Contents

Chapter 1
Introduction

1.1 Prussian Blue

Accidentally first synthesized by Heinrich Diesbach at the very beginning of XVIII's century [1], Prussian Blue, also named ferric ferrocyanide, would make history not only as an inorganic pigment but also as the base pillar for research about its analogue compounds. Aside from its color, Prussian Blue's key characteristic is represented by its open, zeolitic-type structure, first investigated and discussed by Keggin and Miles in 1936 by means of X-ray diffraction [2]. Prussian Blue has a face-centered cubic structure where Fe^{III} and Fe^{II} alternate and are linked by cyanide, which acts like a bridge between the two iron atoms. Both are octahedrically coordinated, Fe^{II} to carbon and Fe^{III} to nitrogen. The resulting structure is therefore composed of repeating Fe^{II}-C≡N-Fe^{III} chains with a cell lenght of approximately 10.2 Å [2].

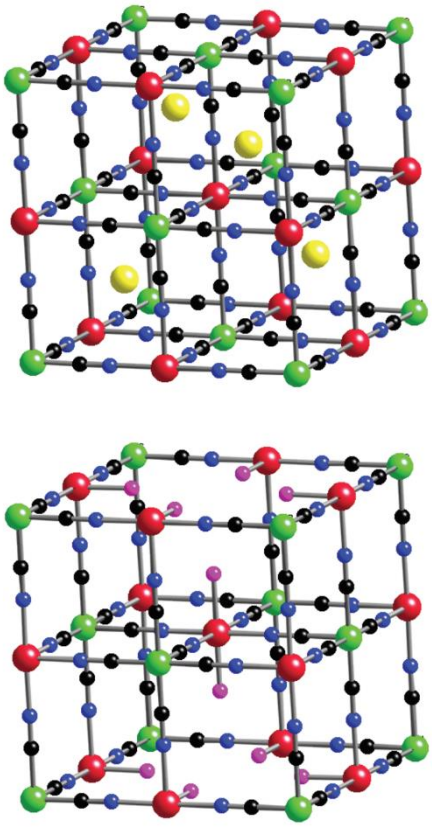

Figure 1 - Structures of soluble Prussian Blue (up) and insoluble Prussian Blue (down). Legend: Fe^{II} (green), Fe^{III} (red), K^+ (yellow), C (black), N (blue), water O (purple) [4]

The characteristic intense blue colour of Prussian Blue is due to the mixed-valence nature of the compound and originates from the charge transfer between the Fe^{II} and Fe^{III} centres [3].
It must be noted that there are two forms of Prussian Blue, *soluble* and *insoluble*. The former has stoichiometric formula $KFe^{III}[Fe^{II}(CN)_6]$, while the latter is $Fe_4[Fe(CN)_6]_3$. Such definitions are not related to actual solubility in water, since both are insoluble, but they refer to the ease in peptization of the two compounds. While the structure revealed by Keggin and Miles successfully describes soluble Prussian Blue's, insoluble Prussian Blue was investigated later in detail by Ludi et al. [4], still with the aid of X-ray diffraction. Insoluble

Prussian Blue lacks some $[Fe(CN)_6]^{4-}$ units, resulting in a different stoichiometry and their replacement by water molecules. Figure 1 [5] shows Prussian Blue's two possible structures. Independently of the considered form, Prussian Blue's lattice has plenty of cavities and vacancies that can be occupied by ions or water molecules. Its density (1.8 g/cm^3, [4]) is exceptionally low indeed in comparison to other iron salts (higher than 3 g/cm^3) [1]. Such feature is at the basis of Prussian Blue's host-guest chemistry, upon which several fascinating applications can be developed. One remarkable example is the use of Prussian Blue as an antidote against Tl^+ poisoning: Tl^+ would replace K^+ in its lattice and become irreversibly trapped [1]. Prussian Blue's valuable medical aid has gained it a place in World Health Organization (WHO) Model List of Essential Medicines [6].

1.2 Metal Hexacyanoferrates

Prussian Blue is just one of the many compounds belonging to the metal hexacyanometallates class. They are characterized by the general stoichiometric formula [7]:

$$A_hM_k[B(CN)_6]_l \times mH_2O$$

where A is an alkali metal cation, M and B are transition metal ions and h, k, l and m are stoichiometric numbers. In case B is represented by Fe, the formula $A_hM_k[Fe(CN)_6]_l \times mH_2O$ describes metal hexacyanoferrates structure. They are also referred to as Prussian Blue Analogues (PBA), as Prussian Blue, being iron (III) hexacyanoferrate(II), is this class' prototype compound.

Up to date, several forms of metal hexacyanoferrates have been synthesized: copper [8], palladium [9], indium [10], vanadium [11], nickel [12], cobalt [13], titanium [14], platinum [15], manganese [16] and zinc [17]. Rare earth metals hexacyanoferrates have also been synthesized and studied [18][19][20]. In addition to them, the syntheses of mixed hexacyanoferrates have also been reported, such as Cu/Co [21], Ni/Co [22] and Ni/Pd [23].

Synthesis of metal hexacyanoferrates can be achieved either chemically – mainly by simple, scalable and low cost bulk co-precipitation methods [24] – or electrochemically, upon an electrode substrate. It is possible to modulate Fe or M's oxidation state through a precise synthetical route [3] and that is why many compound stoichiometries, each determined by a specific M:Fe ratio, can exist for a given analogue [7].

All analogues have in common the open-framework lattice structure already discussed with Prussian Blue, formed by -N≡C-Fe^{II}-C≡N-$M^{III/II}$- atomic chains in a repetitive fashion. In these compounds Fe^{II} (d^6) is always low spin, while M can be either high or low spin. They also possess a certain flexibility due to the stretching and vibrational modes of the cyanide ligand, which, acting like a bridge, can mediate metal to metal charge transfer [25] through a π-back-bonding mechanism - removing charge from the C terminal and transfer it to the N end [26].

Metal hexacyanoferrates present several properties, among which electrochemical [27][28][29], magnetic [25] and electrochromic [11]. The feasible applications will be discussed in Section 1.3.

1.2.1 Metal nitroprussides

Another class of analogues is represented by metal nitroprussides (MNP). The basic structure of nitroprussides derives from the pentacyanonitrosylferrate(II) anion, $[Fe(CN)_5NO]^{2-}$ [30]. A transition metal ion still coordinates to the N end of the -CN group. The main structural difference from hexacyanoferrates is, therefore, the substitution of one cyanide with a nitrosyl group. Nitrosyl is a so-called "non-innocent" ligand, meaning that its oxidation state when bound to a metal complex is not clear. In fact, nitrosyl can undergo a series of chemical reduction reactions, which change both its geometry and its coordination state, as can be seen in Figure 2. [31]

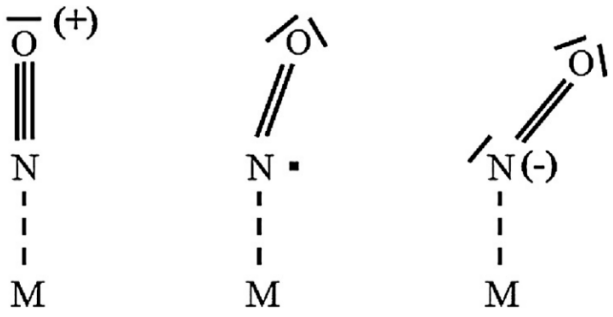

Figure 2 - Lewis structures of nityrosyl group as it undergoes reduction reactions while coordinated to M [31]

This feature is important whenever electrochemical studies or applications are involved. Redox states – and therefore geometry – can be differentiated by means of infrared (IR) spectroscopy, since linear M-NO absorbs at 1930-1950 cm^{-1} and bent M-NO at 1400-1700

cm^{-1} [31]. Also, nitrosyl does not act like a bridge between the two metal centers, resulting in more porous lattice structures.

The most relevant compound belonging to this family is sodium nitroprusside, $Na_2[Fe(CN)_5(NO)]$, usually dihydrate. Its iron atom is in a +2 oxidation state and octahedrically coordinates the five cyanides and the nitrosyl ligands. Sodium nitroprusside has been found to exist in two different structures, one with an isonitrosyl and the other with a bent nitrosyl [32], [33]. As with Prussian Blue, sodium nitroprusside is widely used as medication to treat hypertensive crises. Once in the body, the release of nitrosyl as nitric oxide causes dilatation of blood vessels, lowering blood pressure. It is found, again, in WHO's Model List of Essential Medicines [6].

1.2.2 Nickel Hexacyanoferrate

Nickel hexacyanoferrate (hereby abbreviated NiHCF) is an analogue of particular interest, having been studied extensively along with cupric hexacyanoferrate. It gained attention for being very effective in the removal and immobilization of radionuclide ^{137}Cs from wastewaters and it is a candidate material for ESIX (Electrochemically Switched Ion Exchange) [3], a promising technology for environmental purposes.

NiHCF can be synthesized either chemically or electrochemically, as previously stated. Chemical synthesis involves bulk co-precipitation, either directly pouring one Ni^{II} salt solution into a ferricyanide one (or the opposite) or by mixing them in a dropwise mode. The resulting structures are mostly non-stoichiometric, presenting a Ni:Fe molar ratio with $1 \leq Ni \leq 2$ in regards to iron [34]. Lattice non-stoichiometry resulting from bulk synthesis methods can be adapted to thin film synthesis [35].

However, thin films are mainly synthesized by electrochemical deposition. A variety of electrochemical deposition protocols can be found in literature [36]–[40]. A traditional strategy involved the use of nickel metal surfaces as substrate and their consequent oxidation to produce Ni^{II} ions that would supposedly react with $[Fe(CN)_6]^{3-}$ or $[Fe(CN)_6]^{4-}$ in solution [12]. Nevertheless, cathodic deposition is chosen instead in more recent papers: both potentiodynamic and potentiostatic procedures are encountered. Zamponi et al. [41] investigated the effect of experimental conditions on the resulting NiHCF structure: it was concluded that potentiodynamic methods provided a K^+-rich structure, assumed as

$KNi[Fe^{III}(CN)_6]$, while the application of a constant potential – especially for long times – resulted in a Ni-rich structure, $Ni_{1.5}[Fe^{III}(CN)_6]$. They also hinted that both structures were actually deposited. Such assumption can be made whenever solid mixtures are synthesized, independently of the synthetical route.

NiHCF has a cubic structure with -Ni-N≡C-Fe- linear atomic chains and cell length *a* between 10.1 Å and 10.4 Å according to Loos-Neskovic et al. [42]. Bulk-synthesized NiHCF belongs to the *Fm-3m* space group [42],[43]. Cathodically deposited NiHCF thin films were analyzed by means of XRD and EXAFS by Steen et al. [44] and they concluded that their structure resembles better "insoluble" Prussian Blue's and falls in *Pm-3m* group (in contrast with bulk NiHCF). While Fe^{II} is ochtaedrically coordinated to six carbon atoms, the average Ni coordination number is between 4.4 and 5.1 – overall, the structure is less rigid than expected. Lattice parameter also increases proportionally to intercalated cation size.

While Fe^{II} is electroactive, Ni^{II} is electrochemically inert in NiHCF [45].

1.3 Prussian Blue Analogues' applications

Prussian Blue Analogues, like Prussian Blue itself [29], show considerable electrochemical activity. Such feature is usually attributed to the reversible Fe^{III}/Fe^{II} redox couple, yet the other present transition metal may react and change its oxidation state as well, e.g., Cu is electroactive in copper hexacyanoferrate [46], as Ti is in titanium hexacyanoferrate [14].
As either M or Fe or both are oxidized and reduced, alkali metal cations in the solution leave or enter the lattice respectively to maintain net charge neutrality in the material. This feature has been studied extensively for application in ion sensors and ion exchange, especially for non-electroactive toxic cations such as Tl^+ and Cs^+ [3].
In the last few years, many studies have focused on the application of PBAs as battery materials, especially in rechargeable Sodium Ion Batteries (SIBs). PBAs present a variety of advantages, from their rigid open framework – which is unaffected by ion insertion processes – to the affordable and simple synthesis method. Electrochemical properties of the material can be also easily tuned, for example by choosing a specific combination of transition metals. [45]

PBAs-based biosensors and transducers have also been developed due to the materials' electrocatalytic activity. Karyakin reported several examples, including sensors for H_2O_2 and glucose [29].

In addition, PBAs display electrochromic properties. Electrochromism is the change of color in a material when a voltage is applied and it is an important feature in the development of displays. Cobalt hexacyanoferrate showed significant electrochromic behavior, which was also found to be electrolyte-depending [47]. Vanadium hexacyanoferrate films are electrochromic, changing from yellow to green when oxidized [11].

PBAs, finally, have also been studied for hydrogen storage [48][26] and for wastewater remediation [3].

1.4 X-Ray Photoelectron Spectroscopy

X-Ray Photoelectron Spectroscopy (XPS) or ESCA – an acronym that stands for Electron Spectroscopy for Chemical Analysis - is a surface-sensitive spectroscopic technique. It is based on the photoelectric effect, which describes a surface emitting electrons when illuminated by an incident beam of light [49].

In the case of XPS, the surface is irradiated by an incident X-Ray beam with a known definite energy, which excites the constituting atoms and subsequently causes ejection of photoelectrons. With relatively high probability, core electrons - the closest to the atom's nucleus - are expelled, creating a core hole (Figure 3). The atom is thus ionized and the emitted so-called "primary electrons" are analyzed with respect to their kinetic energy and detected. Photoelectron lines are named according to their total momentum ($J = l \pm s$), where l = 0,1,2,3 - denoted as s,p,d,f - and $s = \pm 1/2$, quantum numbers of the core energy level from which the photoelectrons are expelled. e.g. Fe $2p_{3/2}$ where $3/2 = 1 + ½ = l + s$. [49]

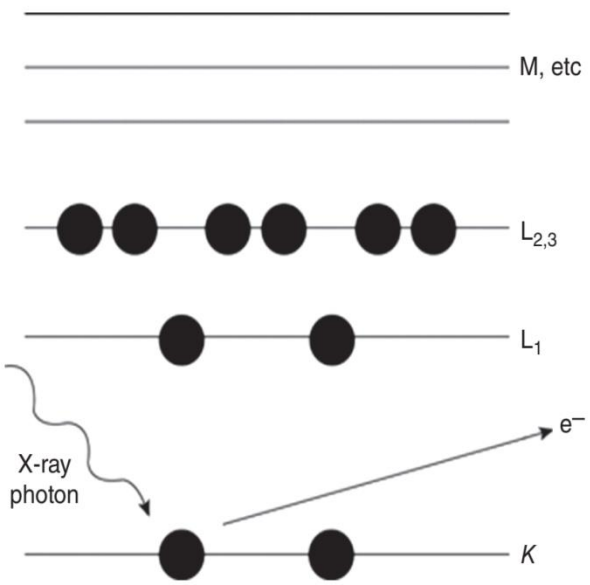

Figure 3 - Ejection of a 1s electron and formation of a core hole after photoionization by a X-Ray photon [50]

Since the electrons travel harder in matter, they have a generally low mean free path (modeled by a so-called "universal curve", which relates mean free path to kinetic energy of electrons) of approximately 10 Å-20 Å because of strong interaction with matter, only the topmost atomic layers are probed. The escaping photoelectron has a specific kinetic energy E_K, which can be calculated as follows: [51]

$$E_K = h\nu - E_B - \Phi \qquad [1]$$

In such formula, $h\nu$ is the X-Ray's energy, E_B is the electron's binding energy and Φ is the spectrometer's work function.

E_B is a characteristic energy value for a certain orbital of a certain element. Therefore, the binding energy is an element-specific parameter and provides qualitative composition of a sample. Generally speaking, the more closely bound an electron, the higher its corresponding E_B and, according to Equation 1, the less kinetic energy it has after ejection.

Aside from elemental analysis, it is also possible to probe the actual chemical species present by checking the peak signal's chemical shift. Chemical shift is a change in core-level binding energy value for an atom in a certain environment as a result of the changed electron density in the valence electrons.

Therefore, the usual information that can be gained by XPS analysis is:

- elemental identity
- chemical oxidation state via chemical shift

It is also possible to evaluate the amount of the various specimens through quantitative analysis of peaks. Assuming that the sample is homogeneous, there is a correlation between the intensity of a peak and the number of atoms sampled [49]:

$$I = nf\sigma\theta y\lambda AT \quad [2]$$

Where

- I is the peak intensity, in photoelectrons/second
- n is the number of atoms - of the analyte element - per cm^3 in the sample
- f is the X-Ray flux, in photons/cm^2 • sec
- σ is the photoelectric cross-section for the atomic orbital of interest in cm^{-2}
- θ is the angular efficiency factor for the instrument
- y is the efficiency of the photoelectric process
- λ is the IMFP (Inelastic Mean Free Path) of a photoelectron
- A is the area of the analyte sample in cm^2
- T is the detection frequency

It must be kept in mind that the quantitative analysis results represent only the sample's surface. To probe the inner layers of the sample, sputtering is employed. Sputtering involves bombardment of the surface via inert ions such as Ar^+.

XPS analysis is carried out in Ultra High Vacuum (UHV, 1×10^{-9} Torr) for plenty of experimental reasons. First, UHV is required to ensure a sufficient inelastic mean free path for the photoelectrons escaping the solid and to minimize the dissipation of energy via inelastic scattering. Low pressures (10^{-7} Torr) are also needed to operate the X-Ray anode and filaments without damage. They are also necessary to minimize surface contamination from the gases present in the analysis chamber [49].

Samples are usually fixed on carbon tape placed on a metallic sample holder, in order to provide conductivity. Despite this, specimen charging phenomena occur nevertheless.

1.4.1 Extrinsic and intrinsic energy loss processes

It should be mentioned that primary electrons can experience energy losses through specific processes, known as “shake-up” and “shake-off”. In case of a shake-up process, the photoelectron interacts with an outer shell valence electron and promotes it to a higher energy level, hereby losing some of its original kinetic energy. The resulting photoelectron line is situated at a slightly higher binding energy than the present line, giving rise to a satellite. If the photoelectron transfers enough kinetic energy to the valence electron to cause its emission, shake-off occurs. Again, the resulting line is located at higher binding energy as a satellite to the main line. [52]

Plasmon peaks are structures arising from photoelectrons’s energy losses as well. In this case though, peaks are situated at 20-25 eV above the primary photoelectron lines and are deemed mostly extrinsic. This phenomenon may happen when analyzing metal surfaces [51].

Another process that must be taken into consideration is multiplet splitting. Multiplet splitting arises whenever an atom, in a given oxidation state, contains unpaired electrons [51]. After photoionization, the unpaired core electron may couple with the outer shells’ unpaired electrons. This leads to a number of possible final states, which are detected in the spectrum as multi-peaks structures. Multiplet splitting is very common when transition metal atoms are analyzed.

Inelastic scattering, secondary electrons and collision give rise to a step-like background at the photoelectron lines, which increases from lower to higher binding energies. [51]

1.4.2 Relaxation processes after photoionization

When an electron core hole has been created, the atom is unstable. In order to stabilize, two competitive processes may occur (Figure 4) :

- X-Ray fluorescence: an electron from an outer shell fills in the vacancy, emitting a photon whose energy is equal to the difference $|E_n-E_0|$, where *n* is the outer energy level. When examining this characteristic radiation, the associated technique is X-Ray Fluorescence (XRF) Spectroscopy. [49]

- Auger effect: it is a two-electron process, in which upon relaxation of an outer electron into the inner core hole, a different outer electron is ejected. Such electron is a

secondary electron and the overall process leaves the atom doubly ionized, yet in a more stable state. The kinetic energy of the Auger electron is totally independent of incident *hv* and depends exclusively on the energy difference between the involved atom shells. An Auger line can thus be identified by these atomic orbital shells in a three-letter code: the first letter refers to the orbital from which the photoelectron is ejected (K in Figure 4), the second to the orbital of the decaying outer electron (L_1) and the third and last one to the orbital losing an electron ($L_{2,3}$). Auger lines are recorded anytime an XPS experiment is running. Due to normalization to the excitation energy, the position of Auger lines changes when a different X-Ray source is selected and overlapping with primary photoelectric lines has to be considered. [49]

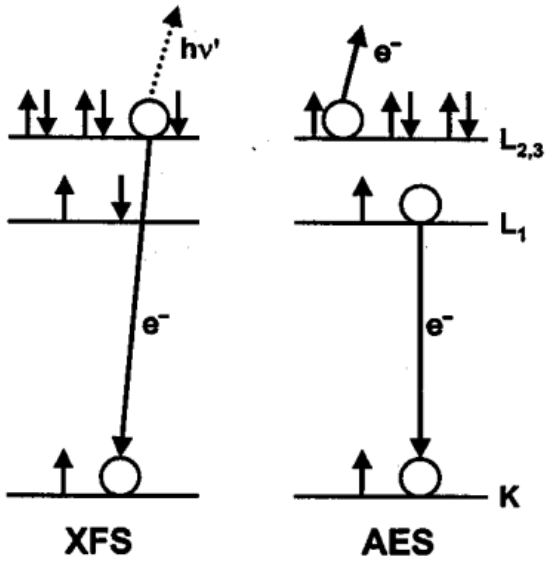

Figure 4 - Schemes of X-Ray Fluorescence and a KLL Auger phenomena [49]

Fluorescence is more likely for heavier elements (Z>25), whereas Auger effect is more probable for lighter elements [50].

1.5 Cyclic Voltammetry

Cyclic voltammetry (CV) is an electroanalytical technique useful to characterize the electrochemical behavior of a certain species or material, determine the potential (*E)* at which oxidation or reduction occur and state whether such reactions are reversible or not [53].

Cyclic voltammetry is similar to linear sweep voltammetry (LSV), where a defined potential area is investigated at a certain scan rate *v* in a given direction starting from a precise initial potential E_0. However, while LSV is a one-segment experiment, in CV a reverse scan begins

immediately after – therefore, completing one full cycle. Current peaks are usually seen when electrochemical reactions take place. Their intensity is related to the operating scan rate by the Randles-Sevcik equation, valid for a reversible system at T = 25 °C [53]:

$$I_p = (2.69 \times 10^5) n^{3/2} A D_O^{1/2} C_O^* v^{1/2} \quad [3]$$

where:

- I_p is the peak current, in A
- n is the stoichiometric number of electrons taking part in the electrode reaction
- A is the area of the electrode in cm^2
- D_O is the diffusion coefficient of species *O*, in cm^2/s
- C_O^* is the bulk concentration in the solution of species O, in mol/cm^3
- v is the linear scan rate, in V/s

When electroactive layers are being analyzed, I_p is directly proportional to *v* [53].
Equations concerning the peak potential E_p are also important [53]:

$$|E_p - E_{p/2}| = 2.20 \times RT/nF = 56.5/n \text{ mV at 25 °C} \quad [4]$$

where:

- $E_{p/2}$ is the half-peak potential
- R is the universal gas constant, measured in J/mol×K
- T is the temperature, in K
- F is the Faraday constant, e.g the charge on one mole of electrons, in C
- n is the stoichiometric number of electrons involved in the reaction

In a reversible system, the potential E_p does not depend on the current, on the scan rate or the concentration of the analyte in solution – it is therefore a specific value for the studied reaction and representative of the thermodynamics of the studied system.

1.6 Oxygen Evolution Reaction

Oxygen Evolution Reaction (OER), also referred to as “water oxidation”, is one of the two reactions – the other one being HER, Hydrogen Evolution Reaction - involved in water

splitting. Water splitting represents an efficient, clean and renewable way to produce H_2, which is deemed as a promising energy source to substitute fossil fuels. While at the cathode HER occurs, at the anode OER, the complementary reaction, proceeds [54].

OER may happen both in acidic (Reaction 1, [55]) and alkaline (Reaction 2, [56]) media, yet the mechanism is different:

1) $2H_2O \rightarrow 4H^+ + 4e^- + O_2$
2) $4OH^- \rightarrow 2H_2O + O_2 + 4e^-$

A pH dependence of OER is nevertheless clear. OER studies are often carried out in alkaline conditions since many OER catalysts – mainly oxides and hydroxides – are chemically stable, whereas they are not in acidic solutions [57].

A major challenge in the development of this technology is finding highly-performing and stable OER catalysts indeed. That is because OER is a very slow-moving reaction, which requires the transfer of four electrons – therefore having a large overpotential η [54].

Among the studied catalysts are rutile-type RuO_2 and IrO_2, which display high activity yet are oxidized and dissolved at high anodic potentials [54].

Ni and its oxide have been known to possess electrocatalytic activity towards OER [57]. Since Ni is found in combination with Fe on earth and Ni oxides and hydroxides may present iron impurities, a lot of research has focused on NiFe electrocatalysts for OER. The presence of iron in NiO_x has been found to enhance dramatically OER electrocatalysis [58], [59]. McCrory et al. [60] found that $NiFeO_x$ has a remarkable specific activity, larger than many other oxides. A study on NiHCF as electrocatalyst for OER has recently also been published [43]. Therefore, NiFe compounds deserve plenty of attention in the future developments.

Chapter 2
Aim of the thesis

This work has been developed around two main interconnected topics: the first involving the synthesis, characterization and an application of NiHCF and the second aimed to a structural characterization of a set of PBAs.

Concerning NiHCF, the work set out to develop a reproducible method to synthesize thin films of nickel hexacyanoferrate on Ni foam as a substrate, since a previous approach was not satisfying [61]. Both syntheses were based on an electrochemical route and Ni-foam was chosen as an electrode because of its large electroactive surface area and low cost. Characterization of the deposited material included cyclic voltammetry in different electrolytes to probe its electrochemical behavior and XPS spectroscopy to find out its stoichiometry. Finally, the performance of such material on Ni foam as electrocatalyst for oxygen evolution reaction (OER) was evaluated.

Besides this, XPS spectra of a set of ten powders - including both metal hexacyanoferrates and metal nitroprussides – were recorded to gain valuable information about the oxidation states of the metals and their stoichiometry. The spectra could also be helpful in detecting trends and in making comparisons, in order to get a wider picture of metal hexacyanoferrates as a class of compounds.

Chapter 3
Experimental

3.1 Reagents and materials

3.1.1 Reagents

$K_4Fe(CN)_6 \times 3H_2O$ (*CAS Number 14459-95-1*) was purchased from Merck, while $K_3Fe(CN)_6$ (*13746-66-2*), $Na_2Fe[(CN)_5NO] \times H_2O$ (*13755-38-9*), $Ni(NO_3)_2 \times 6H_2O$ (*13478-00-7*), $NaNO_3$ (*7631-99-4*), KNO_3 (*7757-79-1*) and KOH (*1310-58-3*) were purchased from Sigma-Aldrich. All compounds were used directly without further treatment or purification.

3.1.2 Powders

The following set of powders was provided (Table 1). They were all synthesized by co-precipitation methods in our group, yet by different researchers, by a protocol described in Mullaliu et. al [46]. Reported stoichiometries have been obtained by Atomic Emission Spectroscopy (AES – this acronym should not be confused with Auger Electron Spectroscopy).

Table 1 – Powder samples information: precursors and AES-evaluated stoichiometry

Sample name	Precursors	Stoichiometry
MnFeA02	$MnSO_4 \times H_2O$, $Na_4[Fe(CN)_6] \times 10H_2O$, Na_2SO_4	$Na_{1.3}Mn_{1.3}Fe(CN)_6$
MnFeA03	Same as MnFeA02	$Na_{1.9}Mn_{1.1}Fe(CN)_6$
TiFe01	$Ti(OBu)_4$, EtOH, $Na_4Fe(CN)_6$, HCl	$Na_{0.9}Ti_{0.7}Fe(CN)_6$
TiFe02	Same as TiFe01	Not determined
CuFeA	$CuSO_4$, $Na_4Fe(CN)_6$	$Na_{1.4}Cu_{1.7}Fe(CN)_6$
CuFeB	Same as CuFeA	$Na_{1.1}Cu_{1.6}Fe(CN)_6$
CuFeC	$CuSO_4$, $K_3Fe(CN)_6$	$K_{0.15}Cu_{1.5}Fe(CN)_6$

InFe02	$InCl_3$, $Na_4Fe(CN)_6$	Not determined
CoNP_05	$Co(NO_3)_2$, $Na_2[Fe(CN)_5NO]\times 2H_2O$, $NaNO_3$	$CoFe[(CN)_5NO]$
NiNP1	$NiSO_4$, $Na_2[Fe(CN)_5NO]\times 2H_2O$, $NaNO_3$	$NiFe[(CN)_5NO]$

3. 2 Electrochemistry

All electrochemical experiments were performed at room temperature using a CHI 620 potentiostat. A three-electrode cell configuration was always adopted, with a 5 mm × 5 mm Ni-foam substrate as working electrode, a standard calomel electrode (SCE) as reference and a Pt wire as auxiliary electrode. All mentioned solutions are aqueous solutions.

3.2.1 Electrosynthesis

3.2.1.1 Former electosynthesis

A former method, from a previous thesis [61], was first repeated. 50 mL solutions with 5 mM $K_3Fe(CN)_6$ and 0.1 M KNO_3 were prepared fresh each time. The open circuit potential between Ni foam and the solution was monitored for 300 seconds (equilibration time) and then, a potential of 1.0 V was applied for other 300 seconds. As a final step, a potential of 0.25 V was applied for 120 seconds.

3.2.1.2 New electrosynthesis

Three preliminary deposition protocols were pointed out in literature, differing in scan rates and explored areas, and they were tested to select the most suitable one. Method I was also arbitrarily tested:

I. [0.0 V- 1.2 V] at 100 mV/s scan rate
II. [0.0 V - 0.85 V] at 100 mV/s scan rate [38]
III. [0.0 V - 1.2 V] at 25 mV/s scan rate [36]
IV. [0.0 V - 0.85 V] at 25 mV/s scan rate [40]

Method III was later chosen and adopted for all later trials, as explained in Section 4.1.2. 50 mL aqueous solutions with 5mM $K_3Fe(CN)_6$, 5mM $Ni(NO_3)_2$ and 0.1 M KNO_3 were

prepared fresh each time. Cyclic voltammetry (CV) was performed, scanning from 0 V to 1.2 V potential at 25 mV/s for 15 full cycles. Since a precipitate was already formed in the flask, a magnetic stirrer was required to keep homogeneity in the medium during deposition.

3.2.2 Electrochemical characterization

3.2.2.1 Former electrosynthesis

The synthesized material was characterized by means of CV in 1 M $NaNO_3$ solution. 30 scans (15 full cycles) were recorded with a 50 mV/s scan rate, exploring the potential region -0.1 V - 0.8 V and starting from 0.25 V with a negative swipe.

3.2.2.2 New electrosynthesis

Materials deposited according preliminary trials I to IV were characterized with CV recorded in 1 M $NaNO_3$ solution. Again, 15 full cycles were recorded with a 50 mV/s scan rate, from -0.1 V to 0.8 V and starting from 0.25 V with a negative swipe.

Materials synthesized according to method III were characterized by CV in 0.1 M KNO3, 0.1 M NaNO3 and 1M KOH (after LSV). CV performed in 0.1 M KNO_3 were recorded with several scan rates, while in 0.1 M $NaNO_3$ and 1 M KOH only 50 mV/s and 10 mV/s scan rates, respectively, were used. The potential investigated area was still -0.1 V- 0.8 V in KNO_3 and $NaNO_3$, while it was 0.1 V – 0.45 V in KOH.

3.2.3 Oxygen Evolution Reaction

Linear Swipe Voltammetry was performed immediately after deposition, scanning at 10 mV/s from 0.0 V to 0.65 V in a 1 M KOH solution.

3.3 XPS measurements

3.3.1 Sample preparation

Compounds chosen as references – $K_4Fe(CN)_6$, $K_3Fe(CN)_6$ and $Na_2Fe[(CN)_5NO]$ – were milled in a mortar to reduce grain size and enhance homogeneity. Powders had been already milled and were used without further treatment. Electrochemical samples were exposed to air for at least two hours. Each sample was prepared on carbon tape placed on a square sample holder. Carbon tape area

was covered entirely and as homogenously as possible. The sample holder was always cleaned with acetone prior and after the use.

3.3.2 Measurements

XPS measurements were performed with a VG Escalab 220i-XL spectrometer. The employed spectrometer was equipped with a model 220 analyzer and a set of six channel electron multipliers with a 16 ns multidetector dead time. The working pressure was between 10^{-8} and10^{-9} mbar. A survey spectrum was recorded first every time to get qualitative information, then detailed spectra. The spectra parameters are summarized in Table 2, while Table 3 details the type of radiation (non-monochromatic) used for every sample.

Table 2 – Acquisition parameters of XPS measurements

Parameter	**Survey spectrum**	**Detailed spectra**
Binding energy range (eV)	-5 - 1200	Element depending
Pass energy (eV)	50	10 50(*)
Step width (eV)	0.5	0.1
Number of scans	1	4
Dwell time (ms)	100	300
Lens mode	Large Area (LAE)	Large Area (LAE)

(*) Electrochemical samples

Table 3 – X-Ray radiation sources employed in measurements

Radiation	**Photon Energy (eV)**	**Analyzed samples**
Al-Kα	1486.6	MnFeA02, MnFeA03, TiFe01, TiFe02, CuFeA, CuFeB, CuFeC, InFe02
Mg-Kα	1253.6	Used only in combination with Al-Kα
Both		Ni-foam untreated, Ni-foam cycled, NiHCF pristine, NiHCF reduced,

		NiHCF oxidised, CoNP_05, NiNP1

Reference compounds and powders were inserted in the machine and exposed to high vacuum for at least a night. No flood gun was used during measurement, yet $Na_2Fe[(CN)_5NO]$ spectrum was recorded a second time with flood gun operating to judge whether differential charging phenomena were occurring or not. No sputtering was ever performed.

3.3.3 Spectrum fitting

Spectra were fitted using Unifit 2020 software (https://www.unifit-software.de). Excitation satellites from non-monochromatic radiation were always subtracted from detailed spectra. A combination of polynomial and Shirley background was chosen. Peak shapes were simulated combining Lorentzian and Gaussian functions by convolution (Voigt profile).

When E_B values references are not being specified, it is implied that the values were presented by a databank in Unifit.

3.3.4 Charge correction

Although a common strategy is to charge-correct results on C 1s adventitious (aliphatic) carbon, either at 284.8 eV or 285.0 eV, N 1s seemed to be a better choice for the kind of species investigated in this work.

First, E_B values for N 1s cyanide signals were better documented in literature and had very close binding energy values, making N 1s a more reliable signal to perform charge correction upon. Also, C 1s cyanide signal is very close to aliphatic carbon's and the two species cannot be separately deconvoluted in fitting procedure – this feature will be clearly demonstrated in the results section (Chapter 4).

However, electrochemically modified samples are an exception to this choice, in fact they were charge-corrected on C 1s adventitious carbon. The reason lies in the little amount of material deposited on the substrate, which would make charge correction on N 1s less reliable. And yet, because of that, C 1s signal could be attributed mainly to adventitious carbon.

Table 4 summarizes the signals and the binding energies values on which charge correction was performed according to the analyzed sample.

Table 4 – Chosen signals and relative E_B for charge correction

Sample	Signal and species	E_B (eV)	Reference
$K_4Fe(CN)_6$ and MHCFs	N 1s *-CN*	397.6	[62]
$K_3Fe(CN)_6$	N 1s *-CN*	398.1	[63]
$Na_2Fe[(CN)_5NO]$ and MNPs	N 1s *-CN*	397.2	[62]
Electrochemical samples	C 1s *adventitious carbon* *-CH_2-*	285.0	[64]

Chapter 4
Results and Discussion

4.1 Electrochemistry

4.1.1 Former synthesis

Several samples were synthesized and tested, as shown in Figure 5. When $NaNO_3$ is employed as electrolyte, a single reversible redox couple is observed, with an anodic E_p at 0.34 V and a cathodic E_p at 0.32 V. It is evident that the synthesis is not reproducible, suggesting the idea of different amounts of deposit. These features are in agreement with previous findings and the porous nature of Ni-foam was given as an explanation for the lack of reproducibility [61].

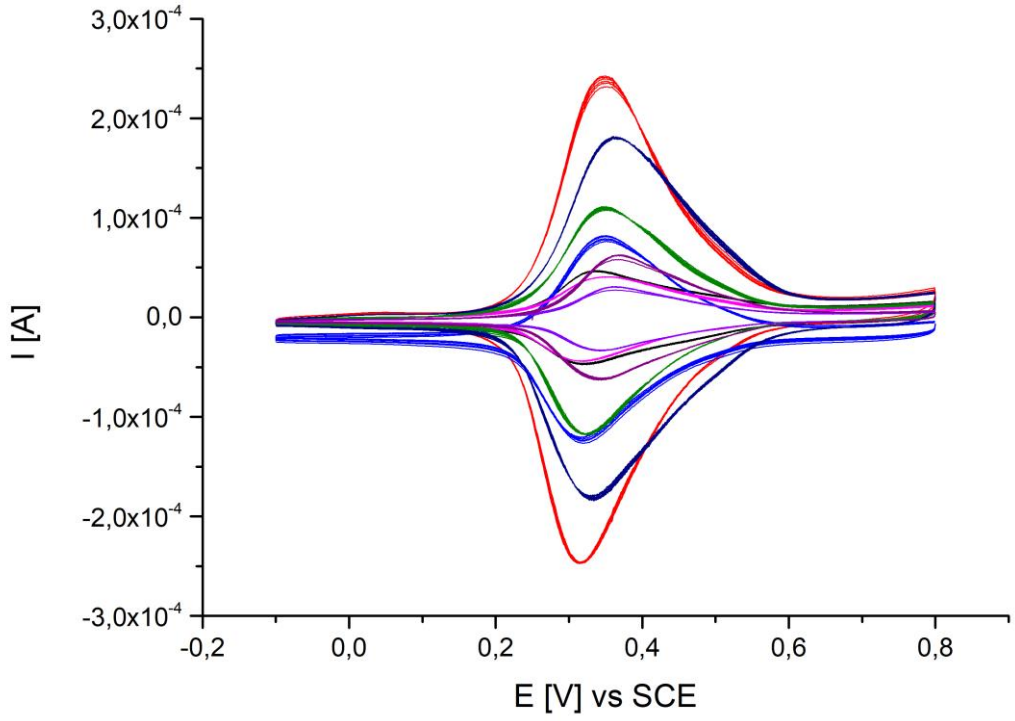

Figure 5 – Cyclic voltammograms of thin films of NiHCF electrodeposited on Ni-foam in 1M $NaNO_3$ in -0.1 V to 0.8 V range at 50 mV/s scan rate

4.1.2 New synthesis

Since the largest amount of NiHCF was synthesized with this protocol (Figure 6), Method III - 25 mV/s scan rate exploring the 0.0 V – 1.2 V are – was selected as new method.

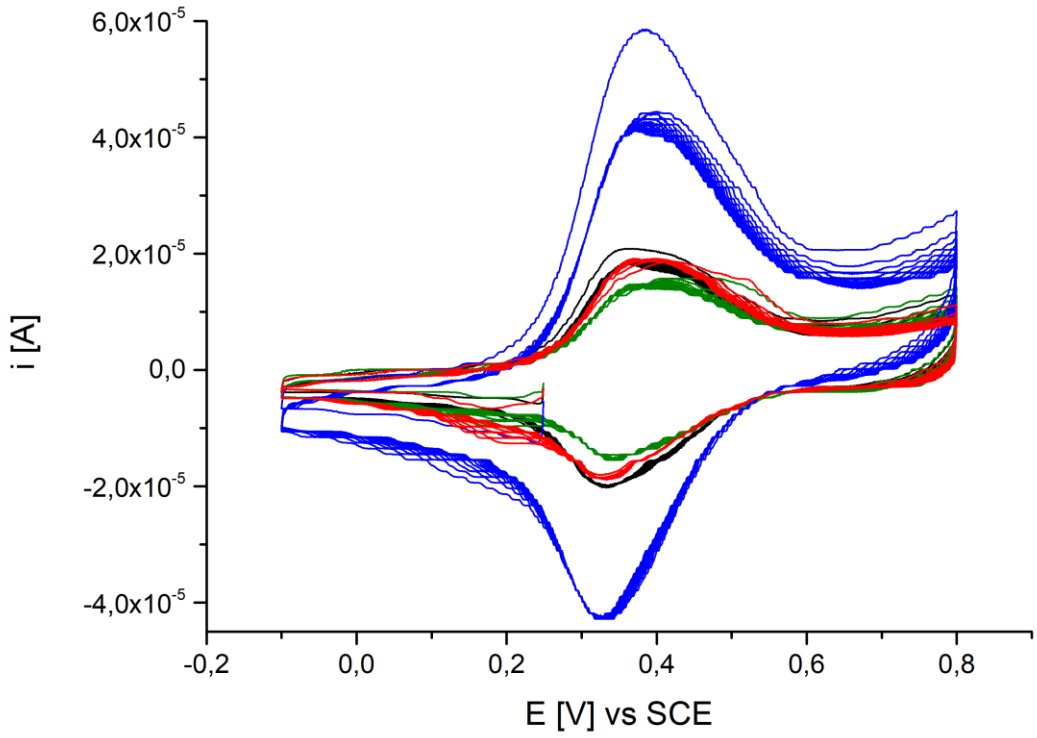

Figure 6 – Cyclic voltammograms of thin films of NiHCF electrodeposited on Ni-foam in 1M $NaNO_3$ in -0.1 V to 0.8 V range at 50 mV/s scan rate. Films were synthesized according to procedures: I) 0.0V-1.2V at 100mV/s (black), II) 0.0V-0.85V at 100 mV/s (green), III) 0.0V-1.2V at 25 mV/s (blue), IV)0.0V-0.85V at 25 mV/s (red)

The resulting deposition voltammogram is displayed in Figure 7. The arrows point towards the direction of change of intensity during the run. First, a high cathodic current is noticed in the 0.0 V – 0.2 V area: this feature is associated to a reduction process happening at the electrode. The cathodic current peak initially has the shape of a totally irreversible peak. Its intensity continually decreases during cycling and the peak position shifts to a slightly higher potential (0.12 V), while an anodic peak at 0.21 V appears and increases. The overall final shape of such region resembles a reversible redox couple. It is plausible that these signals can be attributed to aqueous $[Fe(CN)_6]^{3-}$, which is taken away from the solution as the deposition goes on. When the electrode area is covered with the material, ferricyanide ion is not needed anymore and the redox couple signal is therefore detected. The concurrent progress of the

deposition reaction is proved by rise in intensity of the signals in the 0.3 V - 0.6 V voltammogram region, where the presence of two redox couples could be evinced. Zamponi et. al [27] obtained a similar voltammogram, identifying ferricyianide ion reduction at potentials lower than 0.3 V and two redox couples between 0.35 V and 0.6 V – which were attributed to the synthesized films of NiHCF.

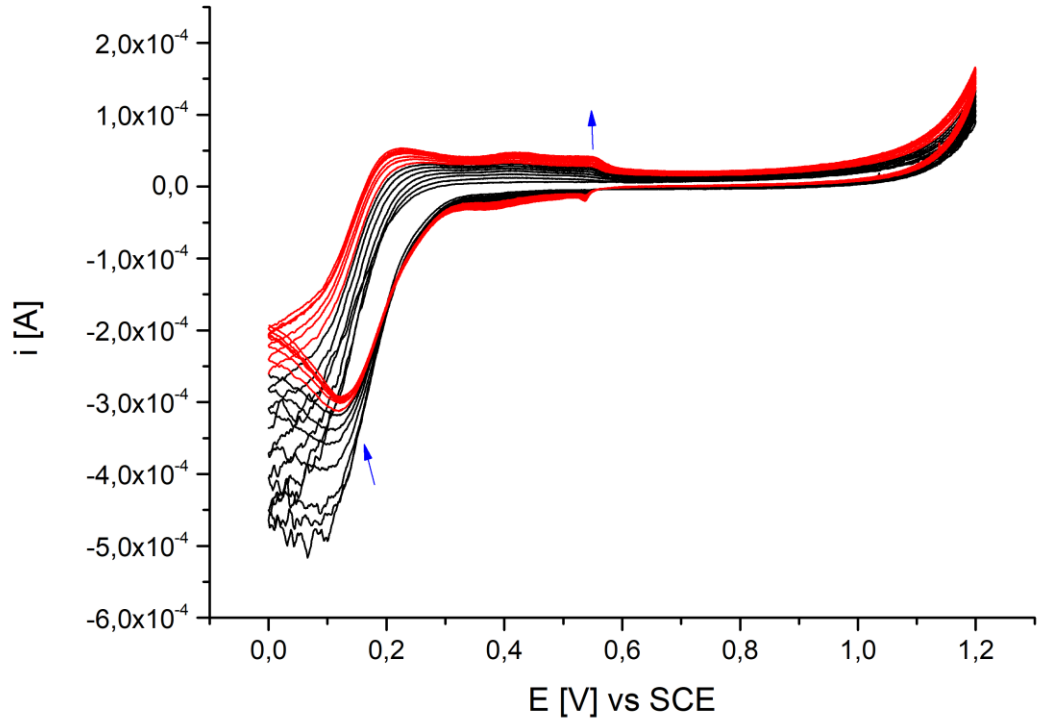

Figure 7 – Cyclic voltammogram of NiHCF being synthesized on Ni-foam via cycling from 0.0 V to 1.2 V at a 25 mV/s scan rate from a 5mM $Ni(NO_3)_2$, 5 mM $K_3Fe(CN)_6$ and 0.1 M KNO_3 solution

4.1.3 Characterization

Figure 8 provides proof that films of NiHCF were actually deposited on Ni-foam with the new method. The voltammetric response of the synthesized material can be seen: two redox couples appear. The first couple is found at approximately 0.37 V (cathodic) and 0.45 V (anodic), while the second one at 0.53 V (cathodic) and 0.55 V (anodic). The shape and the presence of two redox couples in the voltammogram match results provided by literature [27][65][66]. The corresponding electrochemical reactions are [41] :

1) $Ni_{1.5}[Fe^{III}(CN)_6] + K^+ + e^- \leftrightarrow KNi_{1.5}[Fe^{II}(CN)_6]$

2) $KNi[Fe^{III}(CN)_6] + K^+ + e^- \leftrightarrow K_2Ni[Fe^{II}(CN)_6]$

Reaction 1 occurs at higher potentials, while Reaction 2 at lower potentials. The existence of two forms of NiHCF, one Ni-rich and the other K^+-rich, was postulated to explain the results [41].

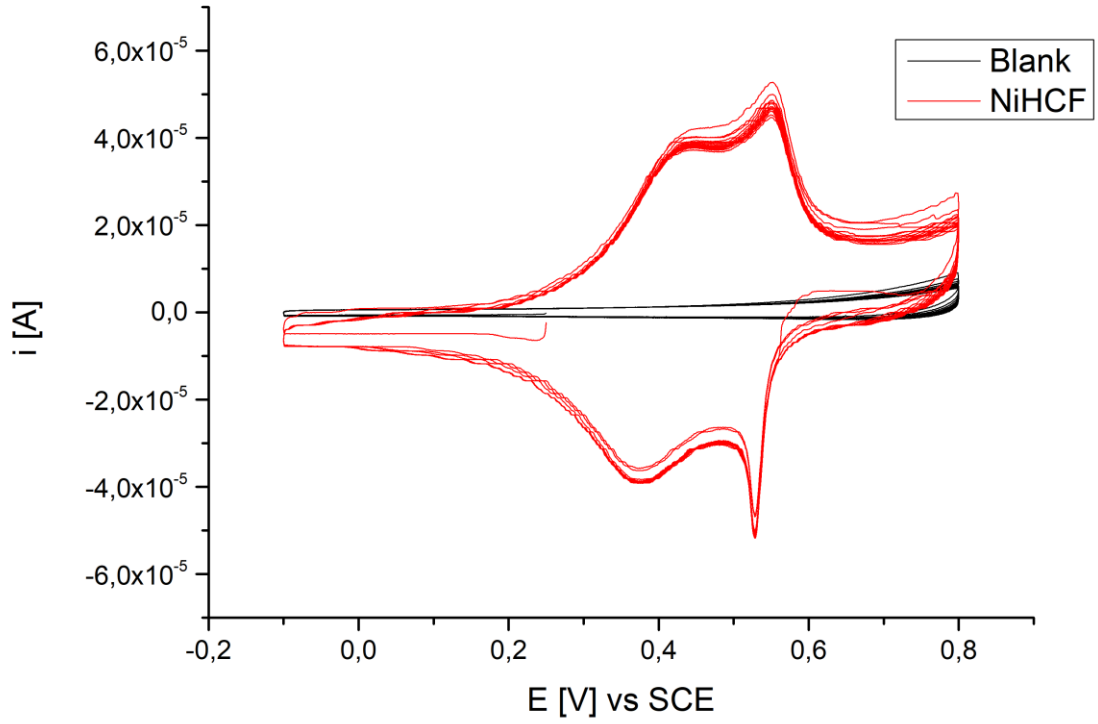

Figure 8 – Cyclic voltammograms of thin films on NiHCF on Ni-foam and Ni-foam (blank) in 0.1 M KNO_3 in -0.1 V to 0.8 V at 50 mV/s scan rate

Figure 9 displays the reproducibility of the newly proposed synthetic protocol. It is demonstrated that the synthesis is not perfectly reproducible although progress has been clearly made, as voltammograms are mainly superimposable. In this case, it might be assumed that different amounts of deposited material can be related to differences in the porous substrate's area - both internal and external.

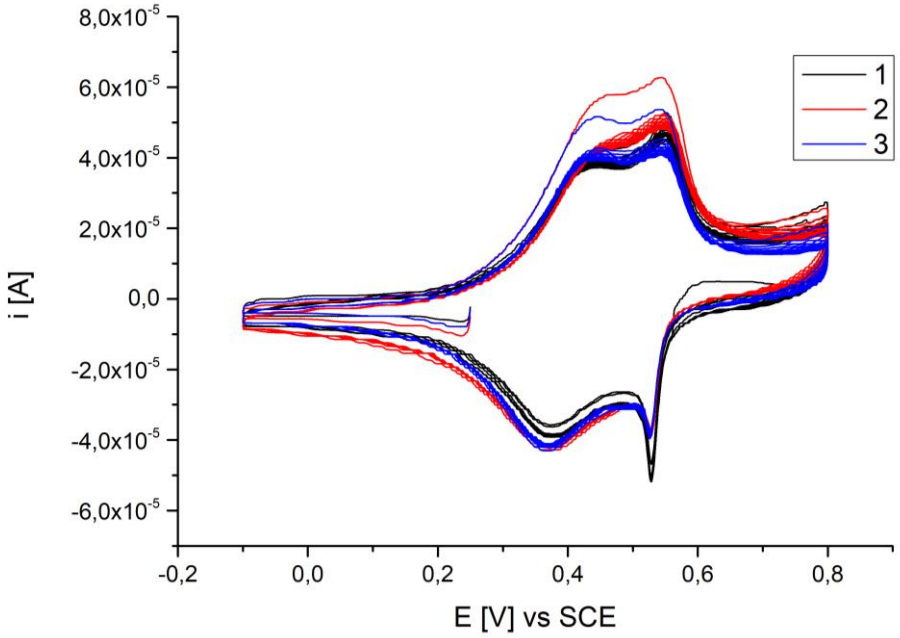

Figure 9 – Selected cyclic voltammograms of thin films of NiHCF on Ni-foam in 0.1 M KNO_3 in -0.1 V to 0.8 V range at 50 mV/s scan rate

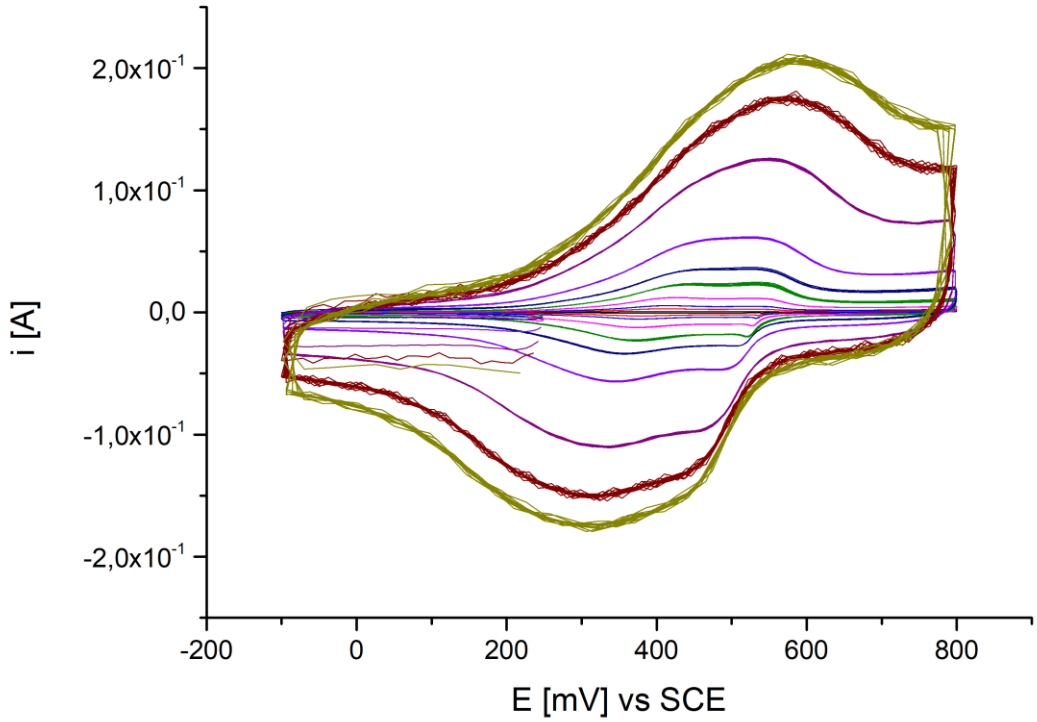

Figure 10 – Cyclic voltammograms of thin films of NiHCF on Ni-foam in 0.1 M KNO_3 in -0.1 V to 0.8 V range at scan rates: 1mV/s, 5 mV/s, 10 mV/s, 25 mV/s, 50 mV/s, 100 mV/s, 200 mV/s, 500 mV/s, 800 mV/s, 1V/s (each recorded with suitable sensitivity)

The characteristic voltammograms were then recorded at several different scan rates, as shown in Figure 10. The two-redox couples profile disappears at high scan rates (higher than 100 mV/s).

The dependency between I_p values and scan rates was explored in Graph 1. Direct proportionality between I_p and v is observed up to 50 mV/s scan rate: films of NiHCF behave indeed like a monolayer (monolayer regime). However, for scan rates above 100 mV/s, direct proportionality between I_p and $v^{1/2}$ is observed: NiHCF films behave like a bulk deposit, in the so-called "diffusive regime". 100 mV/s scan rate was a value at which change happened: it fit better in the diffusive regime than in the monolayer regime.

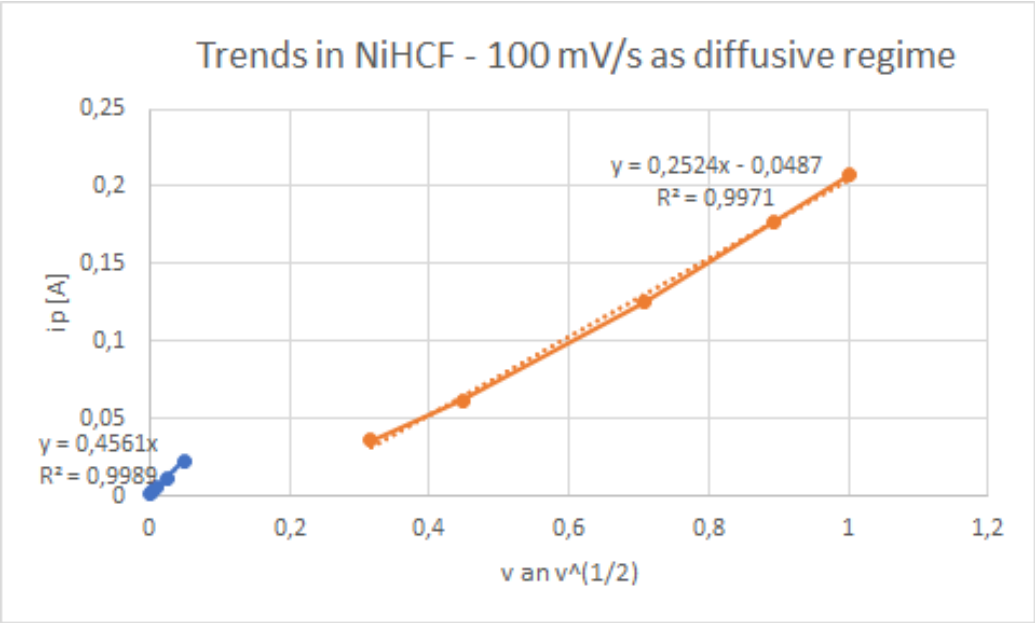

Graph 1 – Linearity between I_p values and scan rates: I_p α v (blue line – monolayer regime), I_p α $v^{1/2}$ (orange line – diffusive regime)

4.1.4 Oxygen Evolution Reaction

A blank of Ni-foam in 1 M KOH was first recorded and is shown in Figure 11. The cathodic I_p at 0.21 V rises slightly yet constantly in intensity, which indicates a reduction reaction taking place more over time. Since Ni-foam should supposedly be Ni^0, it is difficult to state with certainty which process is involved.

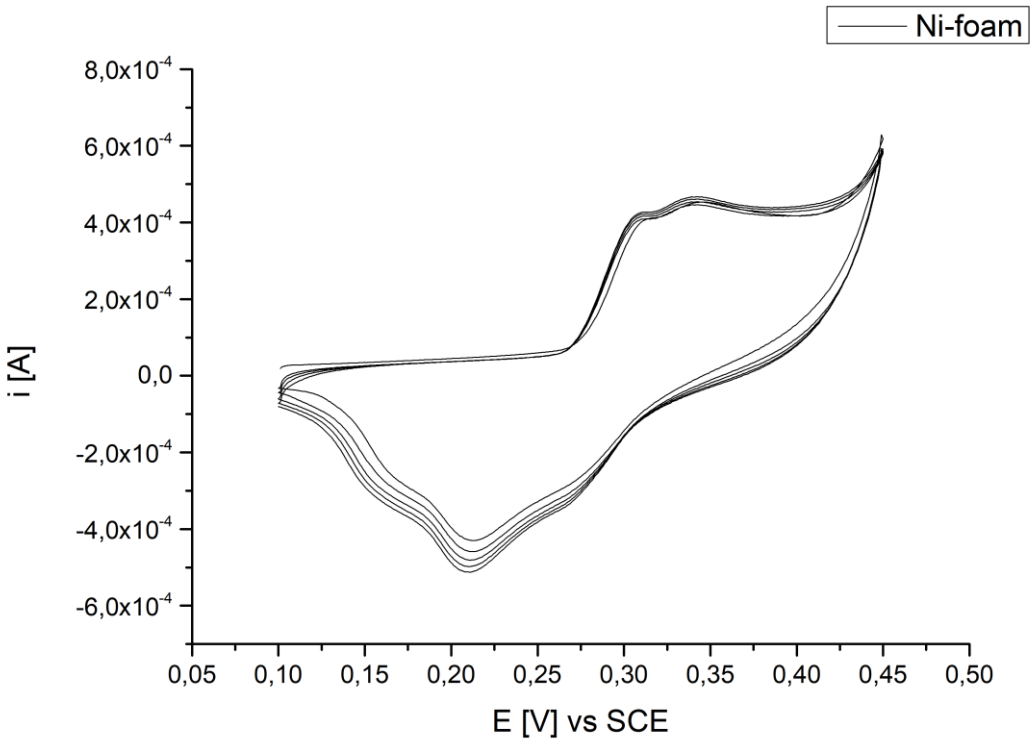

Figure 11 – Cyclic voltammogram of Ni-foam in 1 M KOH in 0.1 V to 0.45 V range at 10 mV/s scan rate

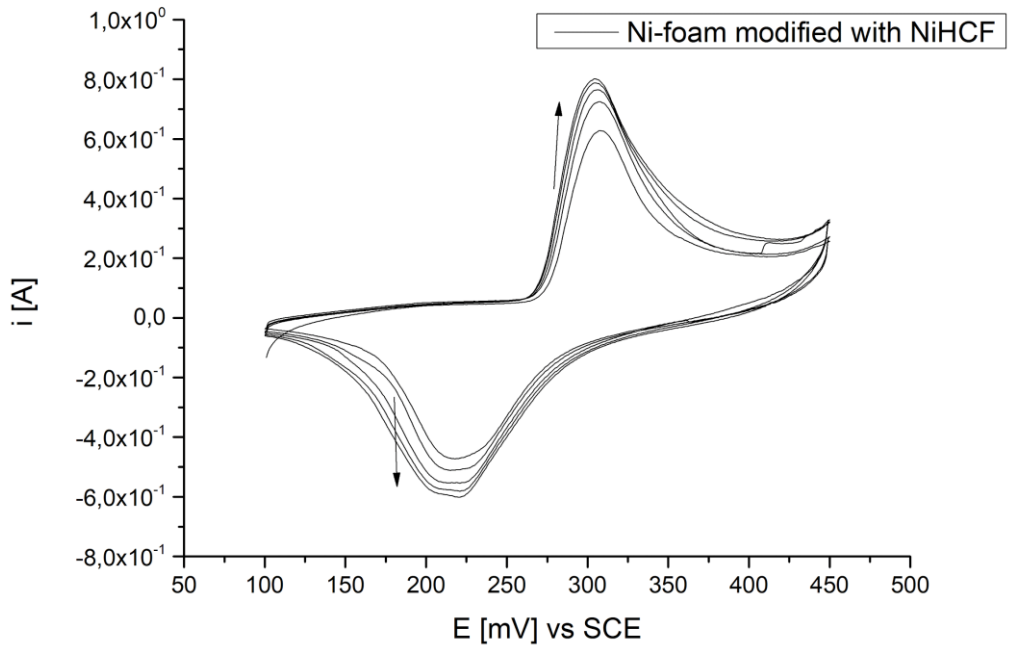

Figure 12 - Cyclic voltammogram of thin films of NiHCF on Ni-foam in 1 M KOH in 0.1 V to 0.45 V at 10 mV/s scan rate

Figure 12 shows the voltammogram for NiHCF on Ni-foam. Although two redox couples - as NiHCF should have - were seen in a preliminary experiment, later voltammograms showed a single reversible redox couple. Its peak intensity increases during cycling. Again, it is difficult to state precisely what occurs, yet it is well established that the NiHCF undergoes profound modification in alkaline solutions [67].

Oxygen Evolution Reaction performances were finally evaluated. Five samples and Ni-foam (blank) were tested both before (Figure 13) and after (Figure 14) cycling in 1 M KOH.

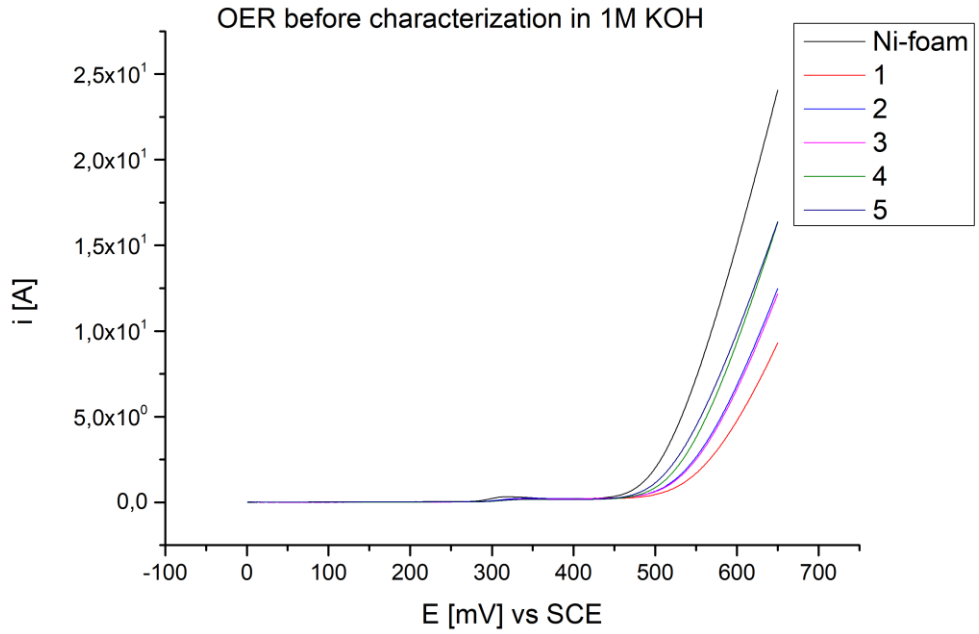

Figure 13– Linear Sweep Voltammogram of OER performance of films of NiHCF and Ni-foam in 1 M KOH in 0.0 V to 0.65 V range at 10 mV/s scan rate (before further characterization)

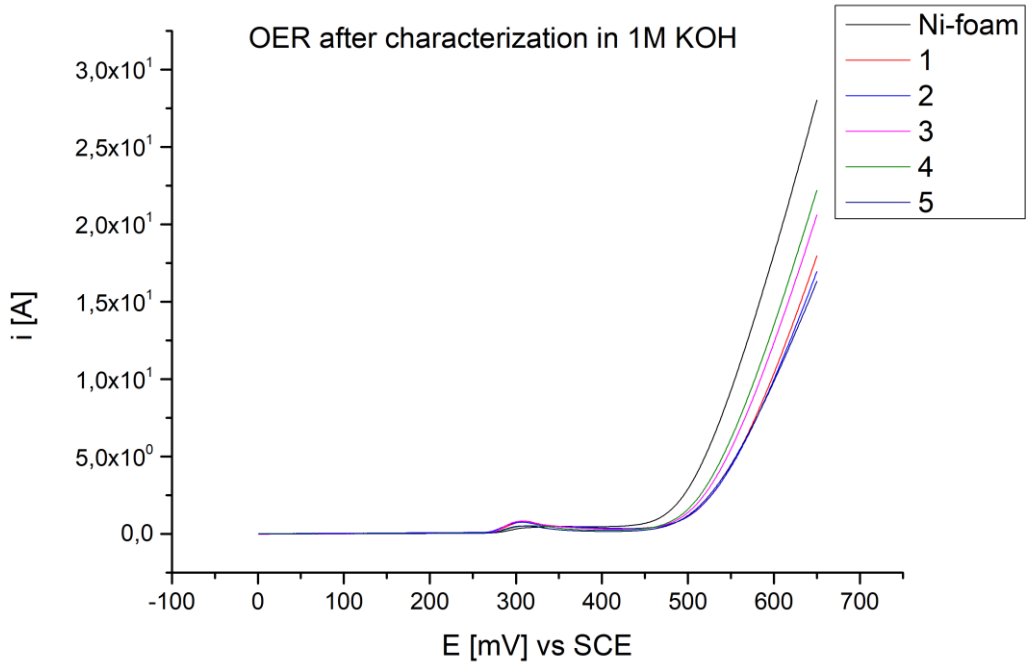

Figure 14 - Linear Sweep Voltammogram of OER performance of films of NiHCF and Ni-foam in 1 M KOH in 0.0 V to 0.65 V range at 10 mV/s scan rate (after characterization)

Ni-foam's electrocatalytic activity is greater than NiHCF's both before and after characterization in 1M KOH. Thus, it is unknown how much of NiHCF's electrocatalytic activity derives from the material itself or Ni-foam substrate. A deeper study on Ni-foam's composition (Section 4.2) could be helpful to better understand its remarkable activity in OER. Actually, the decrease in electrocatalytic performance after modification on Ni-foam with NiHCF may suggest that the material's deposition actually covers some of Ni-foam's highly active sites - therefore hindering electrocatalysis.

After characterization, the samples all displayed enhanced electrocatalytic performance (higher slope) - except for Ni-foam. The peak at 0.3 V is also more pronounced. This is further proof that, during cycling in KOH, chemical modifications that enhance electrocatalysis occur.

As OER performances are therefore related to Ni-foam and not to synthesized NiHCF, further tests were not carried out.

4.2 XPS study of Nickel Hexacyanoferrate

Five samples were measured by XPS:

- Ni-foam untreated
- Ni-foam cycled: the substrate being cycled with the same settings for the electrochemical synthesis, yet in 0.1 M KNO_3
- NiHCF pristine
- NiHCF reduced: NiHCF being synthesized and then reduced to -0.1 V in 0.1 M KNO_3
- NiHCF oxidized: NiHCF being synthesized and then oxidized to +0.8 V in 0.1 M KNO_3

Some points may start from discussing Ni-foam spectra. Survey spectrum showed carbon (adventitious carbon) as the only impurity present.

Figure 15 shows the Ni $2p_{3/2}$ signal for Ni-foam untreated. This might be considered representative, since all samples displayed a similar Ni $2p_{3/2}$ signal. Each Ni $2p_{3/2}$ was fitted with three singlets, each having a satellite. In case of Ni-foam untreated, XPS experiments suggested that exposure to air oxidized most of the substrate (Ni metal, 852.7 eV) to NiO (854.4 eV) and $Ni(OH)_2$ (855.9 eV) or Ni_2O_3 (856.0 eV) – these two species are difficult to differentiate given the close binding energies.

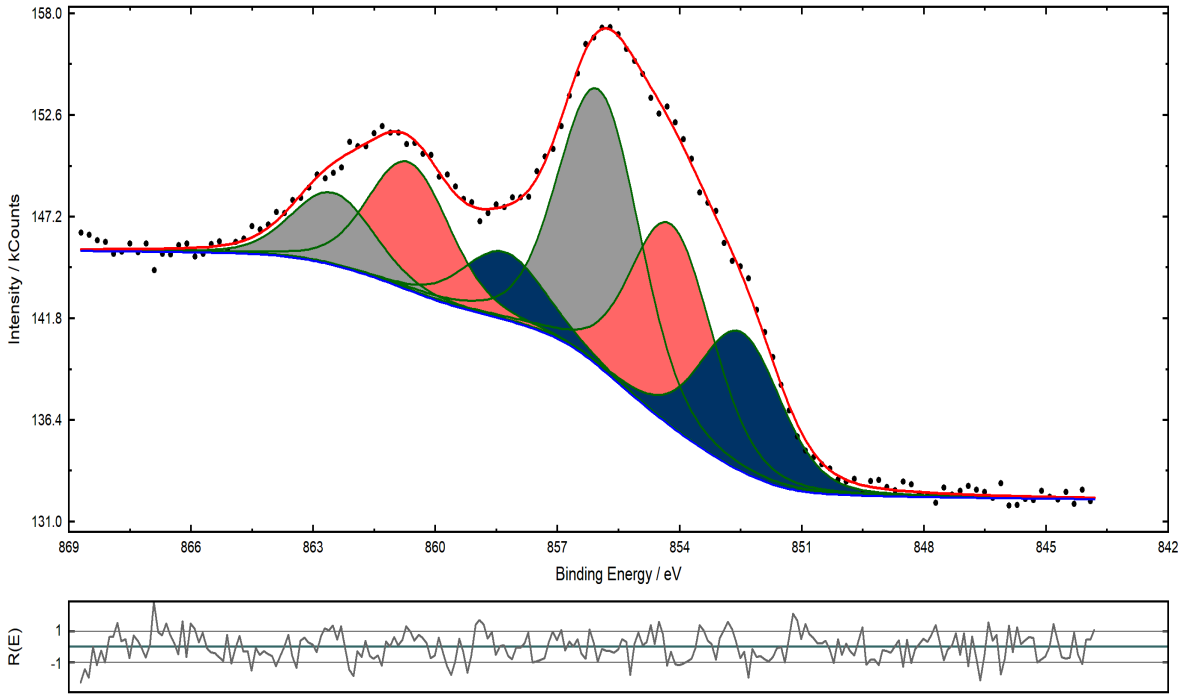

Figure 15 - Ni-foam untreated Ni $2p_{3/2}$ XPS detailed spectrum: Ni metal and satellite (blue), NiO and satellite (pink) and $Ni(OH)_2$ and satellite (grey)

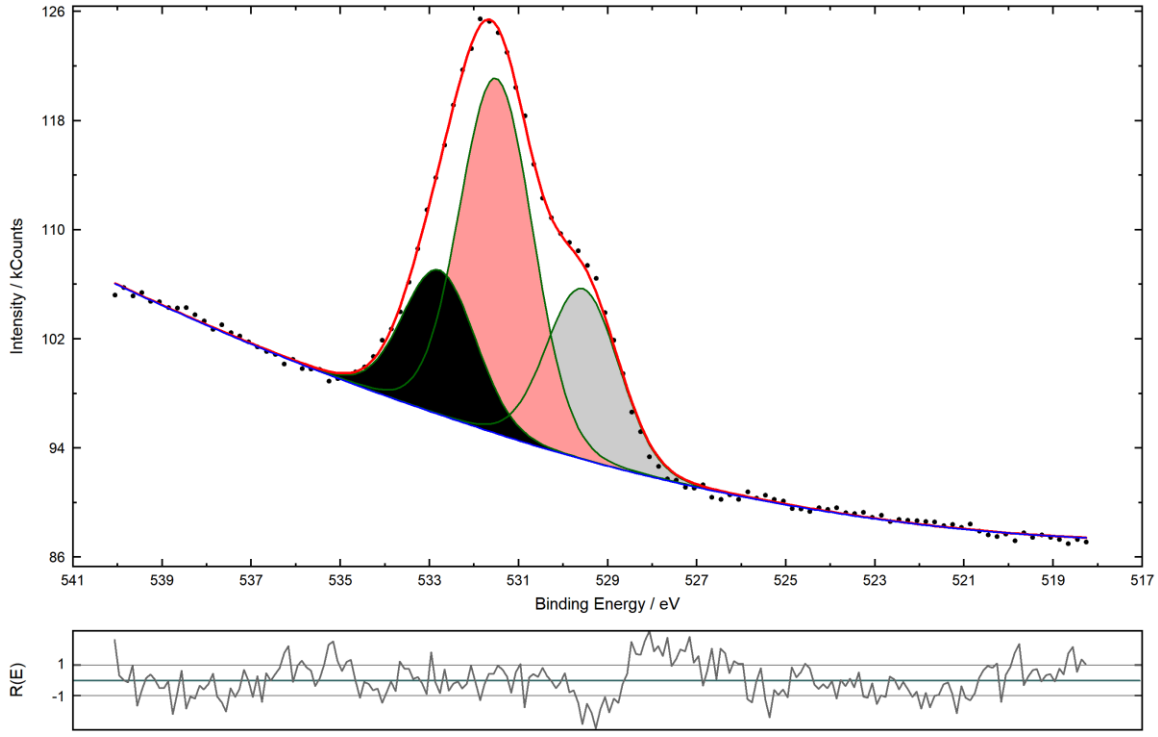

Figure 16 - Ni-foam untreated O 1s XPS detailed spectrum

The presence of NiO and $Ni(OH)_2$ is also validated in the O 1s spectrum (Figure 16), at 529.6 eV and 531.5 eV respectively. The peak at 532.8 eV is alcohol-type oxygen, coming very probably from dirt.

In Figure 17, a plot displaying Ni 2p spectra for all samples is provided.

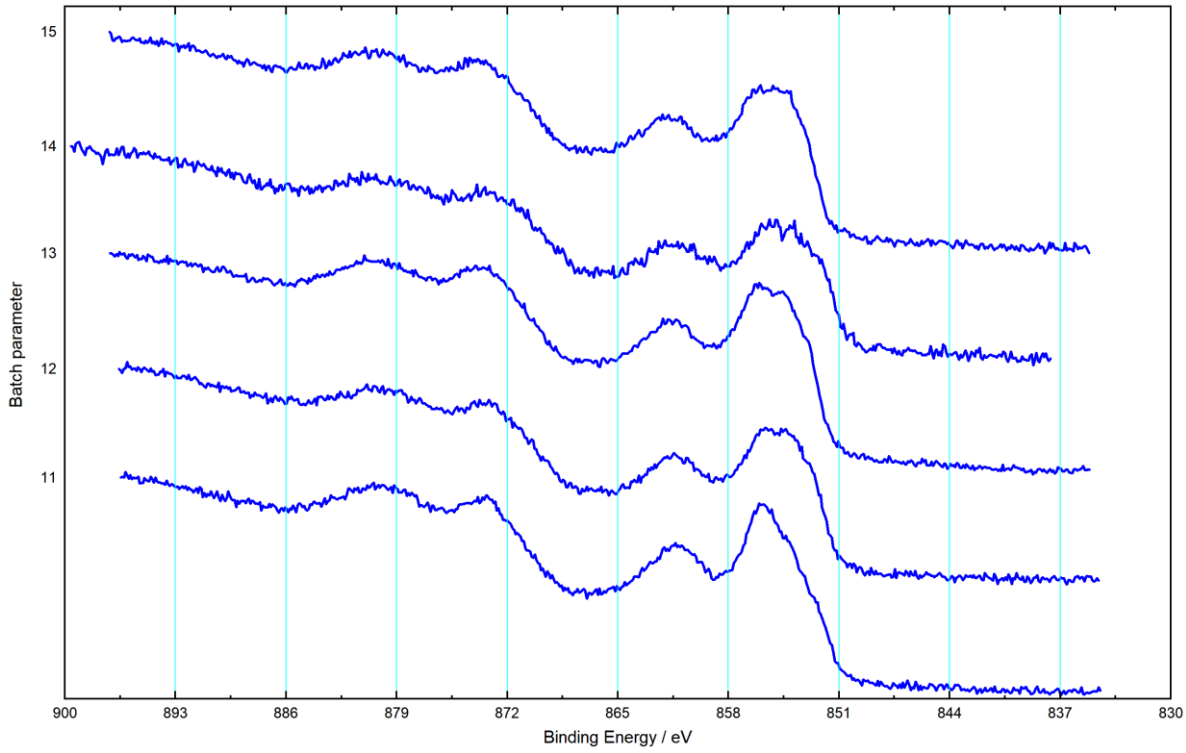

Figure 17 - Ni 2p signals (XPS); Batch Parameter (from bottom to top) 11: Ni-foam untreated, 12: Ni-foam cycled, 13: NiHCF pristine, 14: NiHCF reduced, 15: NiHCF oxidized

The evolution of the Ni 2p signal is not easy to interpret. Ni-foam untreated (11) is the only sample to present a sharp peak in the Ni $2p_{3/2}$ region: other samples do not have edgy peaks and they all seem to have two main species present in similar amounts. The lower binding energy side of the Ni $2p_{3/2}$ also rises more smoothly in the case of Ni-foam untreated. Cycling of Ni-foam, whether with NiHCF or not, seems to significantly alter the substrate nevertheless.

Table 5 shows E_B values and relative amounts of species in Ni $2p_{3/2}$ for all the samples resulting from a peak fit. Satellites were not included in the quantification. Order of the peaks (1,2,3) goes from higher to lower binding energies.

Table 5 - Ni $2p_{3/2}$ peaks: binding energies and relative amounts (excluding satellites)

Sample	**E_B Peak 1 (eV)** ***Relative amount (%)***	**E_B Peak 2 (eV)** ***Relative amount (%)***	**E_B Peak 3 (eV)** ***Relative amount (%)***	**$Ni2p_{3/2}/Fe2p_{3/2}$ ratio**
Ni-foam untreated	856.0 *31.3*	854.4 *22.8*	852.6 *15.7*	31.7
Ni-foam cycled	856.1 *23.6*	854.4 *24.6*	852.8 *24.1*	Indefinite, no Fe was detected
NiHCF pristine	856.1 *17.2*	854.45 *23.7*	852.9 *17.6*	9.9
NiHCF reduced	855.9 *22.8*	854.1 *25.2*	852.2 *24.7*	2.53
NiHCF oxidized	856.5 *23.3*	854.8 *25.8*	853.3 *23.1*	16.9

Peak 1 (attributed to Ni^{II} hydroxide in Ni-foam untreated) undergoes relevant changes in NiHCF oxidized. Its E_B changes significantly, while in the other samples it stays the same. Its relative amount, though, decreases in cycled samples. Peak 2 (attributed to NiO in Ni-foam untreated) changes its E_B in both NiHCF reduced and oxidized, yet its relative amount stays the same. Peak 3 (attributed to Ni-metal in Ni-foam untreated) changes the most: not only does the E_B change in every case – even though some changes are minor, being less than 1 eV apart -, also the relative amount does. Neverthless, NiO and $Ni(OH)_2$ seem to be present in notable quantities – this feature provides an excellent explanation for the OER results obtained. The Ni/Fe ratio shows that some Fe can be already present as an impurity in Ni-foam. Since CV characterization (Section 4.1.3) of NiHCF on Ni-foam revealed that the synthesis was reproducible to a high degree, it is possible that the synthesis is not homogeneous and the porous nature of the substrate enhances the possibility of random and less-structured response. Non-homogeneity of NiHCF synthesis on Ni foam was also proved by SEM in a previous thesis [68]. Also, as synthesized NiHCF is supposed to be few monolayers, photoelectrons from underlying Ni-foam can still be probed – therefore contributing to the high Ni 2p signal.

Fe $2p_{3/2}$ signals are also shown for every sample (Figure 18). The signal to noise ratio was very low in each measurement. It is difficult to state with certainty the oxidation state of Fe. The spectra prove only that the amount of Fe has increased remarkably due to the synthesis and the substrate was indeed modified.

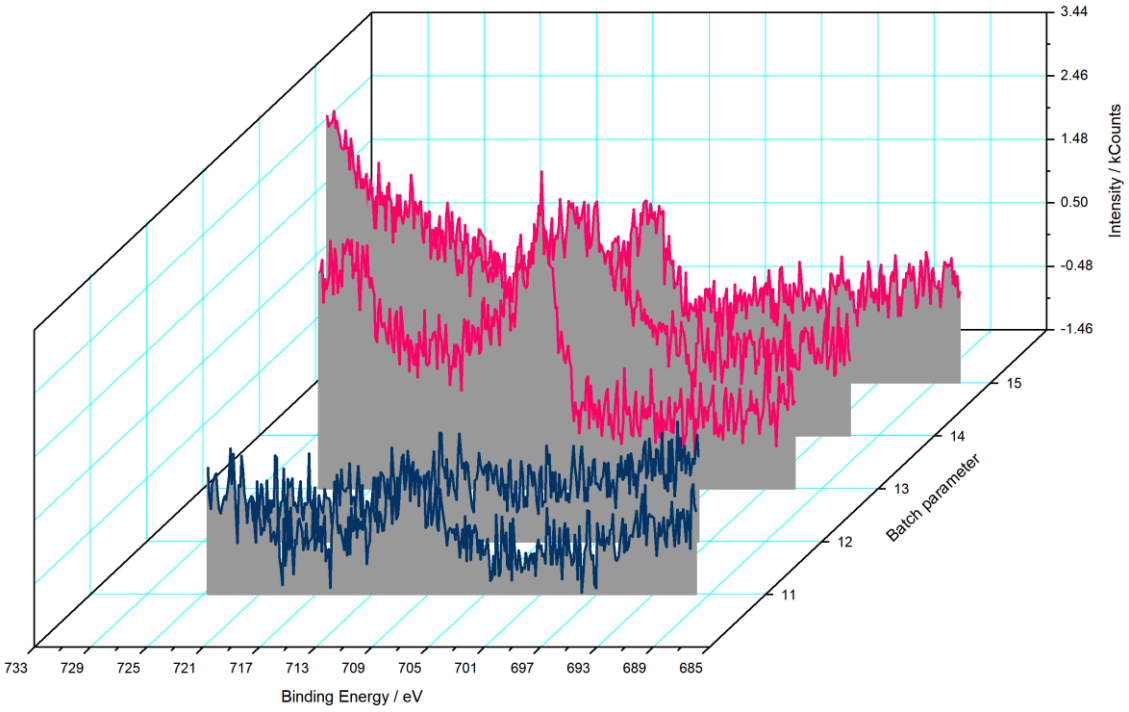

Figure 18 – Fe $2p_{3/2}$ signals (XPS); Batch Parameter 11: Ni-foam untreated, 12: Ni-foam cycled, 13: NiHCF pristine, 14: NiHCF reduced, 15: NiHCF oxidized

Since detected Fe was little, it is possible to assume that a corresponding Ni signal in Ni 2p for synthesized NiHCF is present, yet not big enough to be properly deconvoluted. It also might be possibly harder to differentiate due to a similar binding energy to one of the Ni species present in the sample.

Another proof comes from the survey spectrum for Ni-foam untreated (Figure 19), where no nitrogen was detected.

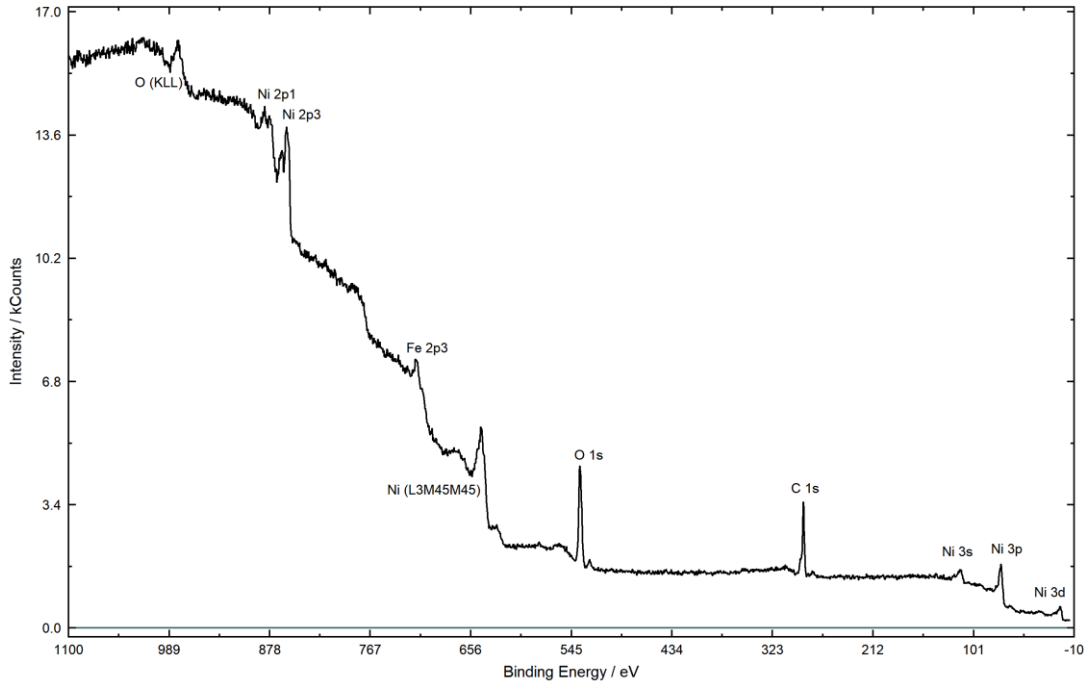

Figure 19 - Ni-foam untreated XPS survey spectrum

The N 1s signal for NiHCF pristine (Figure 20) is very low in intensity. No real information can be obtained, aside from proving that the substrate was modified.

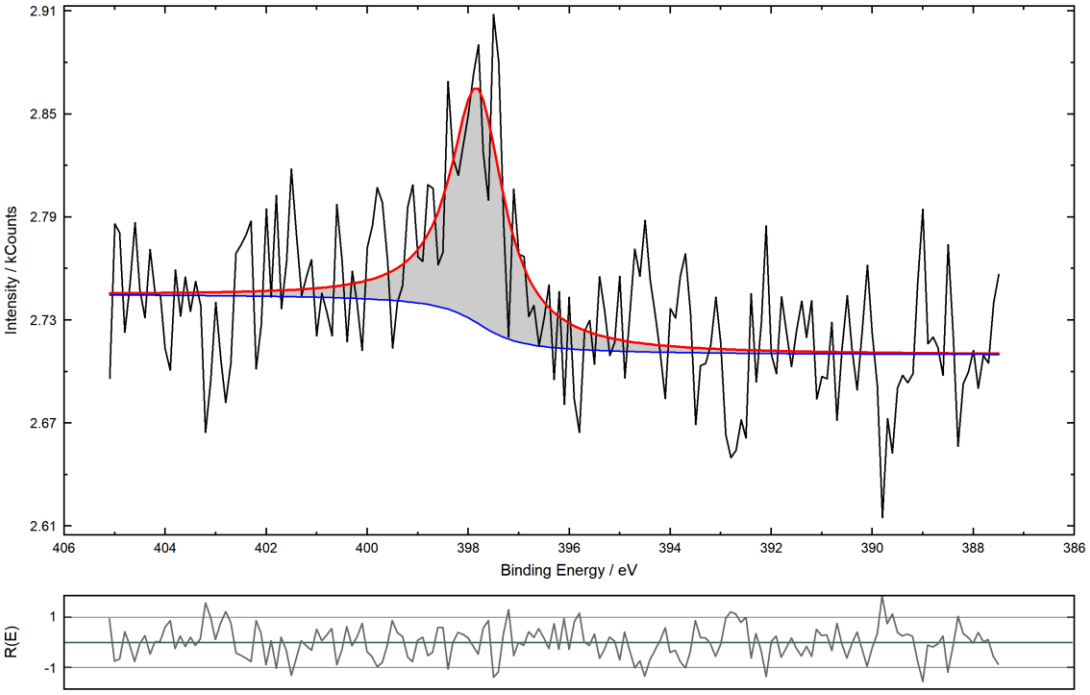

Figure 20 - NiHCF pristine N 1s XPS detailed spectrum

4.3 XPS study of powders

In this part, reference compounds spectra will first be shown and discussed to state some fundamental features about fitting and interpretation of the main signals – which are valuable also to the discussion regarding powders.

For each powder, spectra of metal M and Fe and a quantification table will be provided. C 1s, N 1s, Na 1s and O 1s spectra will not be shown, except when they present any discrepancies from the ones already shown in the section dedicated to reference compounds. Nevertheless, only main lines will be shown and discussed.

4.3.1 Reference compounds

4.3.1.1 $K_4Fe(CN)_6 \times 3H_2O$

Figure 21 shows the survey spectrum for $K_4Fe(CN)_6$ trihydrate. Every expected element is present and no impurities are detected.

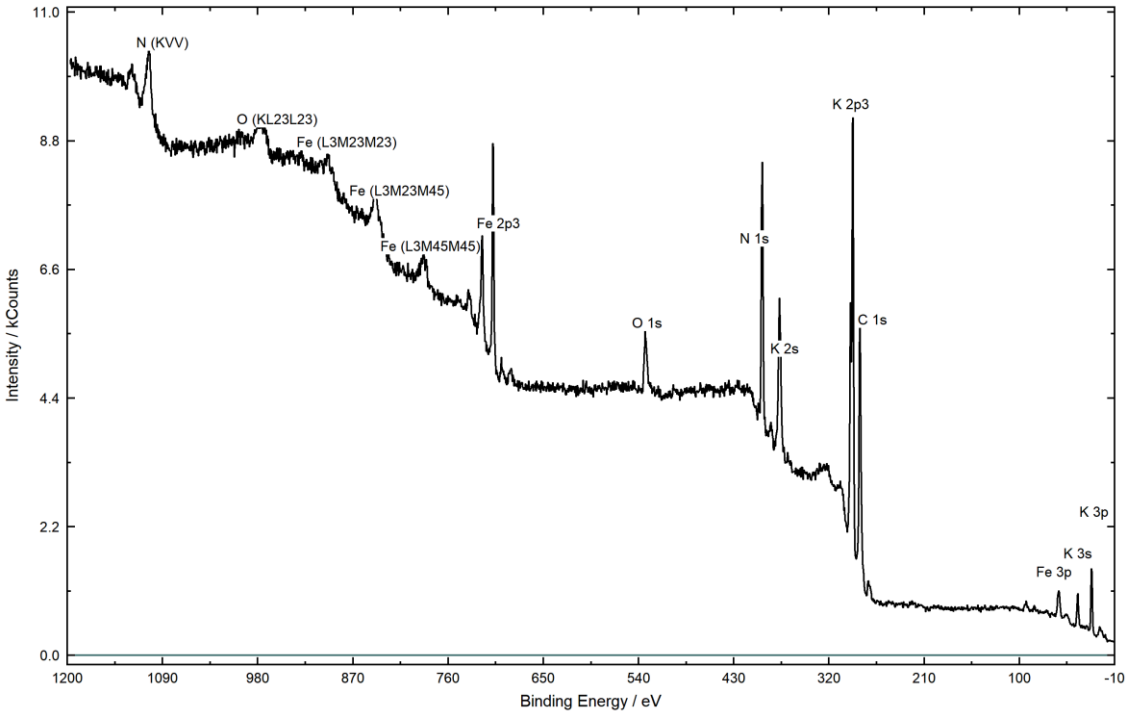

Figure 21 - $K_4Fe(CN)_6 \times 3H_2O$ XPS survey spectrum

Figure 22 displays N 1s spectrum, on which charge correction was performed. The N 1s signal is a singlet entirely dominated by -CN group. A recently reported value in literature for N 1s in this compound is 397.45 eV [69].

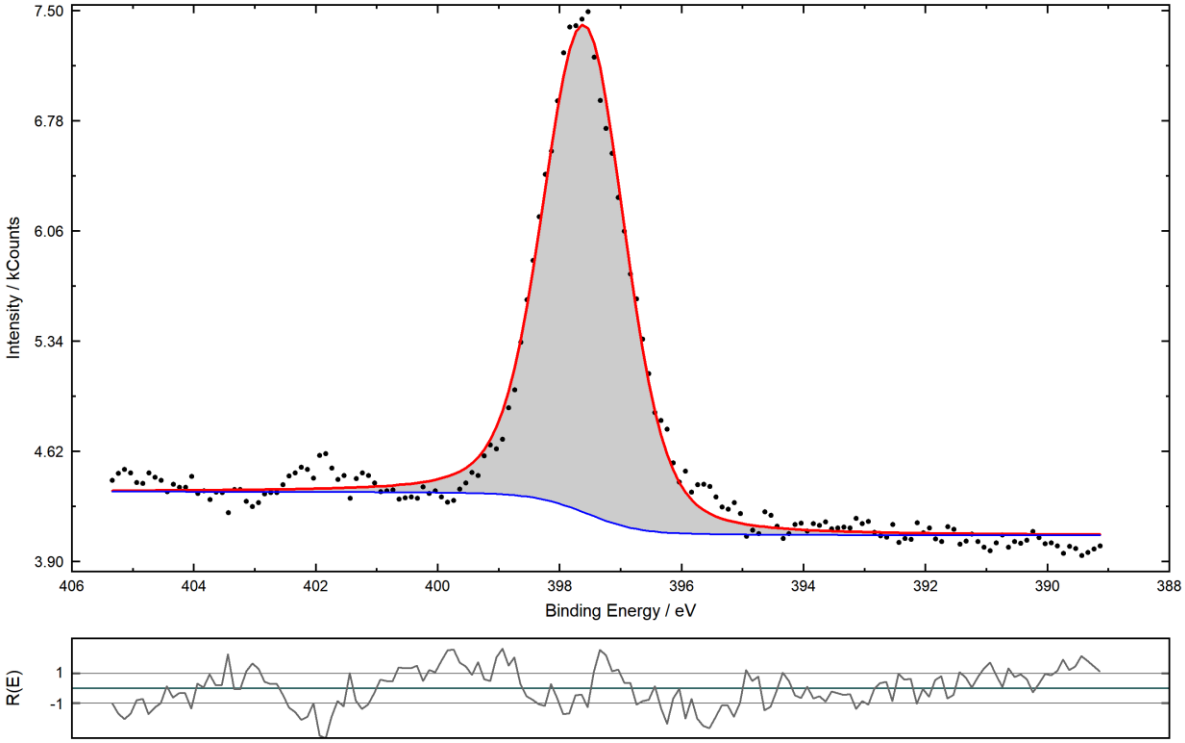

Figure 22 - $K_4Fe(CN)_6$ N 1s XPS detailed spectrum

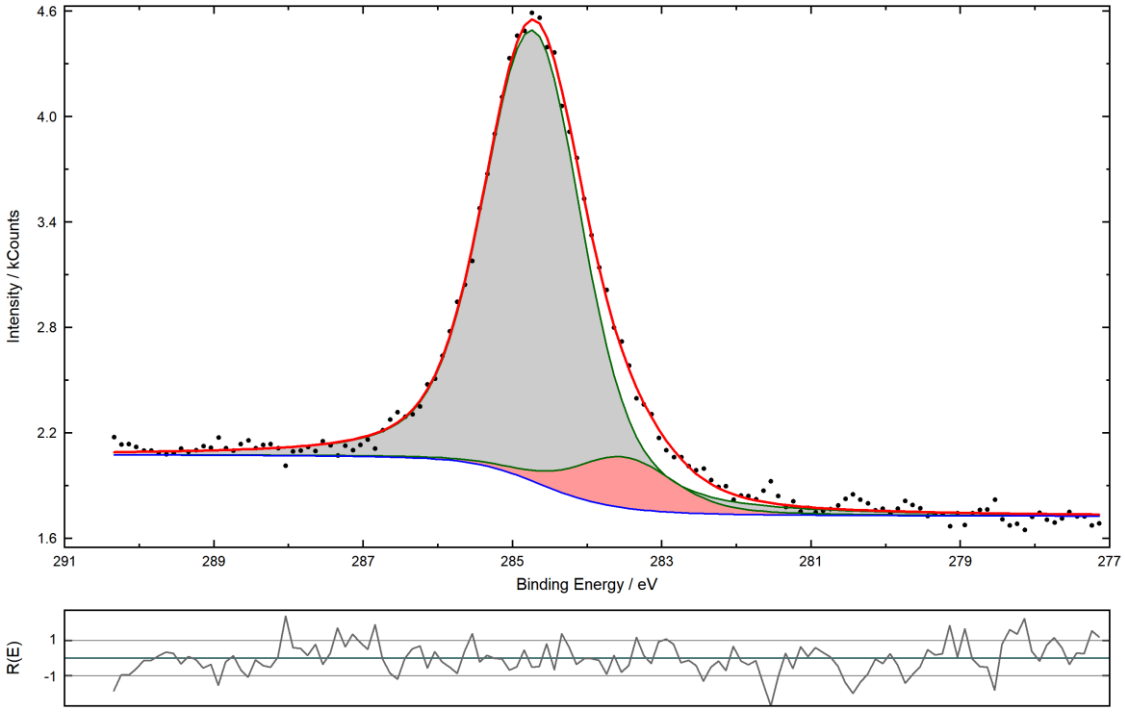

Figure 23 - $K_4Fe(CN)_6$ C 1s XPS detailed spectrum

The C 1s peak (Figure 23) was fitted with two singlets: one for -CN and the other for adventitious carbon (dirt). The final E_B values were 284.7 eV for the former and 283.5 eV for

the latter, respectively. Such result is remarkable, since 283.5 eV is a literature chemical shift for -CN [63], while higher chemical shifts (284.6 eV or 284.8 eV) are usually assigned to aliphatic carbon species. The tested sample has a stoichiometric formula containing six carbon atoms. For this reason, it is considered probable that the main contribution in the C 1s comes from cyanide, not from adventitious carbon. Thus, the main singlet is for now assigned to -CN, even if it has an "incorrect" chemical shift compared to literature. The other singlet must be an unknown carbon species, since its chemical shift has too low binding energy. Therefore, there must also be some actual unfitted aliphatic carbon species contributing to the overall signal. 284.2 eV is a newly reported value for C 1s cyanide signal [69].

The Fe 2p signal did not present any interpretational problems. It should be assigned to Fe^{II} exclusively, for it cannot be reduced in UHV or by X-ray radiation. The peaks were fitted according to literature [70], which consisted on using two additional peaks along with the main one: a lower E_B pre-peak and a higher E_B surface peak. However, as Figure 24 and Figure 25 show, only the pre-peak was deconvoluted by the software. It must be specified that the doublets in the Fe 2p spectrum are due to spin-orbit coupling and not to multiplet splitting. In fact, Fe^{II} is a d^6 coordinated to CN, which is a "strong field" ligand: therefore, all six electrons are paired in the t_{2g} orbitals and none is present in the e_g orbitals. This consideration must also be applied to $K_3Fe(CN)_6$'s and $Na_2[Fe(CN)_5(NO)]$'s Fe 2p spectra. There is a little unfitted intensity on the higher binding energy side of Fe $2p_{1/2}$, but this might be considered normal, as in the case of $[Fe(CN)_6]^{4-}$ there are charge broadening effects which do not make the peak as sharp as expected [71]. This feature complicates the fitting of the signal. Because of this reason, in the powders' spectra only Fe $2p_{3/2}$ will be shown and discussed.

The final E_B for the Fe^{II} peak is 708.4 eV, perfectly matching with Grosvenor [70], and in good agreement with other values, e.g.: 708.3 eV [62], 708.1 eV [69].

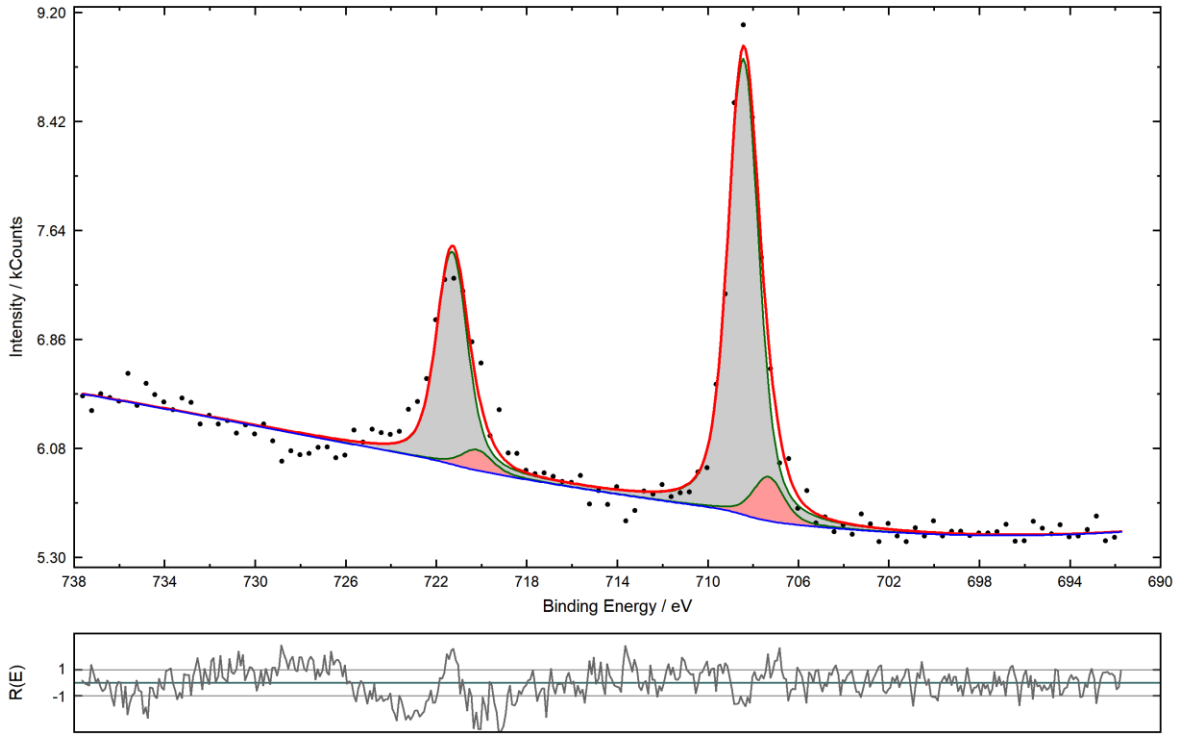

Figure 24 - $K_4Fe(CN)_6$ Fe 2p XPS detailed spectrum

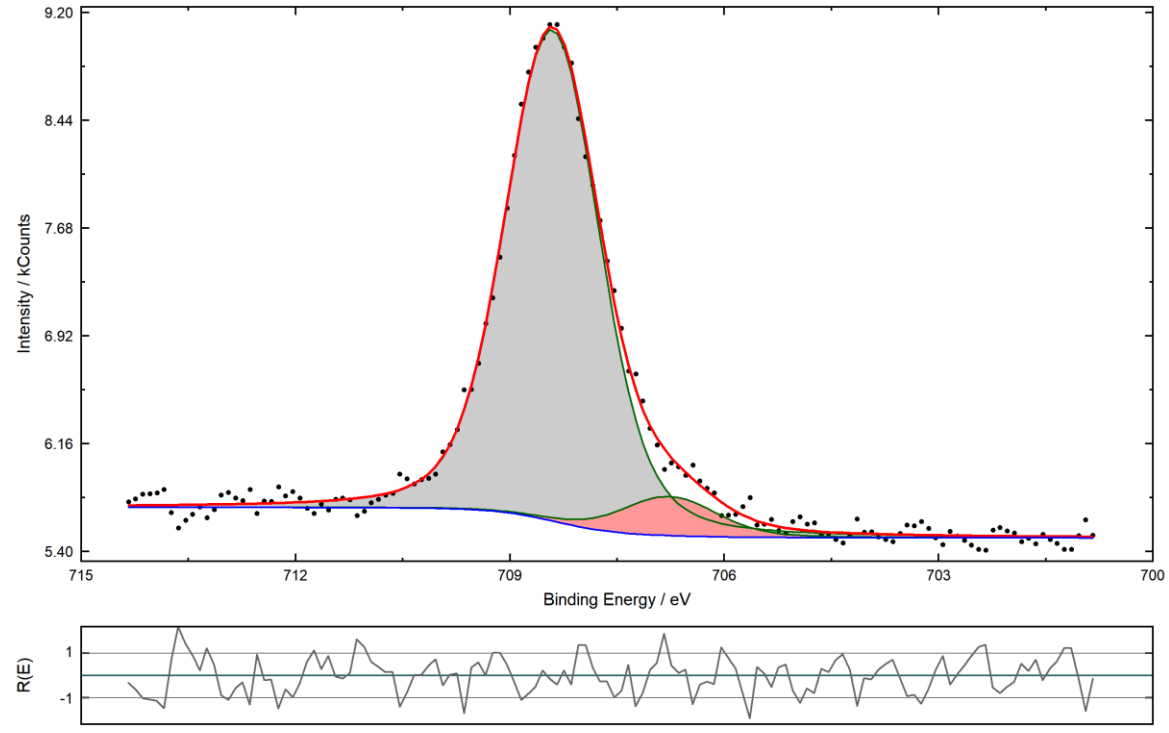

Figure 25 - $K_4Fe(CN)_6$ Fe $2p_{3/2}$ XPS detailed spectrum. The peak is a "zoom in" of Figure 24.

Finally, Figure 26 is the spectrum of the K 2p doublet. The signal corresponds to K^+. The obtained E_B values are 292.9 eV for K $2p_{3/2}$ and 295.7 eV for K $2p_{1/2}$. For K $2p_{3/2}$, 293.2 ± 0.1 eV [72] and 292.5 eV [69] were also found.

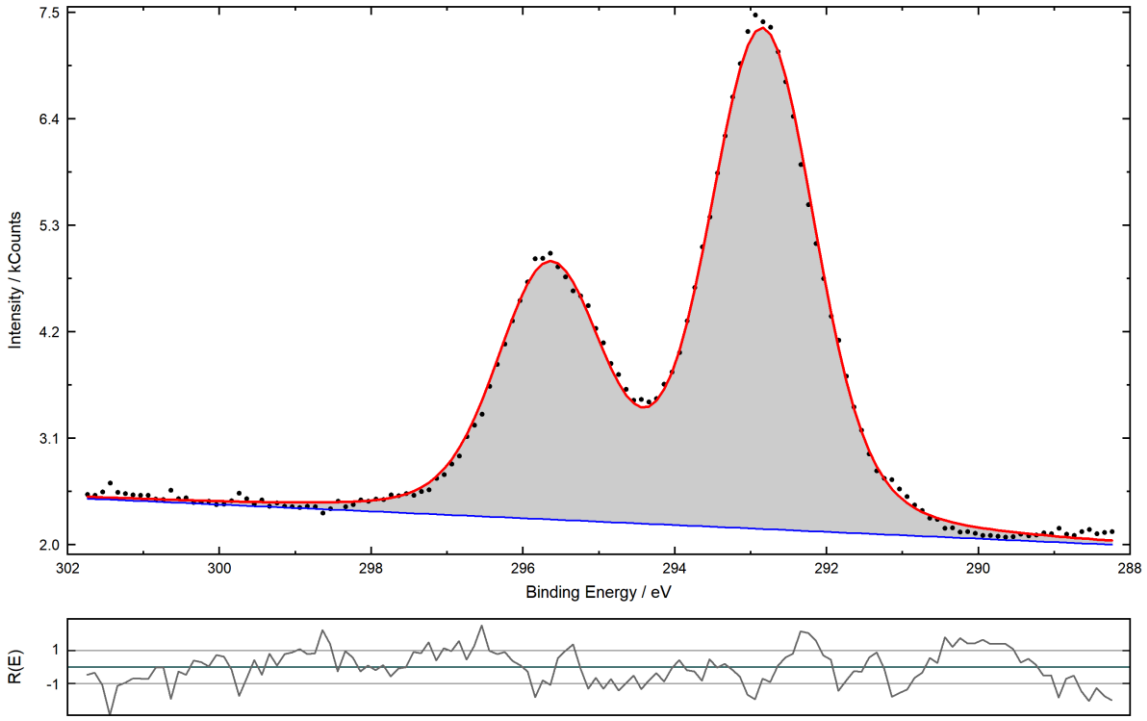

Figure 26 - $K_4Fe(CN)_6$ K 2p XPS detailed spectrum

Table 6 displays the relative elemental amounts calculated by the peaks' integration. The results do not match with the stoichiometric formula except for the N:Fe (5.7) and K:C (1:1.3) ratios, which are acceptable. C:Fe ratio is totally overestimated - 8.7 instead of 6 - and also C:N (1.53) is not corresponding to the formula. Actually, the C 1s signal is not usually reliable in quantitative analysis, since analyte and dirt peaks overlap and they cannot be properly separated. It is probably more sensible not to consider the direct quantification provided for the C 1s signal and assume the quantity of cyanide N 1s is approximately equal to the actual CN amount in the material. This approach will be adopted when discussing quantification carried out for powders. The K:Fe ratio is too large as well: 6.6 instead of 4. More potassium is found in regards to nitrogen (K:N = 1:0.85) Actually, since potassium is a light element, is highly possible that the sensitivity factor is wrongly estimated, as happens quite often with Na.

Table 6 - $K_4Fe(CN)_6$ XPS quantification table

Peak name	E_B /eV	Area/cps·eV	Sens. Fact.	Norm. Area	Quant./at.%	
C 1s K4Fe(CN)6	284.72	4125.222	16.8	245.5489	37.81	42.07
C 1s -CH2-	283.5	464.6359	16.796	27.66348	4.26	
Fe 2p Fe 2+	708.44	8035.377	312.15	25.74171	3.96	4.35
Fe 2p	707.34	780.7931	311.88	2.503473	0.39	
N 1s - CN	397.6	4995.043	31.08	160.7157	24.75	24.75
K 2p	292.85	12499.46	66.769	187.2046	28.83	28.83

4.3.1.2 $K_3Fe(CN)_6$

As they contain the same elements, $K_3Fe(CN)_6$'s survey spectrum is very similar to $K_4Fe(CN)_6$'s – even though $K_3Fe(CN)_6$ should not contain any coordination water. Along with the expected elements, oxygen was detected as well, probably present as carboxylate from fatty acids (adventitious carbon from diffusion pumps).

Figure 27 shows N 1s's spectrum. The peak is a clear -CN singlet. 397.7 eV was another reported E_B value [69].

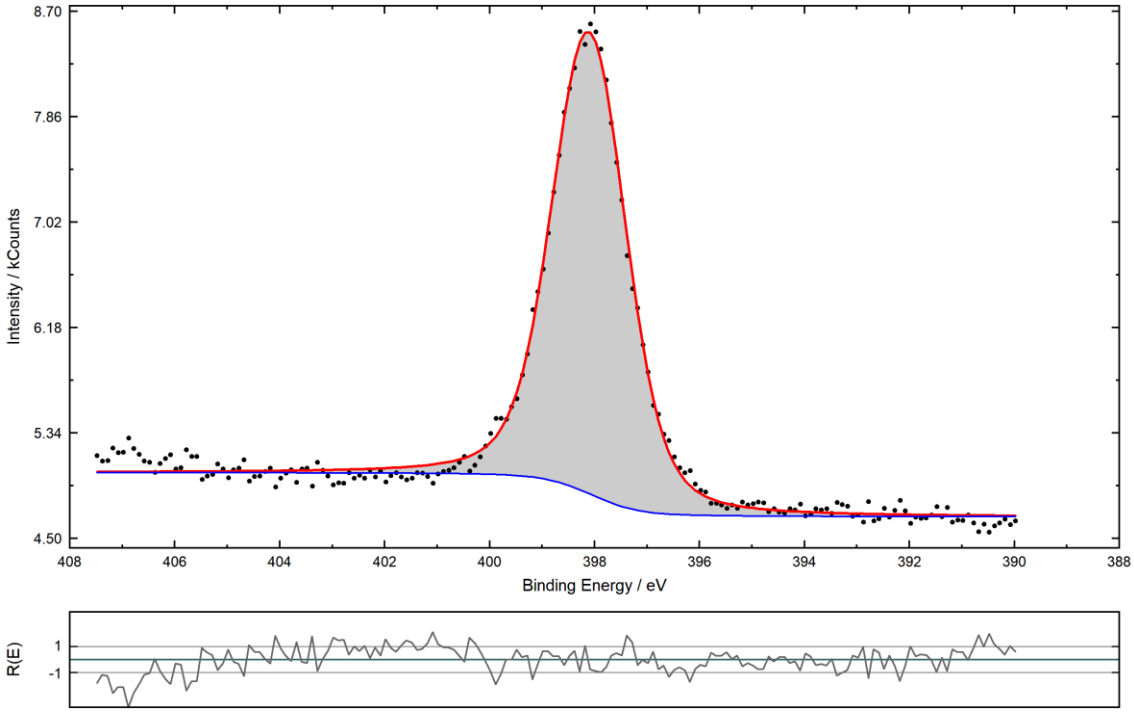

Figure 27 - $K_3Fe(CN)_6$ N 1s XPS detailed spectrum

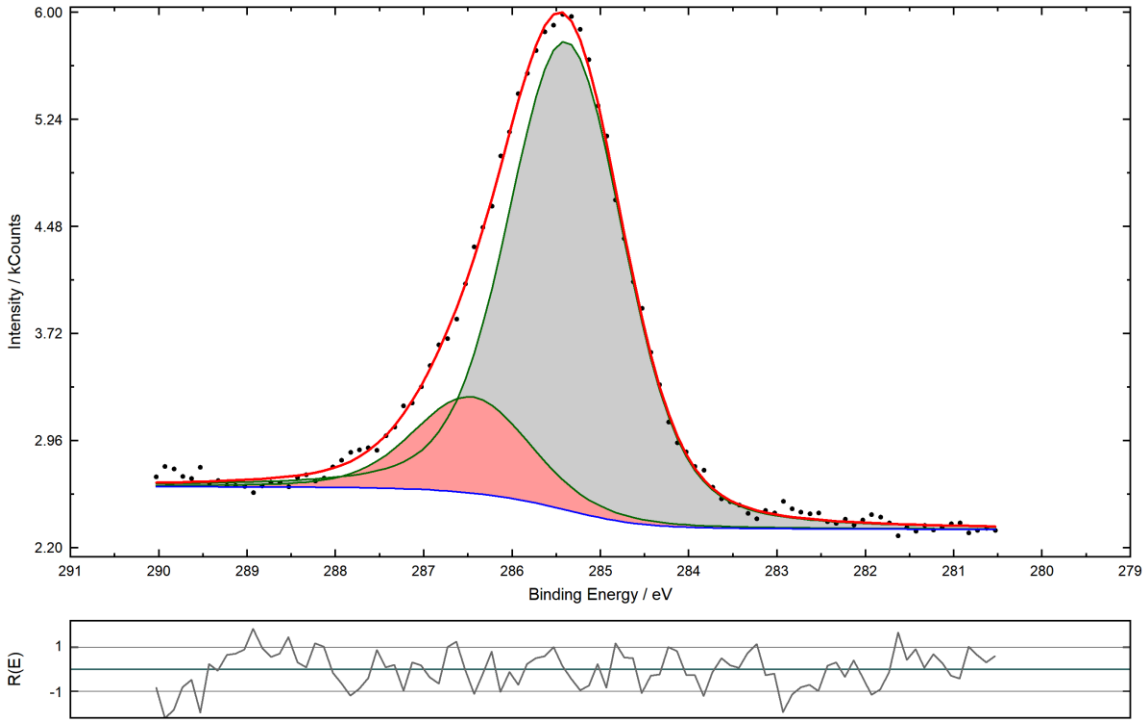

Figure 28 - $K_3Fe(CN)_6$ C 1s XPS detailed spectrum

The C 1s spectrum (Figure 28) was fitted setting two singlets, just as with $K_4Fe(CN)_6$: the -CN signal and an unknown carbon species. The resulting E_B are 285.4 eV for the former and 286.5 eV for the latter signal. The -CN's E_B value is again in contrast with the one given by Vannerberg, 283.9 eV - such discrepancy was a leading factor in suspecting some differential charging to happen during the measurement. When such phenomenum occurs, different areas of the surface have a deviating equilibrium charge during X-Ray irradiation. Another reported value for C 1s -CN is 284.3 eV [69]. 286.5 eV falls well in the organic oxidized carbon chemical shift range.

Figure 29 displays Fe 2p signal. The main signal consisted of at least two components: one at 710.5 eV, and the other at 708.7 eV. Cano et al. [69] found 709.8 eV for Fe^{III} and 707.9 eV for Fe^{II}, while Oku [73] reported 709.9 ± 0.2 eV for Fe^{III} and 708.3 ± 0.1 eV for Fe^{II}. The peak at 710.5 eV is therefore assigned to Fe^{III}, whereas the one at 708.7 eV at Fe^{II} - due to inevitable Fe^{III} reduction after exposure to X-rays [73]. Computation of three peaks provided a better fitting than with only two of them and it is common practice to fit iron signals with more peaks (satellites), so the higher E_B peak (at 711.9 eV) could still be attributed to Fe^{III}. The same considerations made in regards to spin-orbit coupling and to charge-broadening effects in the case of $K_4Fe(CN)_6$'s Fe 2p could be done even with $[Fe(CN)_6]^{3-}$, as Fe $2p_{1/2}$ signal is a very broad signal indeed.

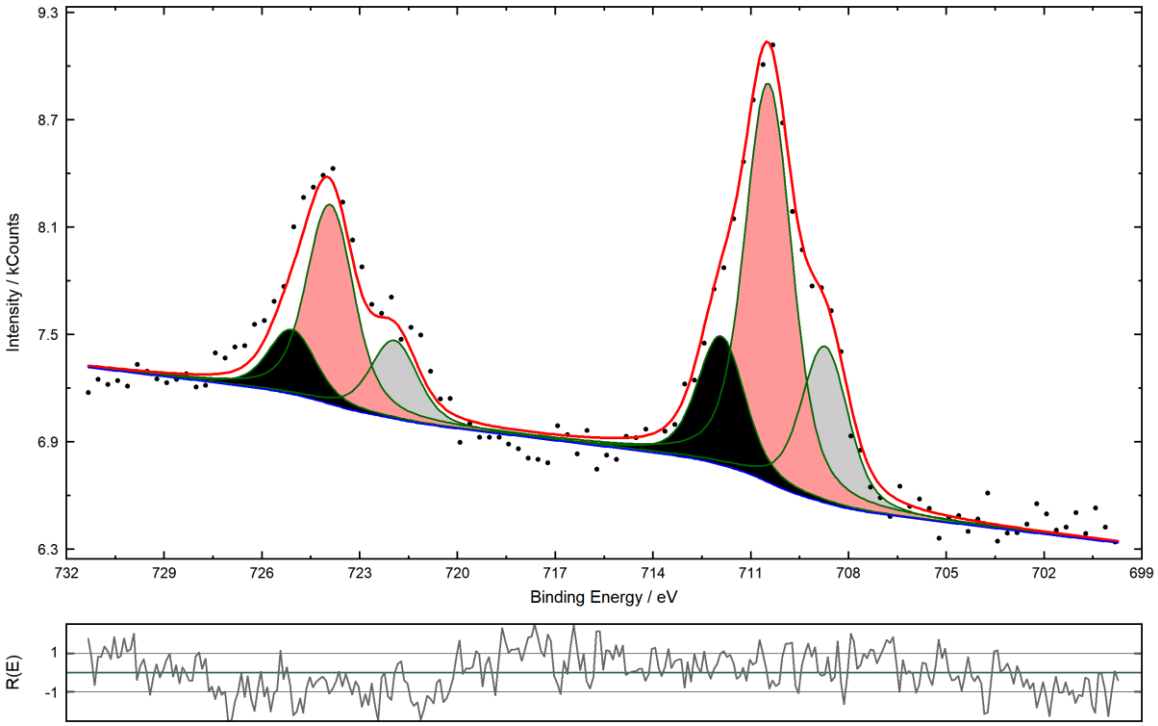

Figure 29 - $K_3Fe(CN)_6$ Fe 2p XPS detailed spectrum

K 2p spectrum will not be shown, for it is extremely similar to the one for K^+ in $K_4Fe(CN)_6$. The resulting E_B values are 293.4 eV for K $2p_{3/2}$ and 296.1 eV for K $2p_{1/2}$. Vannerberg reports 291.9 eV for K $2p_{3/2}$ though [63]. Other values include 292.3 eV [69].

A quantification table is provided in Table 7. Again, Fe:N (1:5.2) is satisfying, along with K:N (1:1.3). K:Fe is quite good this time (3.9). C:Fe is again overestimated (8.1). C:N ratio is 1.55. Yet the overall results match way better with the stoichiometric compound formula than in the previous measurement.

Table 7 - $K_3Fe(CN)_6$ XPS quantification table

Peak name	E_B /eV	Area/cps·eV	Sens. Fact.	Norm. Area	Quant./at.%	
C 1s K3Fe(CN)6	285.39	5083.485	16.792	302.7325	40.51	49.35
C 1s -CH2-	286.46	1043.724	15.8	66.05846	8.84	
Fe 2p Fe 2+	708.73	2316.681	311.94	7.426663	0.99	5.01
Fe 2p Fe 3+ main	710.46	5909.271	259.72	22.7522	3.04	
Fe 2p Fe 3+	711.92	1908.914	259.61	7.352891	0.98	
N 1s -CN	398.11	6085.361	31.08	195.7967	26.2	26.2
K 2p	293.38	9705.345	66.816	145.2548	19.44	19.44

4.3.1.3 $Na_2Fe(CN)_5(NO)$

As stated in the experimental section, $Na_2[Fe(CN)_5(NO)]$'s spectrum was recorded twice, without and with flood gun. The latter spectra were recorded to understand if differential charging phenomena were occurring. But since both sets of spectra are very similar in regards of shape of peaks and chemical shift, only spectra without flood gun will be shown. A table comparing the resulting bonding energies from both measurements will be provided as well. Quantification tables from both measurements will also be included.

Figure 30 is the sample's survey spectrum. Every expected element can be assigned and no impurities are detected.

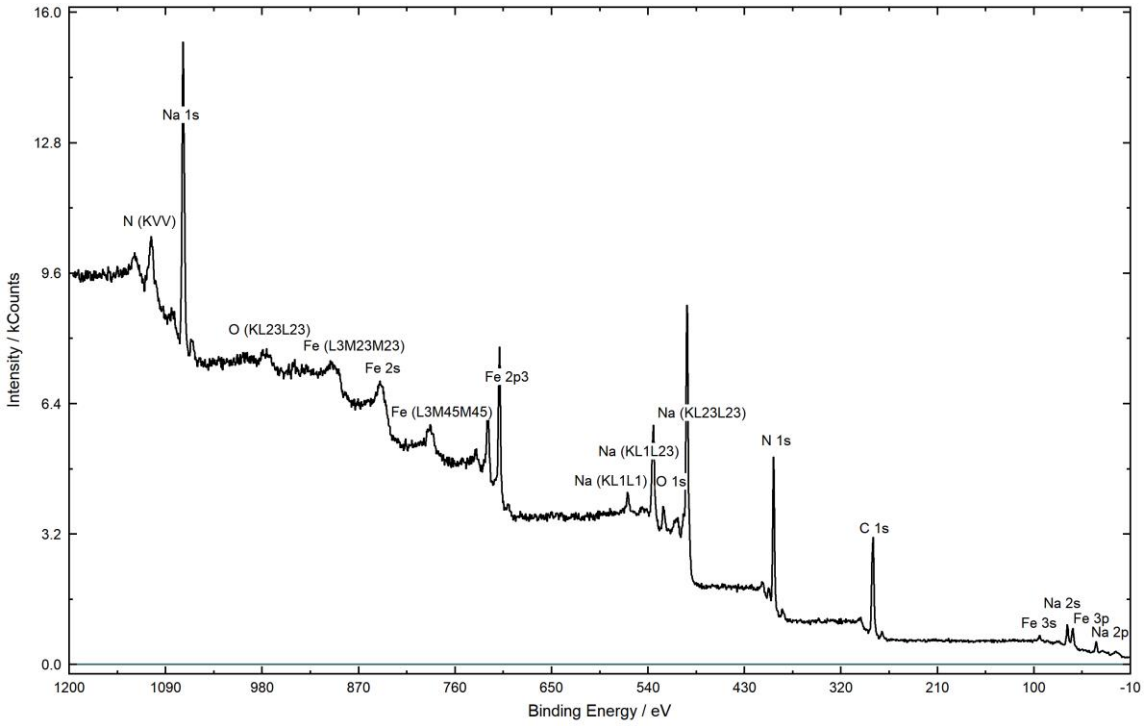

Figure 30 - $Na_2[Fe(CN)_5NO]$ XPS survey spectrum

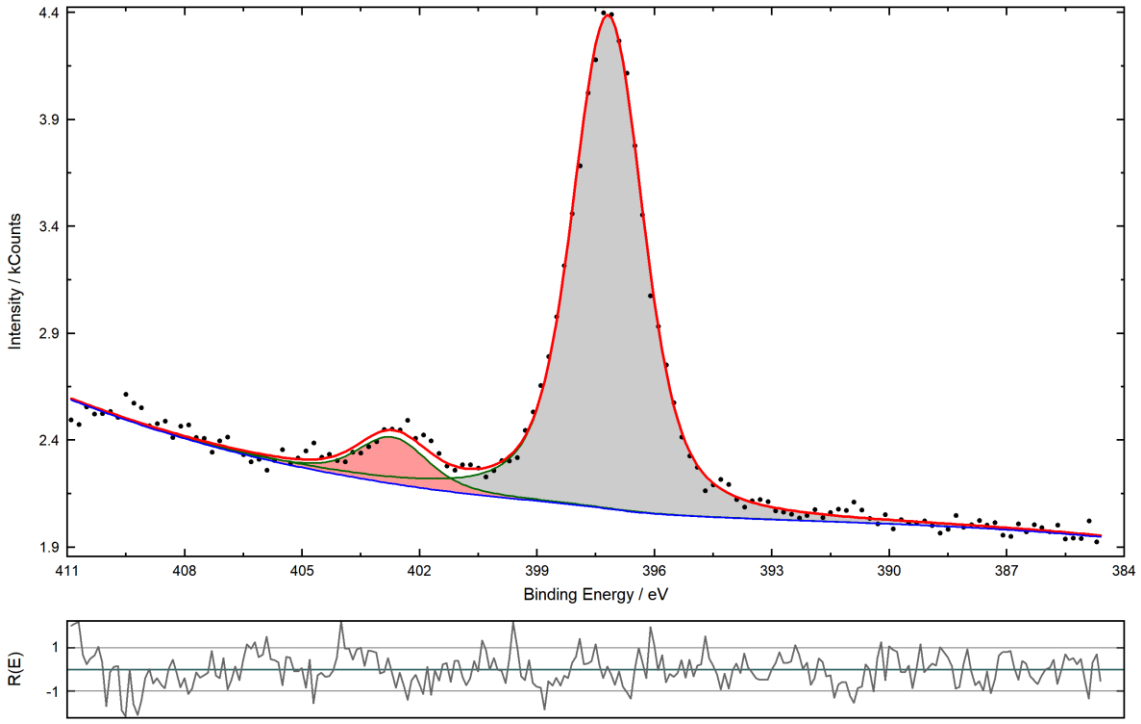

Figure 31 - $Na_2[Fe(CN)_5NO]$ N 1s XPS detailed spectrum

The N 1s spectrum (Figure 31) clearly shows two signals: the -CN high intensity signal at 397.2 and the -NO signal at 402.7 eV. Oku et al. [74] report 398.8 eV for the former and 402.9 eV for the latter. A more recent article reports 397.5 eV for -CN and 402.5 eV for -NO [30].

Figure 32 shows the C 1s peak, at 284.1 eV, whose intensity is related to both cyanide and adventitious carbon. It must be noted that this fitting was made by setting two possible peaks, -CN and adventitious carbon - which was not deconvoluted. Therefore, even in the case of nitroprusside, these two species might be overlapped. Oku et al. [74] came to the same conclusion.

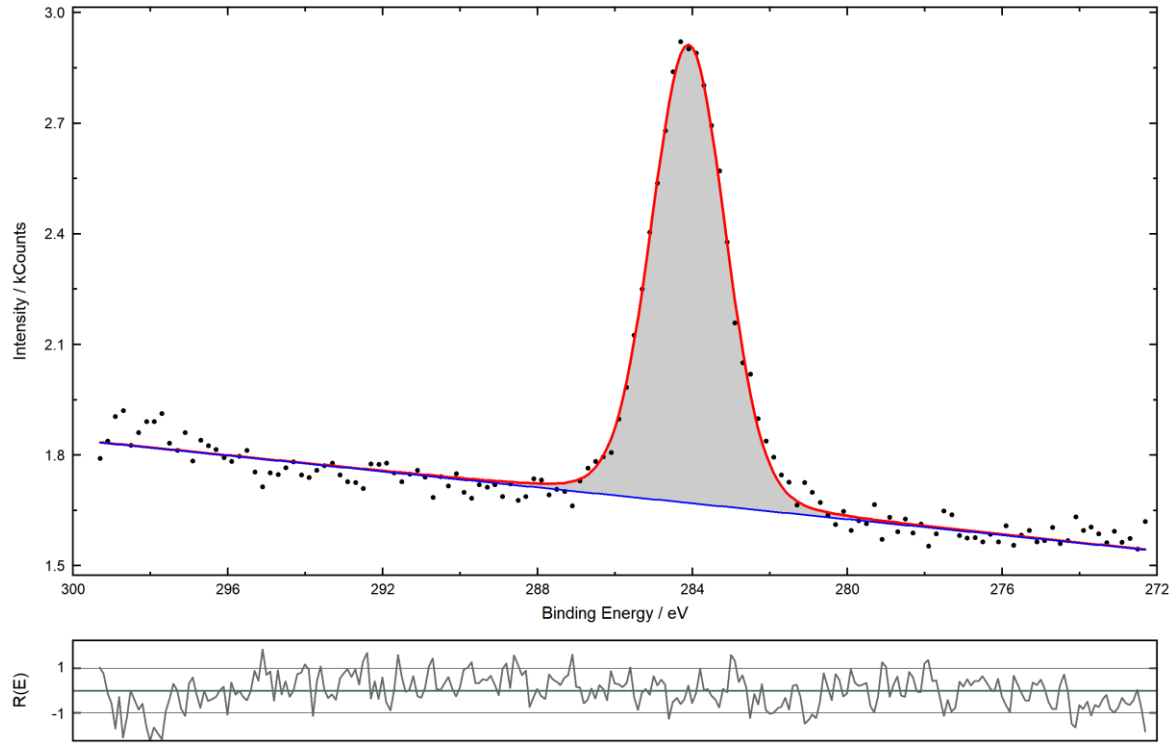

Figure 32 - $Na_2[Fe(CN)_5NO]$ C 1s XPS detailed spectrum

Fe 2p spectrum is displayed in Figure 33. The fitting was achieved with two doublets. Some unfitted intensity on the higher binding energy side of the Fe $2p_{1/2}$ peak can be still seen though - charge broadening effects probably remain even with iron nitroprussiate. Resulting binding energies for Fe $2p_{3/2}$ peak are 709.9 eV for Fe^{II} and 707.9 eV. While the main peak at 709.9 eV can be attributed to Fe^{II}, the identity of the second peak is less clear: while Oku et. al [74] suggest it is related to a possible degradation product such as $[Fe^{II}(CN)_5]^{3-}$ - either hydrated or not – due to X-Ray irradiation. NO^+ would be reduced to NO, which is desorbed in UHV. Cano et al. [30] found two extra peaks – much smaller than those obtained in Figure 33 - corresponding to high-spin Fe^{II}-$(NC)_x$ (at 709.1 eV) and to Fe^0 (at 707.3 eV). These species are thought to be produced by X-Ray irradiation under conventional conditions, after decomposition of the nitroprusside building block [30]. The peak at 707.9 eV may be probably associated to Fe^{II}, since 707.9 eV is too high for metallic Fe, which is usually found between 706.7 eV and 707.2 eV [51]. Yet, it is not possible to state which compound that peak is exactly representative of. Other E_B values for the Fe $2p_{3/2}$ nitroprusside peak are: 709.5 eV [62], 710.1 eV [30] and 710.6 eV [74]. Nevertheless, these higher binding energy values than those related to $[Fe^{II}(CN)_6]^{4-}$ hint to lower electron density on the Fe^{II} atom in nitroprusside.

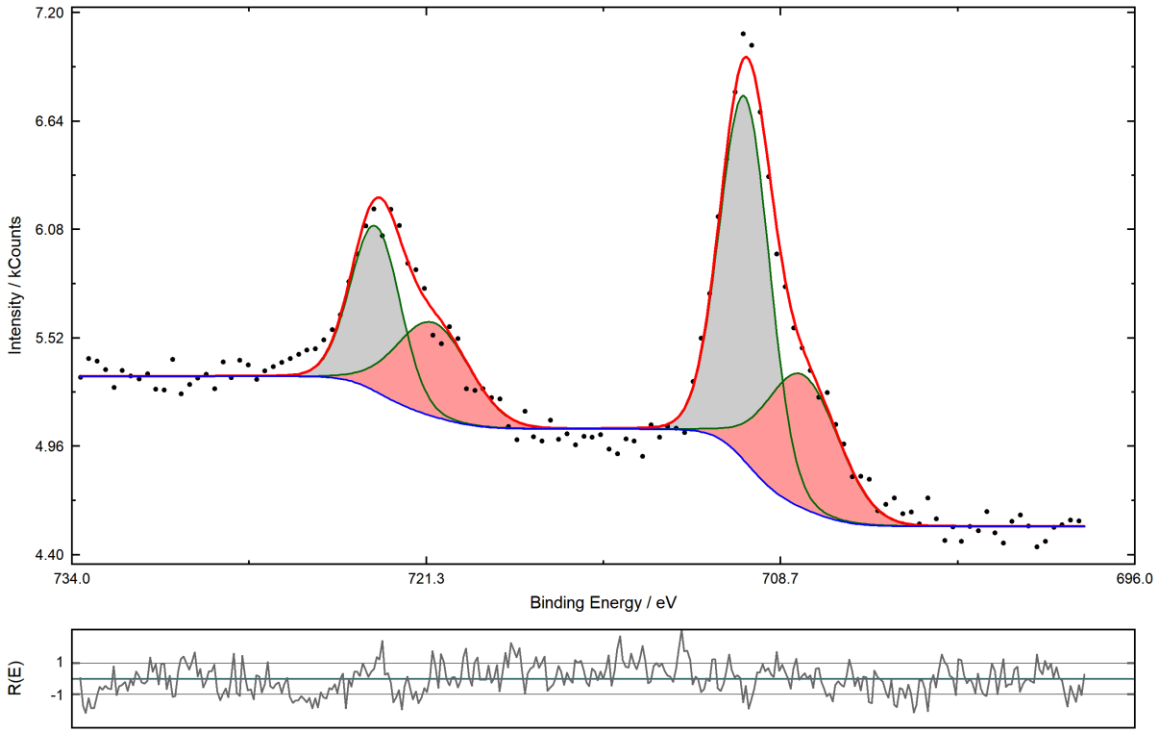

Figure 33 - $Na_2[Fe(CN)_5NO]$ Fe 2p XPS detailed spectrum

A sharp singlet at 1070.6 eV is detected for Na 1s signal in Figure 34, which corresponds to Na^+. The value is in good correspondence with 1070.9 eV, the only E_B found in literature [30].

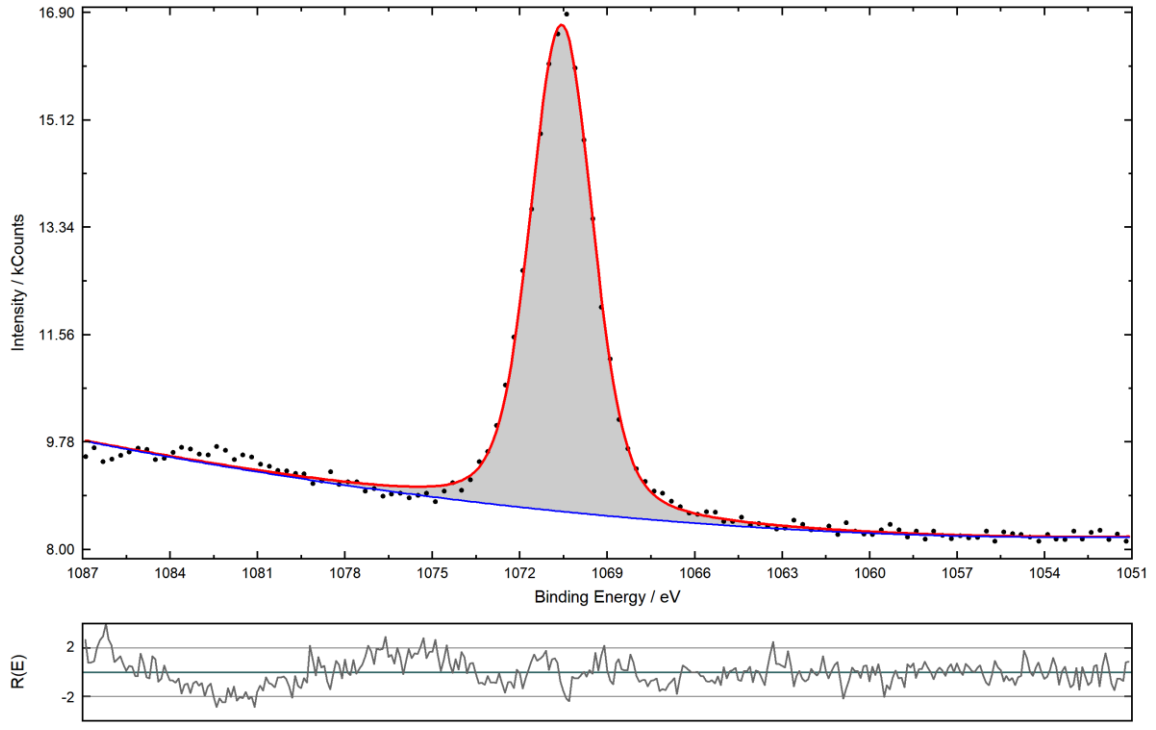

Figure 34 - $Na_2[Fe(CN)_5NO]$ Na 1s XPS detailed spectrum

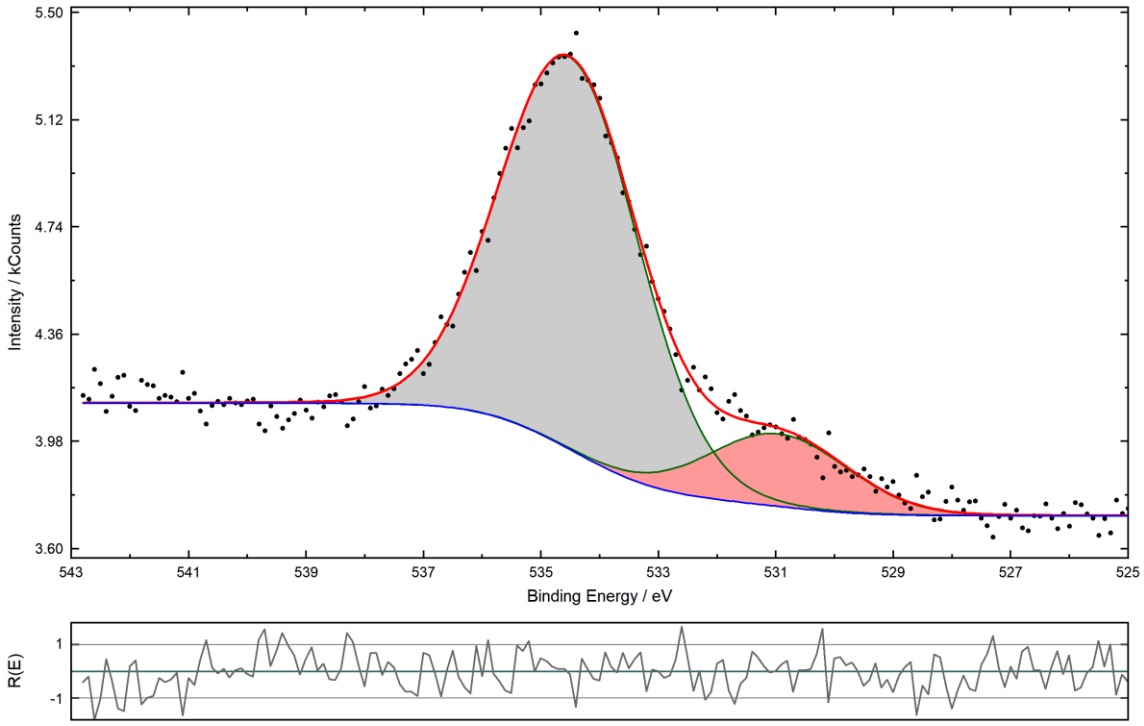

Figure 35 - $Na_2[Fe(CN)_5NO]$ O 1s XPS detailed spectrum: Na KLL (grey peak) and O 1s (red peak) are shown

A Na KLL Auger lines overlaps with the O 1s signal (Figure 35). It was not possible to overcome this, since switching to Mg Kα would provide an oxygen KLL Auger line at 745 eV [51], causing interference with the Fe 2p ½ peak. Since Fe 2p was prioritized over O 1s, Al Kα was still used. The O 1s' experimental binding energy is 531.0 eV, which was attributed to nitrosyl group. A value for nitrosyl reported in literature is 531.6 eV [30].

A quantification table without and with flood gun are represented in Tables 8 and 9 respectively. Flood gun does not change significantly the binding energies (Table 10), which makes comparison between quantitative results more reliable. The most striking difference in respect to previous quantitative analyses lies in the cyanide approximate C:N 1:1 ratio (1:1.08 in the untreated sample and 1:0.94 with flood gun), since adventitious carbon was supposed to be contributing to the C 1s signal. Nitrosyl group N:O ratio also matches good (1:0.8 for untreated sample and 1:1.3 with flood gun). C:Fe (5.7 for untreated sample and 6.3 with flood gun) is again slightly overestimated . N:Fe (CN and NO) is a bit overestimated for the untreated sample (6.7), yet well matched for the flood gun measurement (6.3). The amount of Na is overestimated both in regards to C (1:1.5 in untreated sample and 1:1.4 with flood gun instead of ideally 1:2.5) and to N (1:1.7 in untreated sample and 1.4 with flood gun instead of ideally 1:3). This also happened before with the quantitative analysis of K. This persistent overestimation could be due to these alkali metal being light-weight.

Table 8 - no flood gun $Na_2[Fe(CN)_5NO]$ XPS quantification table

Peak name	E_B /eV	Area/cps·eV	Sens. Fact.	Norm. Area	Quant./at.%	
C 1s_ 11 C 1s	284.1	2580.487	16.788	153.7102	28.22	28.22
C 1s_ 11 Peak 2	286.1	0	16.792	0	0	
Fe 2p_ 12 Fe 2p3	709.94	5165.962	312.21	16.54643	3.04	4.93
Fe 2p_ 12 Fe 2p1	707.89	3211.742	312.12	10.28992	1.89	
N 1s_ 14 N1s CN	397.19	5148.592	31.096	165.5709	30.39	33.26
N 1s_ 14 N 1s NO	402.69	485.6767	31.116	15.60858	2.87	
Na 1s_ 15 Na 1s	1070.57	20265.69	193.58	104.6868	19.22	19.22
O 1s_ 16 O 1s	534.52	3472.279	52.585	66.03175	12.12	14.38
O 1s_ 16 Na (KL1L23)	530.96	646.3146	52.539	12.30161	2.26	

Table 9 - flood gun $Na_2[Fe(CN)_5NO]$ XPS quantification table

Peak name	E_B /eV	Area/cps·eV	Sens. Fact.	Norm. Area	Quant./at.%	
C 1s_ 11 C 1s	284.09	2911.017	16.788	173.3987	30.16	30.16
C 1s_ 11 Peak 2	286.39	0	16.804	0	0	
Fe 2p_ 12 Fe 2p3	709.91	5495.415	312.21	17.60166	3.06	4.75
Fe 2p_ 12 Fe 2p1	707.46	3030.582	311.88	9.717017	1.69	
N 1s_ 14 N 1s	397.2	5047.624	31.096	162.3239	28.24	29.91
N 1s_ 14 N 1s NO	402.5	299.4411	31.116	9.623381	1.67	
Na 1s_ 15 Na 1s	1070.75	24185.85	193.45	125.0225	21.75	21.75
O 1s_ 16 O 1s	534.67	3415.857	52.585	64.95878	11.3	13.43
O 1s_ 16 Na (KL1L23)	531.37	643.3273	52.508	12.25199	2.13	

In Table 10, comparison between the binding energies is provided. N1s -CN will not be represented since it was charge corrected to 397.2 eV in both measurements, as stated.

Table 10 – E_B comparison for $Na_2[Fe(CN)_5NO]$ signals between measurements without and with flood-gun

	C 1s -CN	**Fe $2p_{3/2}$ nitroprusside**	**Fe $2p_{3/2}$**	**N 1s -NO**	**Na 1s**	**O 1s -NO**
No flood gun (eV)	284.1	709.9	707.9	402.7	1070.6	531.0
Flood gun (eV)	284.1	709.9	707.5	402.5	1070.8	531.4

As already stated, judging from the binding energies, flood gun measurement did not alter the results. In conclusion, no differential charging happens with powders and analysis of chemical shift just needs to take into account charging on the sample due to the fact that they are not totally conductive, other factors and several reference results.

4.3.2 MnFeA02

Figure 36 shows the survey spectrum for MnFeA02. Every expected element is present and no impurities were detected.

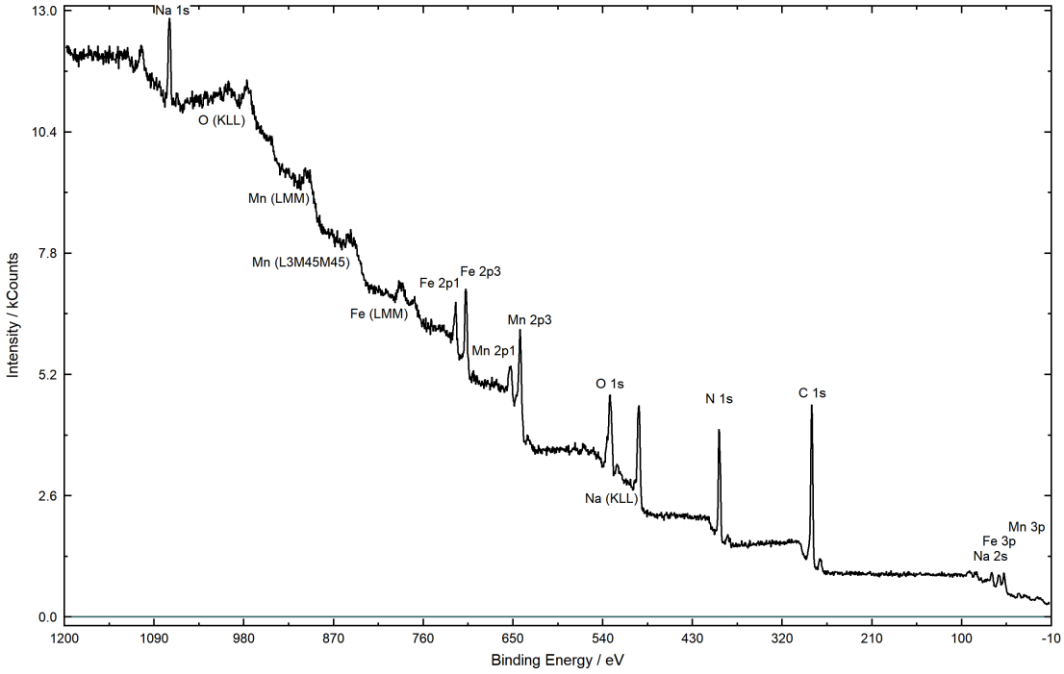

Figure 36 - MnFeA02 XPS survey spectrum

Mn valence states are deemed difficult to distinguish with XPS data [75], [76]. Therefore, choice of suitable references is a crucial step when dealing with the interpretation of such spectra. Wang et. al [76] deposited a composite structure of MnHCF and MnO_2 and investigated the material with XPS. They fitted the $Mn2p_{3/2}$ peak with three singlets, belonging to Mn^{II} (at 640.8 eV), Mn^{III} (641.5 eV) and Mn^{IV} (642.4 eV). Since a Mn^{II} salt was the only source of Mn for the synthesis of our material, Mn 2p spectrum (Figure) was fitted with two doublets and the presence of Mn^{IV} was excluded. Agarwal et. al [77] detected two peaks in the Mn 2p spectrum for a Prussian Blue – MnHCF nanocomposite: they attributed the peak at 641.3 eV to Mn^{III} and the other one at 643.6 eV to Mn^{IV}.

Mn $2p_{3/2}$ main peak was found at 641.8 eV and the minor peak at 646.3 eV (Figure 37). The main peak was consequently attributed to Mn^{III} only and no specific chemical interpretation was given to the minor peak, yet its E_B is too high to belong to some Mn^{IV}. As Mn^{III} coordinated to nitrogen would be a d^4 in a high-spin environment, the minor peaks could easily belong to a satellite. In addition, Mn^{III} would fit perfectly in the basic hexacyanoferrate formula as $NaMn^{III}[Fe^{II}(CN)_6]$, assuring charge neutrality.

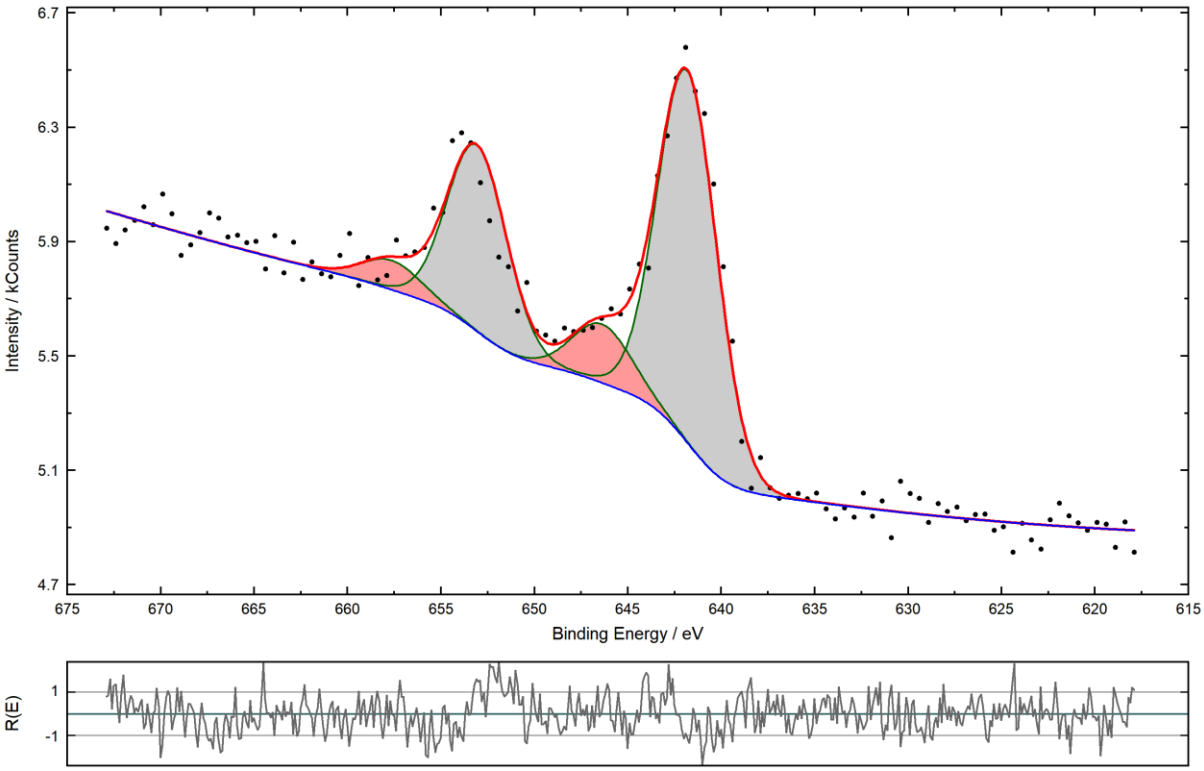

Figure 37 - MnFeA02 Mn 2p XPS detailed spectrum

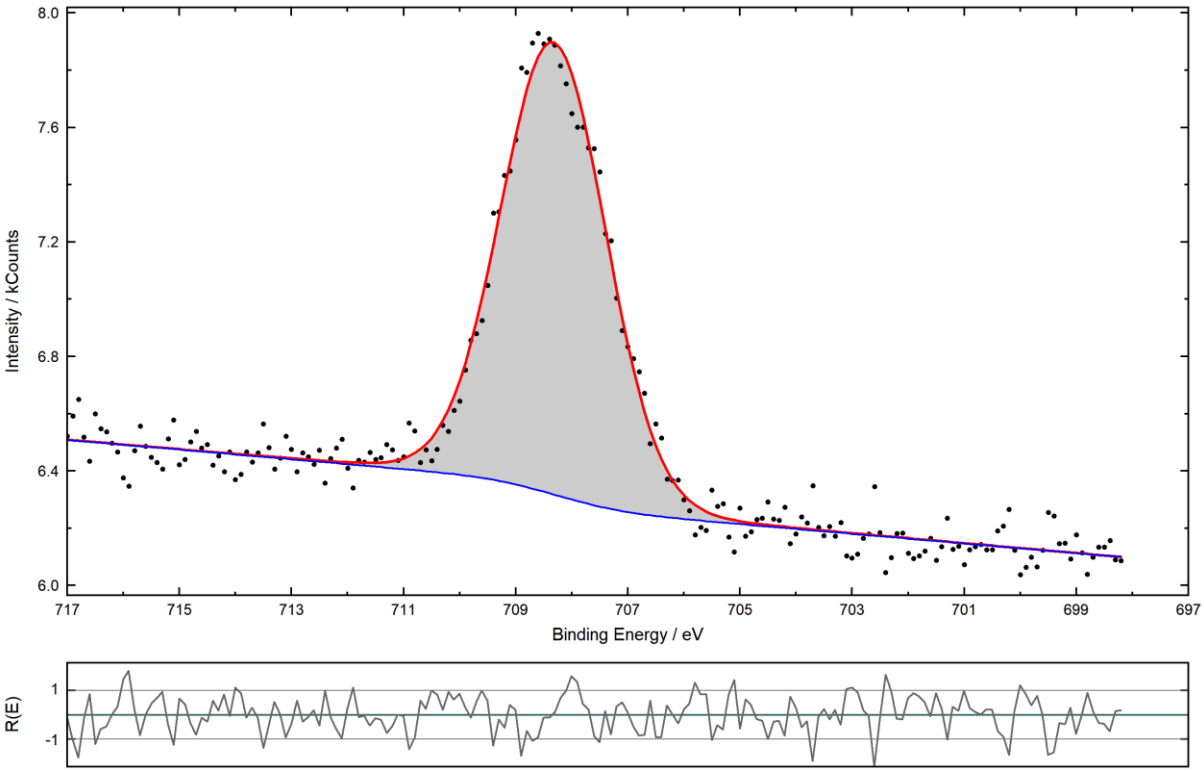

Figure 38 – MnFeA02 Fe $2p_{3/2}$ XPS detailed spectrum

The Fe $2p_{3/2}$ belonging to this sample was fitted with one singlet (Figure 38). The resulting E_B was found at 708.3 eV, a typical value for Fe^{II} species. Wang et. al [76] found 708.5 eV as chemical shift for Fe $2p_{3/2}$ and attributed it to Fe^{II}.

Figure 39 shows the N 1s spectrum. Since charge correction was performed on N 1s main peak (397.6 eV), which is attributed to cyanide, the identity of the minor peak (at 401.2 eV) is unknown up to know. Similar binding energies are usually attributed to ammonium salts or to amine functionalities [51].

The C 1s spectrum (Figure 40) also presented an extra peak at higher binding energies (287.9 eV). This value is, even in this case, attributed to organic carbon [51]. The main peak, at 284.5 eV was attributed to cyanide, yet the chemical shift is very close to the one related to adventitious carbon – which may be contributing to the signal.

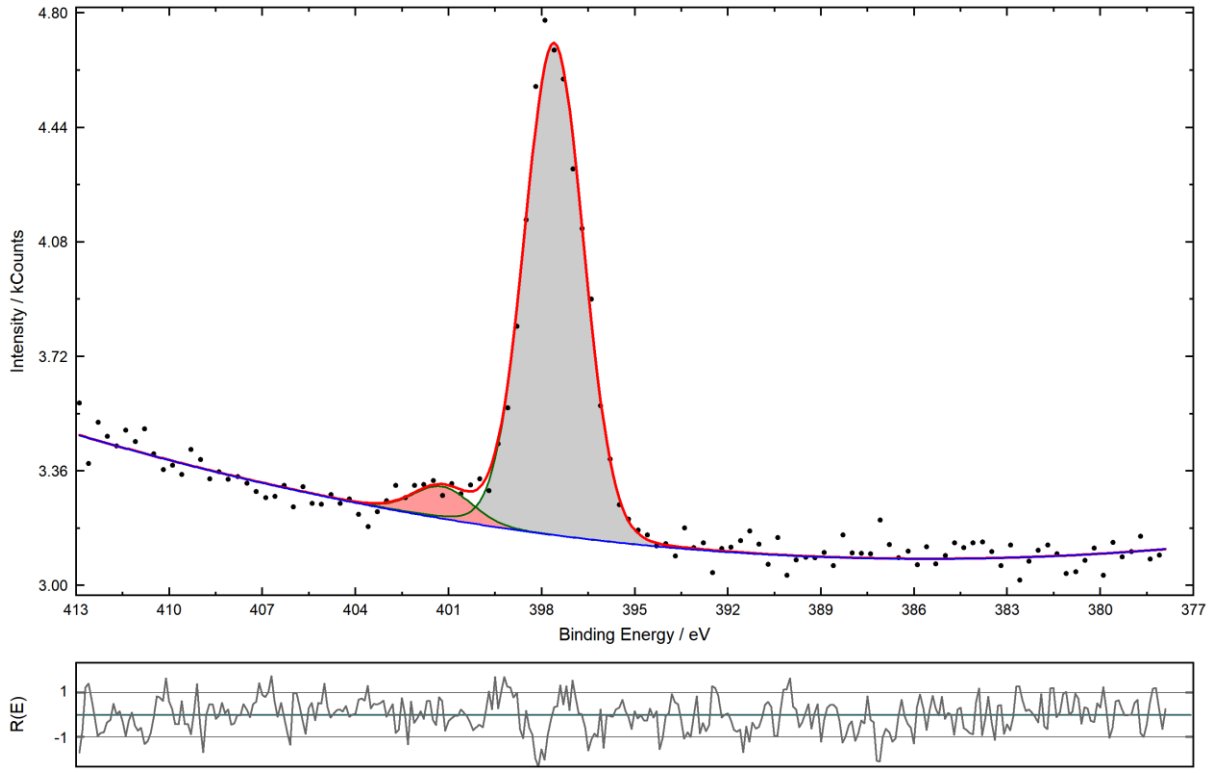

Figure 39 – MnFeA02 N 1s XPS detailed spectrum

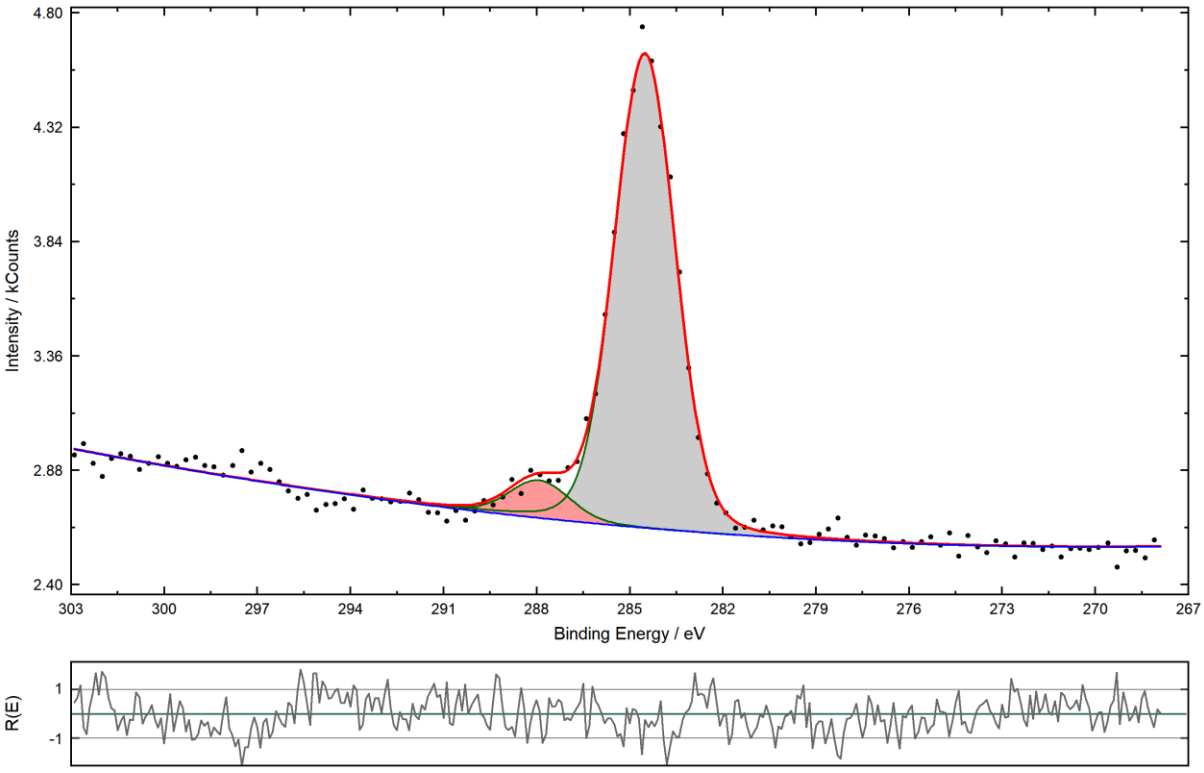

Figure 40 - MnFeA02 C 1s XPS detailed spectrum

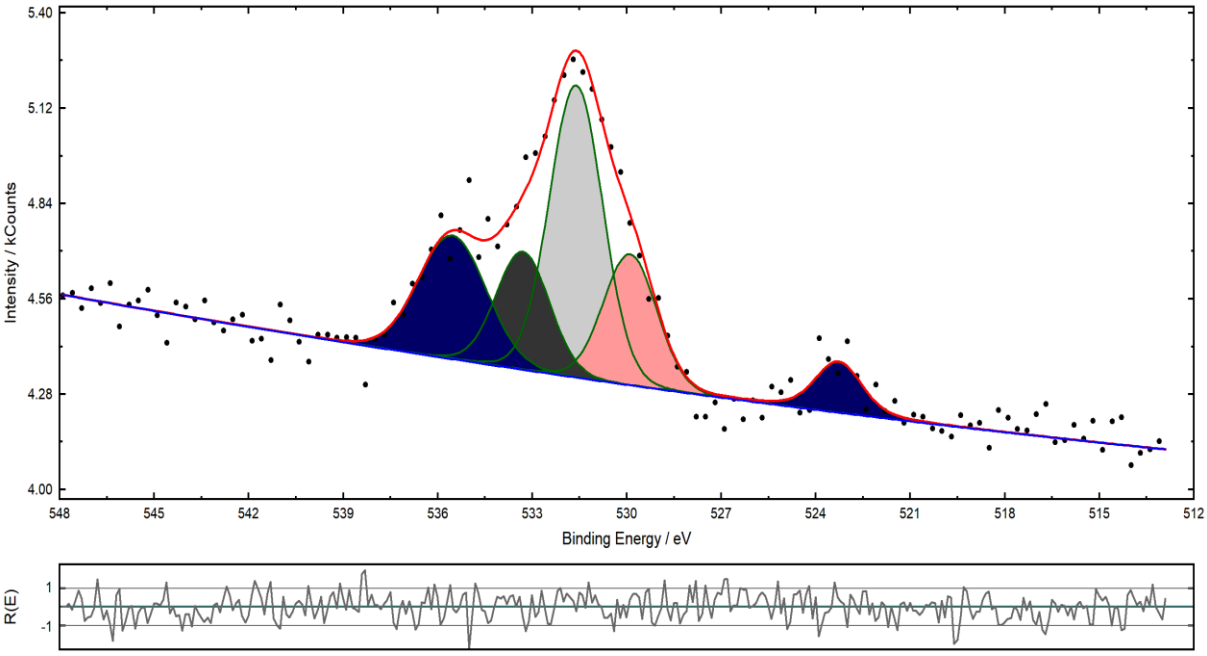

Figure 41 – MnFeA02 O 1s XPS detailed spectrum: organic oxygen compounds (grey), iron oxides (pink), water (dark grey), Na KLL Auger lines (blue)

The O 1s signal is displayed in Figure 41. This spectrum could be deemed as representative for every powder O 1s spectrum recorded in this work (apart from reference compounds). The Na KLL are present every time the counterion for the synthesized powder is Na^+.

Nevertheless, three species containing oxygen are detected: carbonyl-containing compounds at 531.7 eV – 531.9 eV (probably from fatty acids contamination), iron oxides at 529.8 eV – 530.0 eV and coordination water at 533.1 eV – 533.3 eV.

Table 11 is the quantification table for the sample. Mn:Fe ratio is 1.86, a larger value than the one found with AES (Section 3.1.2). Na:Fe ratio is 1.5, slightly higher than 1.3, yet acceptable. To estimate the Fe:N ratio, only the amount of nitrogen from the cyanide-assigned peak will be taken into account: the resulting value is 1:6.38, a value very close to the theoretical stoichiometry for this class of compounds.

Table 11 – MnFeA02 XPS quantification table

Peak name	E_B /eV	Area/cps·eV	Sens. Fact.	Norm. Area	Quant./at.%	
C 1s Peak 1	284.52	4243.392	16.78	252.8839	56.45	60.93
C 1s Peak 2	287.92	337.2437	16.807	20.06567	4.48	
N 1s Peak 1	397.61	3110.147	31.08	100.0691	22.34	23.79
N 1s Peak 2	401.21	201.9939	31.116	6.491641	1.45	
Na 1s Peak 1	1071.74	4570.468	193.71	23.59426	5.27	5.27
Fe 2p3 Peak 1	708.7	2001.094	205.55	9.735079	2.17	3.5
Fe 2p3 Peak 2	707.59	1225.537	205.51	5.963191	1.33	
Mn 2p Doublet 1	641.82	6515.976	258.22	25.23371	5.63	6.52
Mn 2p Doublet 2	646.38	1026.852	258.52	3.971902	0.89	

4.3.3 MnFeA03

In the survey spectrum for MnFeA03 (Figure 42) Si was also detected – as shown by the presence of Si 2s and Si 2p peaks. This impurity might possibly come from bits of glass broken during centrifugation steps, which are necessary to purify the product.

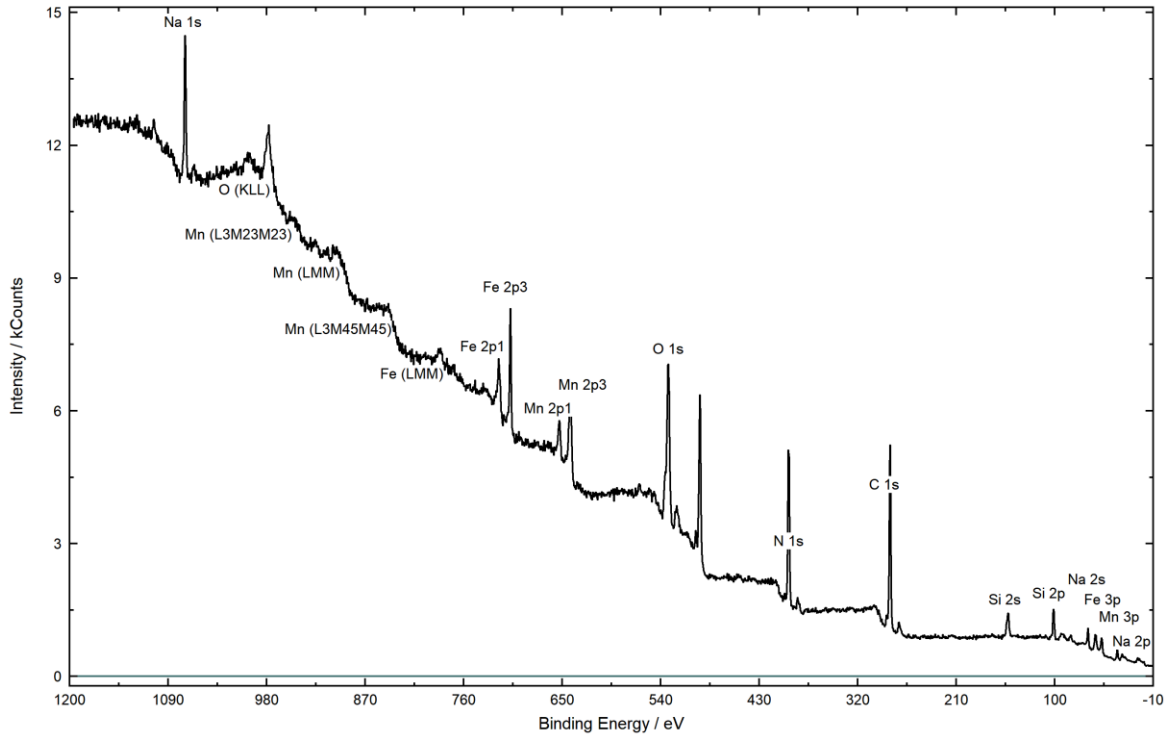

Figure 42 – MnFeA03 XPS survey spectrum

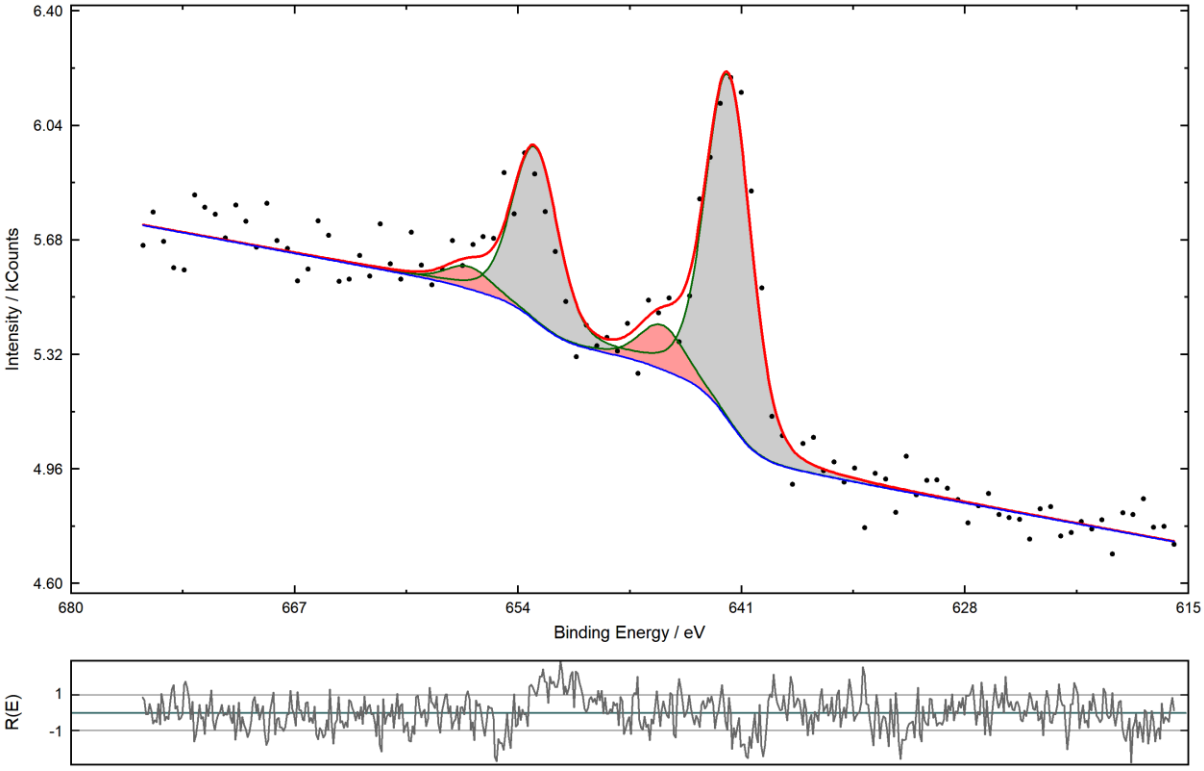

Figure 43 – MnFeA03 Mn 2p XPS detailed spectrum

Figure 43 displays the Mn 2p spectrum. It was fitted with two doublets like MnFeA02. The Mn $2p_{3/2}$ main peak was found at 641.8 eV, while the minor one at 645.6 eV. The given

interpretation was the same as MnFeA02: the main peak was attributed to Mn^{III} and the minor peak could possibly be a satellite.

The Fe $2p_{3/2}$ signal (Figure 44) was fitted with one single peak, whose E_B was found at 708.4 eV. The interpretation was straightforward: the oxidation state of Fe in the compound can be attributed to be Fe^{II}.

The N 1s and C 1s signals did not present any extra peaks, in contrast with MnFeA02.

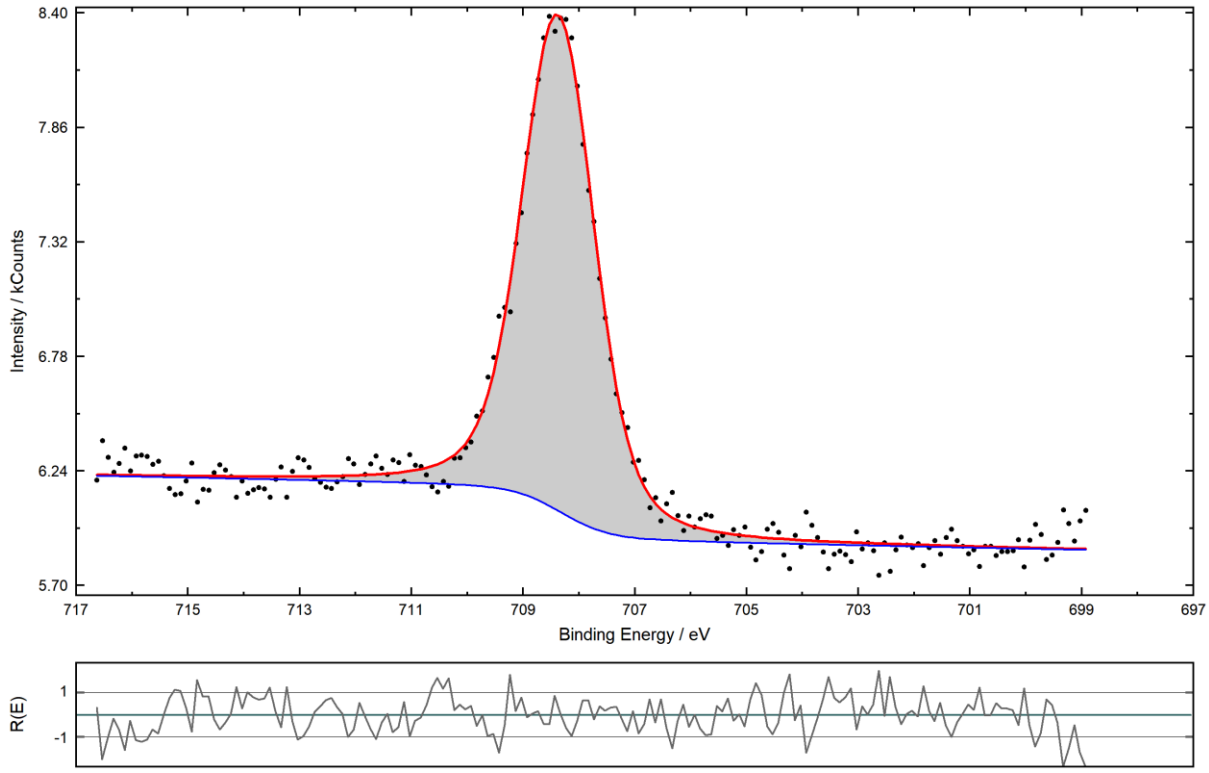

Figure 44 - MnFeA03 Fe $2p_{3/2}$ XPS detailed spectrum

A quantification table is provided (Table 12). Mn:Fe ratio is 1.23, which is very close to the AES provided value. Fe:N ratio is 1:5.95, a very satisfactory value. Na:Fe ratio is 1.5, which is lower than the one obtained with AES yet plausible. The overall results from this quantification match very well with the provided ones.

Table 12 – MnFeA03 XPS quantification table

Peak name	E_B /eV	Area/cps·eV	Sens. Fact.	Norm. Area	Quant./at.%	
C 1s_ 11 Peak 1	284.53	4040.378	16.78	240.7853	58.58	58.58
C 1s_ 11 Peak 2	285.59	0	16.792	0	0	
Mn 2p_ 13 Doublet 1	641.76	4961.307	258.39	19.20077	4.67	5.27
Mn 2p_ 13 Doublet 2	645.61	638.7283	258.47	2.471103	0.6	
N 1s_ 15 Peak 1	397.6	3247.921	31.08	104.502	25.42	25.42
Na 1s_ 16 Peak 1	1071.77	5143.345	193.71	26.55164	6.46	6.46
Fe 2p3_ 12 Peak 1	708.37	3609.701	205.69	17.5488	4.27	4.27

4.3.4 TiFe01

Survey spectrum for TiFe01 is displayed in Figure 45. Again, every expected element is present. Traces of chlorine were detected, yet this can be very probably an impurity from the synthesis mixture, which contained HCl (Section 3.1.2)

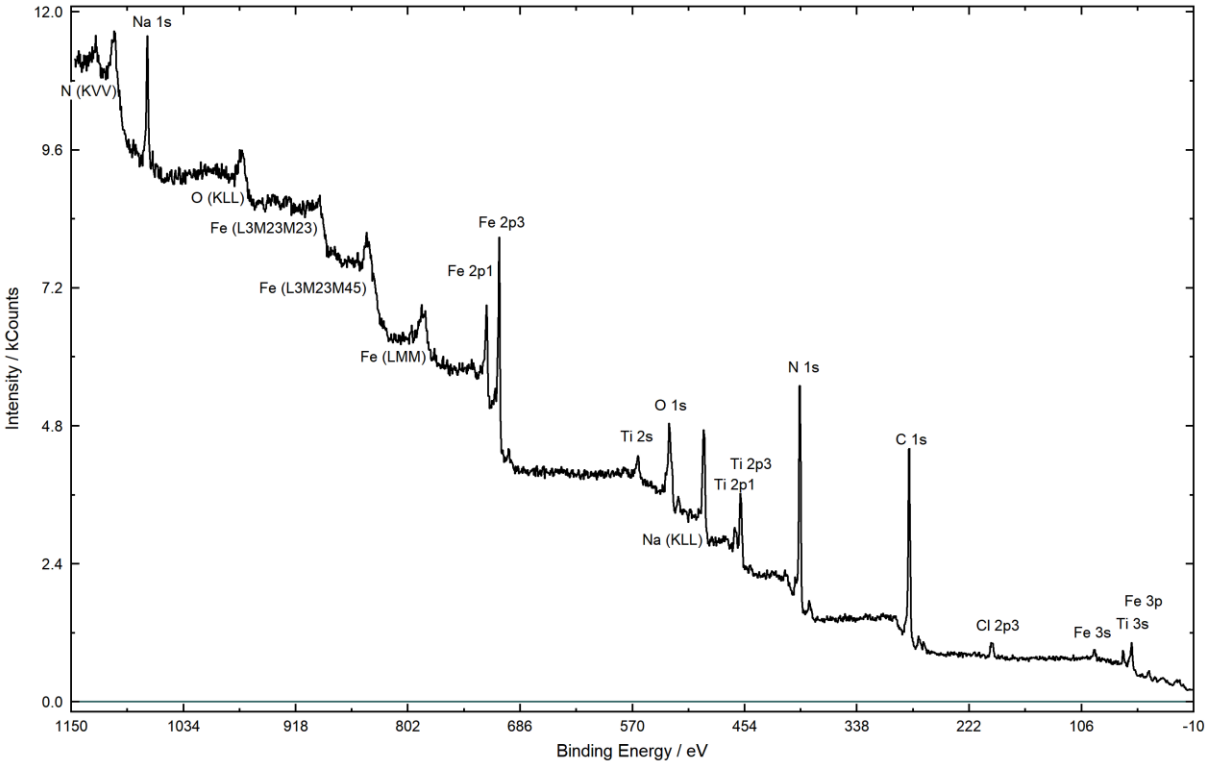

Figure 45 – TiFe01 XPS survey spectrum

Figure 46 displays the Ti 2p spectrum. The starting parameters of the fitting included two doublets, yet only a doublet could be deconvoluted. The E_B for Ti $2p_{3/2}$ was 458.8 eV. Values reported in literature were 458.8 eV [78], 458.9 eV [14] and 458.4 eV [79]. These first two values were both attributed to Ti^{IV}, yet the last one was not given an interpretation by authors.

Due to the striking similarity of the obtained value with the ones from literature, the oxidation state of Ti in this powder was assumed to be Ti^{IV}.

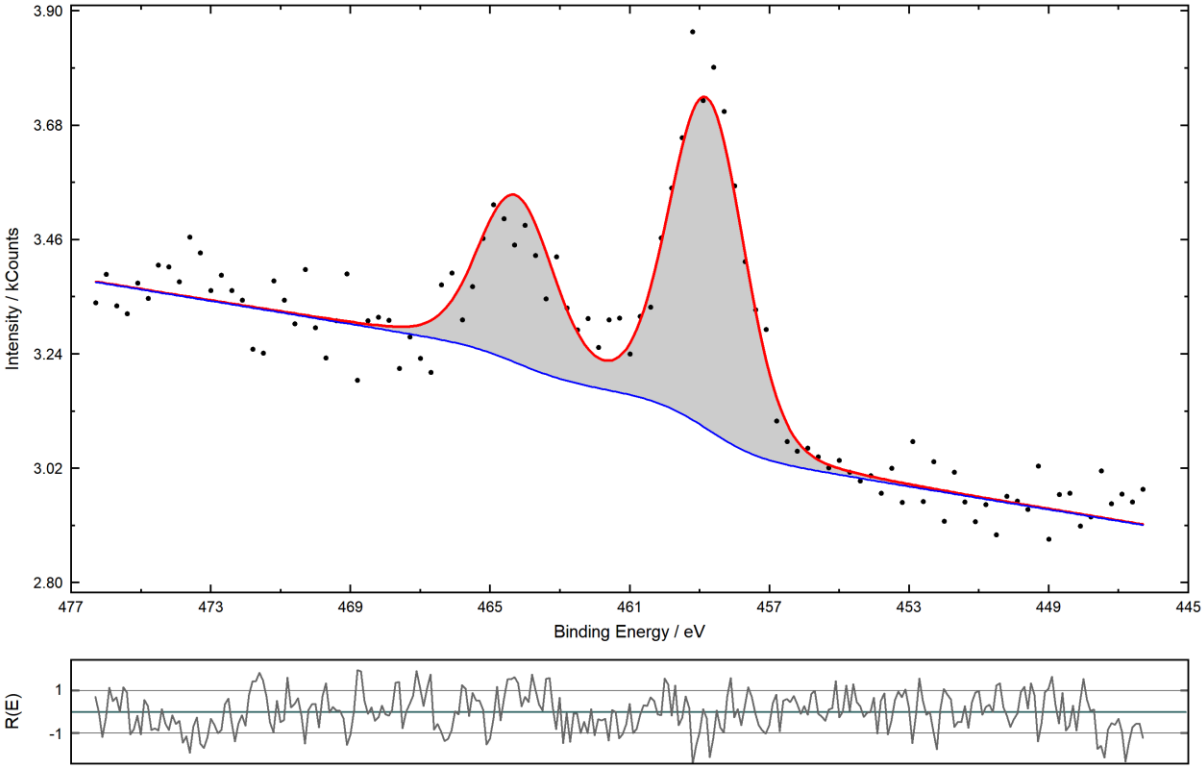

Figure 46 – TiFe01 Ti 2p XPS detailed spectrum

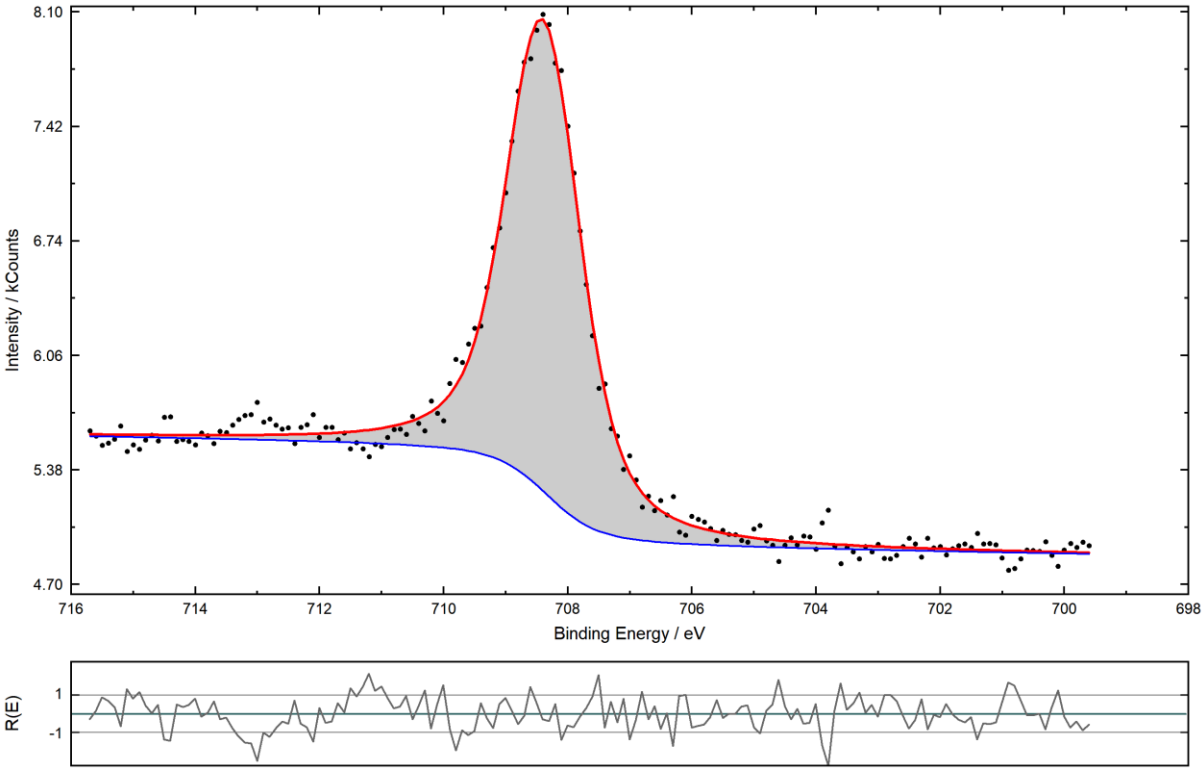

Figure 47 – TiFe01 Fe $2p_{3/2}$ XPS detailed spectrum

Fe $2p_{3/2}$ (Figure 47) was fitted with a single peak, located at 708.4 eV. This was attributed to Fe^{II}. Other binding energies for TiHCF from literature included 709.1 eV (Fe^{II}) and 710.7 eV (Fe^{III}) [78], 708.7 eV (Fe^{II}) [14] and 708.6 eV (Fe^{II}) and 713.3 eV (Fe^{III}) [79].

Surprisingly, the N 1s signal (Figure 48) presented two extra higher-binding energy peaks: the first at 399.1 eV and the second at 402.1 eV. Again, organic nitrogen falls in this range of binding energies and it is difficult to identify with certainty the corresponding species. Interesting enough, 399.2 eV is the chemical species reported for PhCN (Ph = Phenyl). In the next sections, extra peaks will be neither shown nor discussed even if they are present – they will be the subject of a specific section (Section 4.3.11).

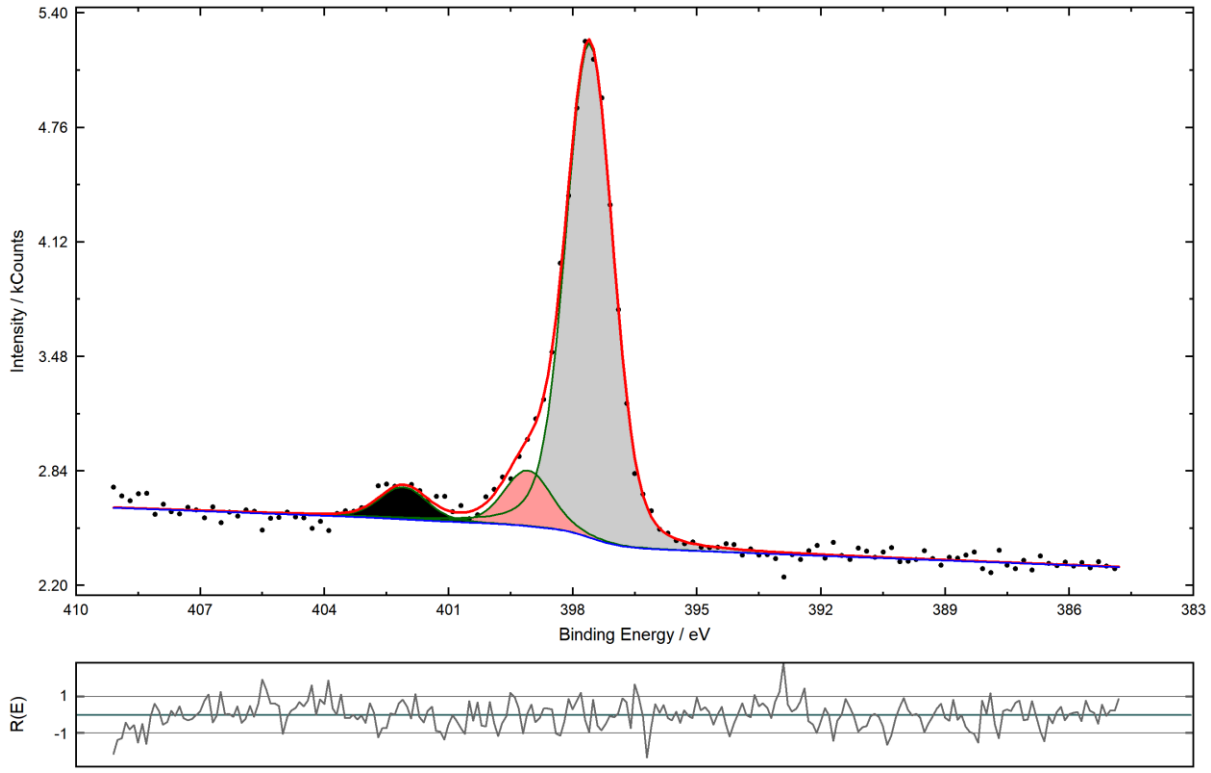

Figure 48 – TiFe01 N 1s XPS detailed spectrum

Figure 49 displays the C 1s signal, which has three extra peaks – located at 286.2 eV, 287.7 eV and 289.0 eV. Aside from amine functionalities, these chemical shifts often correspond to carbon bonded to oxygen [51], e.g.: ethers, carboxyls, carbonates. The main peak, attributed to cyanide, was found at 284.6 eV. Nevertheless, it must be noticed that the compound was obtained from an organic Ti salt as precursor – therefore, there could be additional organic matter that could be oxidized or contribute to the overall signal. As for the case of N 1s,

additional peaks in the C 1s will not be shown or discussed anymore – they will be in a separate section (Section 4.3.13).

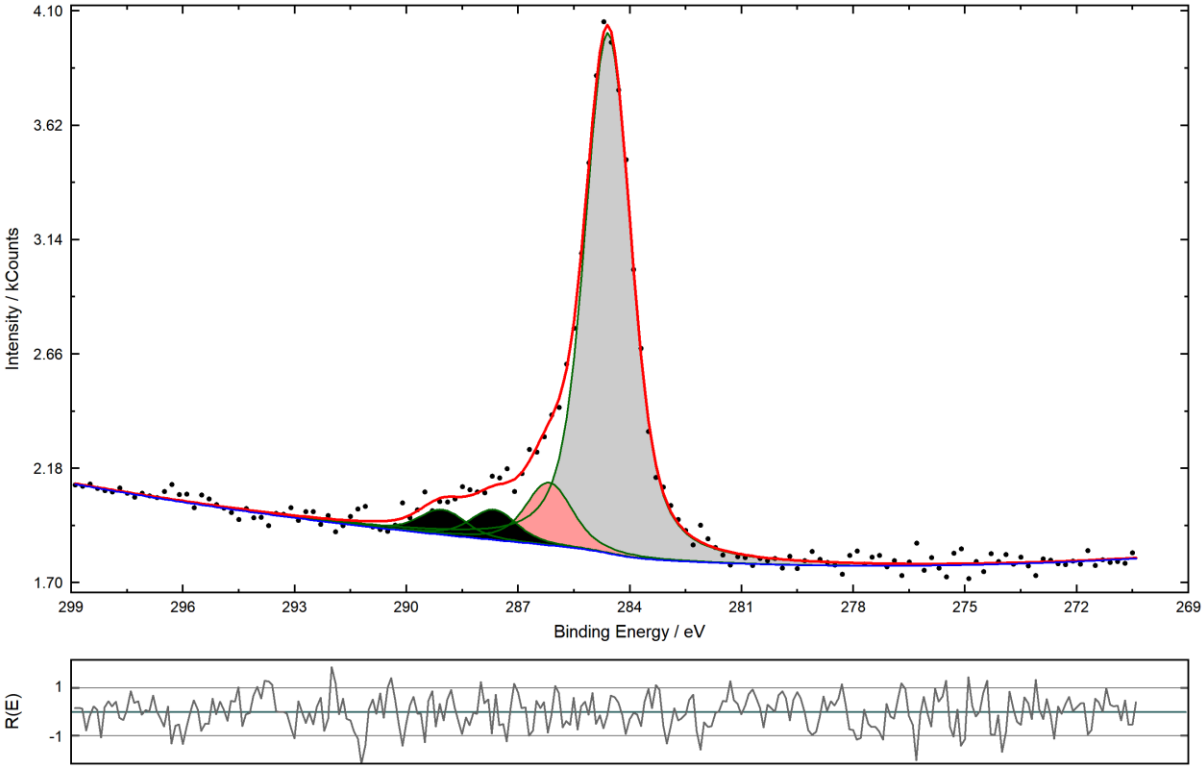

Figure 49 – TiFe01 C 1s XPS detailed spectrum

Table 13 provides quantification for the sample. Ti:Fe ratio is 0.78, again very close to the reported value. Na:Fe is 1.2, a higher but plausible value. The Fe:N ratio is 1:5.54 – acceptable and still quite representative of the theoretical stoichiometry. The results are well matching with the reported ones.

Table 13 - TiFe01 XPS quantification table

Peak name	E_B /eV	Area/cps·eV	Sens. Fact.	Norm. Area	Quant./at.%	
C 1s_ 11 Peak 1	284.59	3419.033	16.78	203.7565	45.4	55.7
C 1s_ 11 Peak 2	286.17	412.8587	16.804	24.56907	5.47	
C 1s_ 11 Peak 3	287.66	199.1801	16.816	11.84468	2.64	
C 1s_ 11 Peak 4	289.04	165.4765	16.819	9.838667	2.19	
N 1s_ 15 Peak 1	397.6	3593.253	31.08	115.613	25.76	30.35
N 1s_ 15 Peak 2	399.09	405.68	31.097	13.04563	2.91	
N 1s_ 15 Peak 3	402.1	235.1024	31.133	7.551548	1.68	
Na 1s_ 16 Peak 1	1072.02	4906.169	193.65	25.33433	5.65	5.65
Na 1s_ 16 Peak 2	1073.26	0	193.78	0	0	
Ti 2p_ 19 Doublet 1	458.8	2268.567	138.85	16.33767	3.64	3.64
Ti 2p_ 19 Doublet 2	457.49	0	138.86	0	0	
Fe 2p3_ 13 Peak 1	708.39	4293.43	205.69	20.8728	4.65	4.65

4.3.5 TiFe02

The survey spectrum for TiFe02 will not be shown since it is very similar to the one obtained for TiFe01. Figure 50 shows the Ti 2p spectrum. The Ti $2p_{3/2}$ E_B is located at 458.7 eV – being very close to the binding energy of Ti $2p_{3/2}$ in TiFe01, Ti is supposed to be Ti^{IV} even in this case.

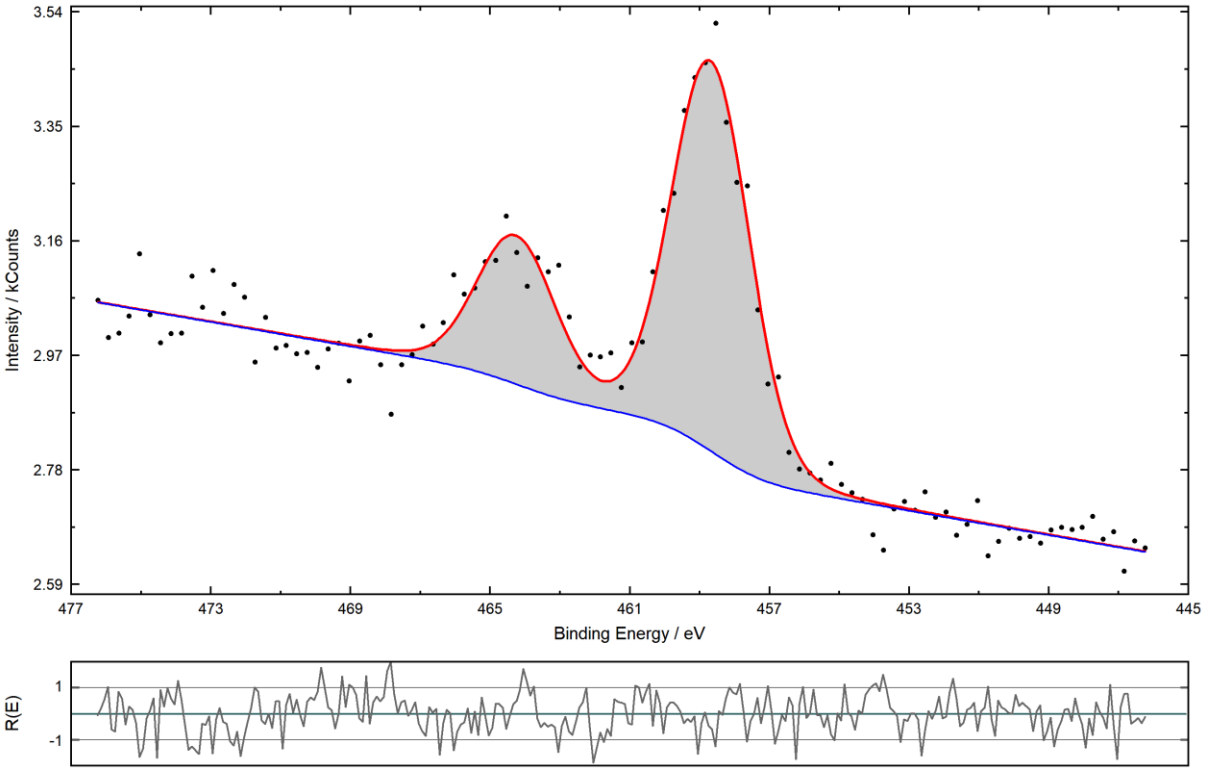

Figure 50 – TiFe02 Ti 2p XPS detailed spectrum

Fe $2p_{3/2}$ (Figure 51) peak was found at 708.5 eV. Again, it is attributed to Fe^{II}.

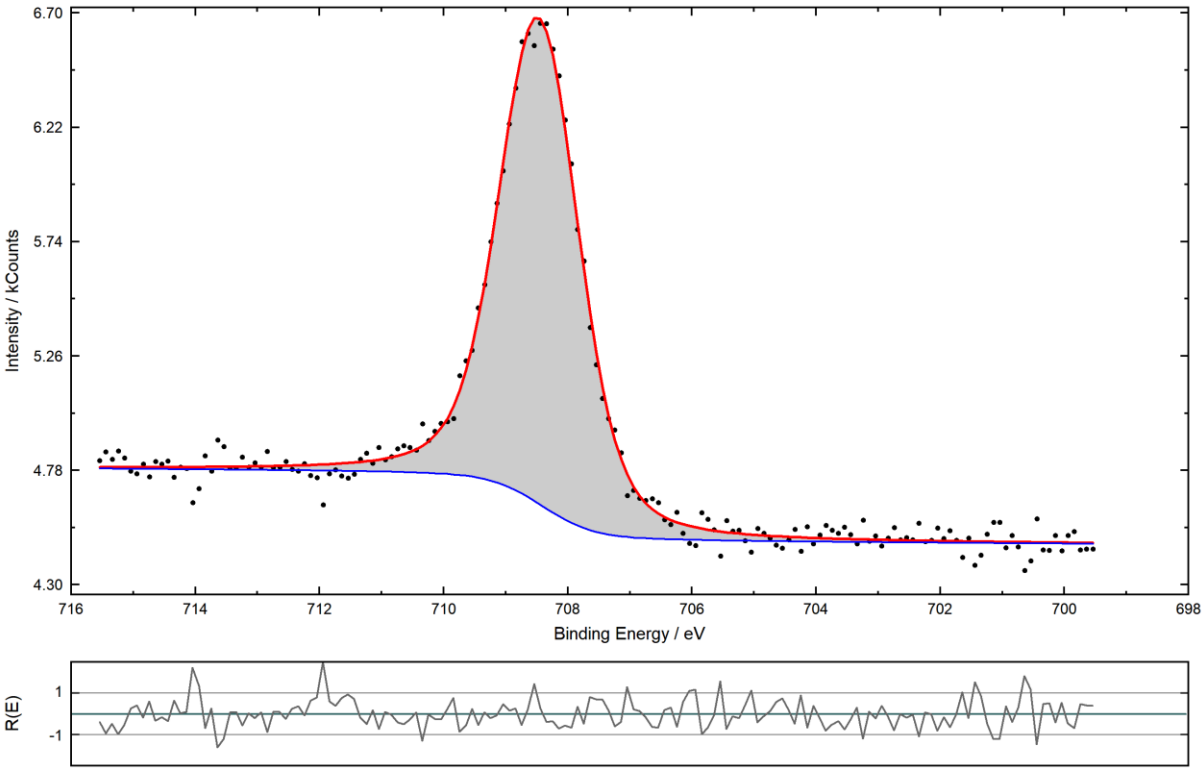

Figure 51 – TiFe02 Fe $2p_{3/2}$ XPS detailed spectrum

Quantification results are shown in Table 14. No reported AES stoichiometry is provided for TiFe02, therefore the following values cannot be compared to other experimental results. Ti:Fe ratio is 1.02, which is plausible. The amount of Ti seems to be higher than in TiFe01's case. The Na:Fe ratio is 0.9 and this result is acceptable. Fe:N is 1:5.56, practically the same amount as in the other TiFe powder. These results are likely to be representative of the material.

Table 14 – TiFe02 XPS quantification table

Peak name	E_B /eV	Area/cps·eV	Sens. Fact.	Norm. Area	Quant./at.%	
C 1s_ 11 Peak 1	284.66	3109.741	16.78	185.3243	50.14	62.81
C 1s_ 11 Peak 2	286.33	498.48	16.804	29.66437	8.03	
C 1s_ 11 Peak 3	288.34	288.0663	16.807	17.13966	4.64	
N 1s_ 15 Peak 1	397.6	2606.256	31.08	83.85638	22.69	25.3
N 1s_ 15 Peak 2	399.07	300.2365	31.097	9.654837	2.61	
Na 1s_ 16 Peak 1	1071.98	2599.832	193.65	13.42493	3.63	3.63
Ti 2p_ 19 Doublet 1	458.69	2147.383	138.85	15.46493	4.18	4.18
Fe 2p3_ 13 Peak 1	708.46	3103.978	205.69	15.0902	4.08	4.08

4.3.6 CuFeA

The survey spectrum for CuFeA is shown in Figure 52. Every expected element is detected, as well as a sulphur impurity (S 2p peak). This may be a residue of sulphates, for one of the used precursor was $CuSO_4$.

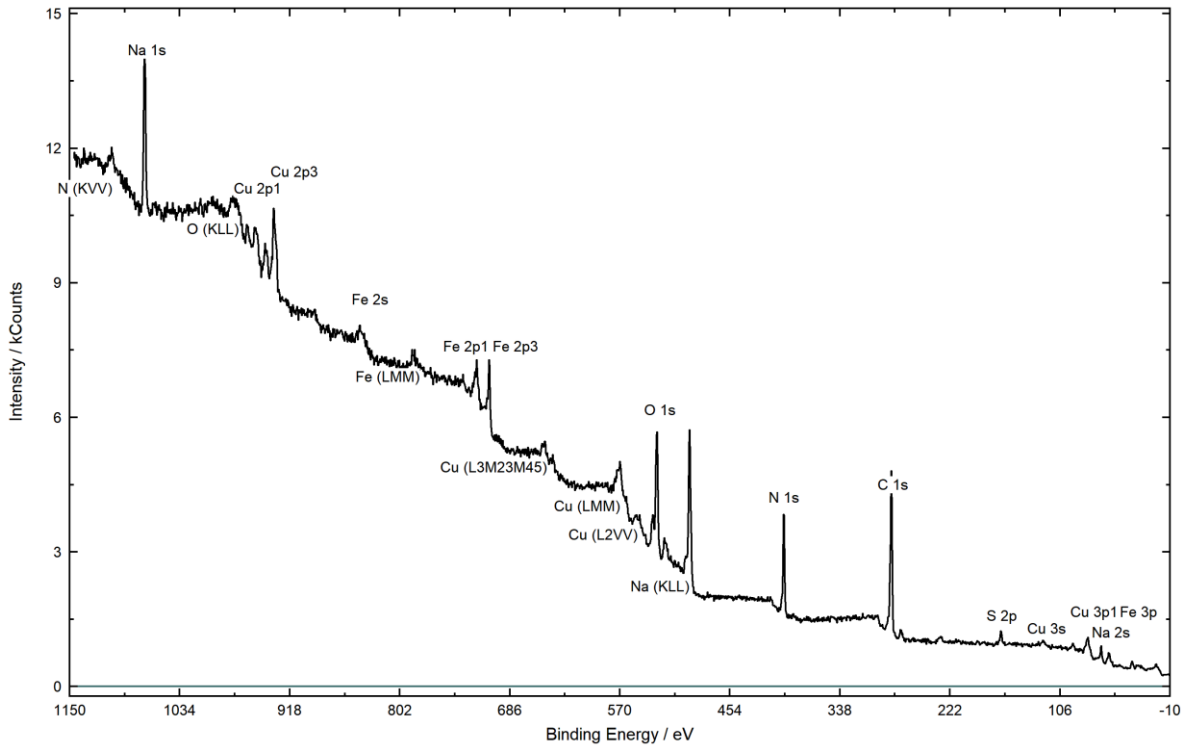

Figure 52 - CuFeA XPS survey spectrum

Figure 53 shows Cu $2p_{3/2}$ spectrum. The interpretation of the spectrum did not present difficulties: the peak at 935.0 eV belongs to Cu^{II} and the one at 932.5 eV to Cu^{I}. Cu^{II} has a well-known shake-up satellite [80], which appears here at 943.4 eV. This satellite will be taken into account for the quantification calculations. Cu^{I} is most probably produced by reduction happening while exposed to UHV [81]. Since Cu^{I} and Cu^{II} peaks have a similar intensity, it could be argued that Cu^{I} is not only a reduction product, but also a species present right from the start. A calibration curve could be helpful in determining possible initial quantities, yet this was not done in this work. Ma et. al [82], who synthesized CuHCF nanoflakes, reported 937.2 eV as E_B for Cu^{II} and 946.2 eV for Cu^{II} satellite. Other experimental binding energy values from literature include 933.0 eV (Cu^{I}) and 935.7 eV (Cu^{II}) [83]. The obtained values are very low in comparison to the cited ones.

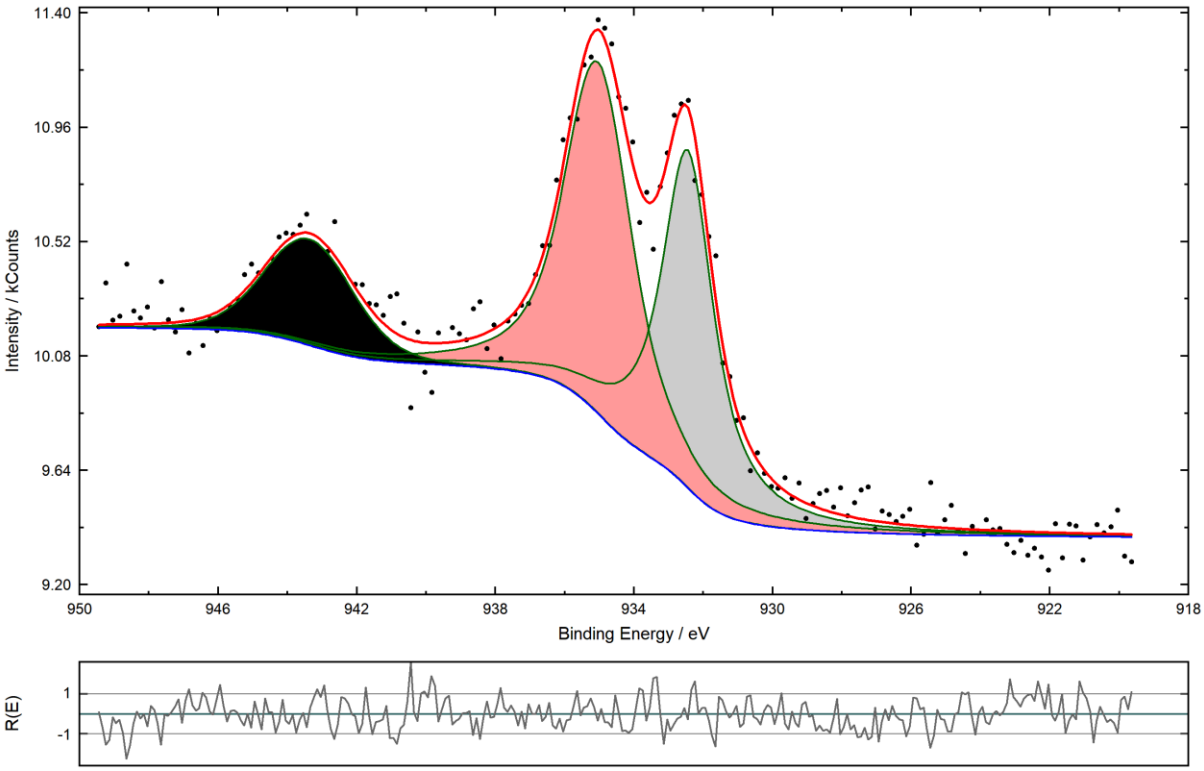

Figure 53 – CuFeA Cu $2p_{3/2}$ XPS detailed spectrum

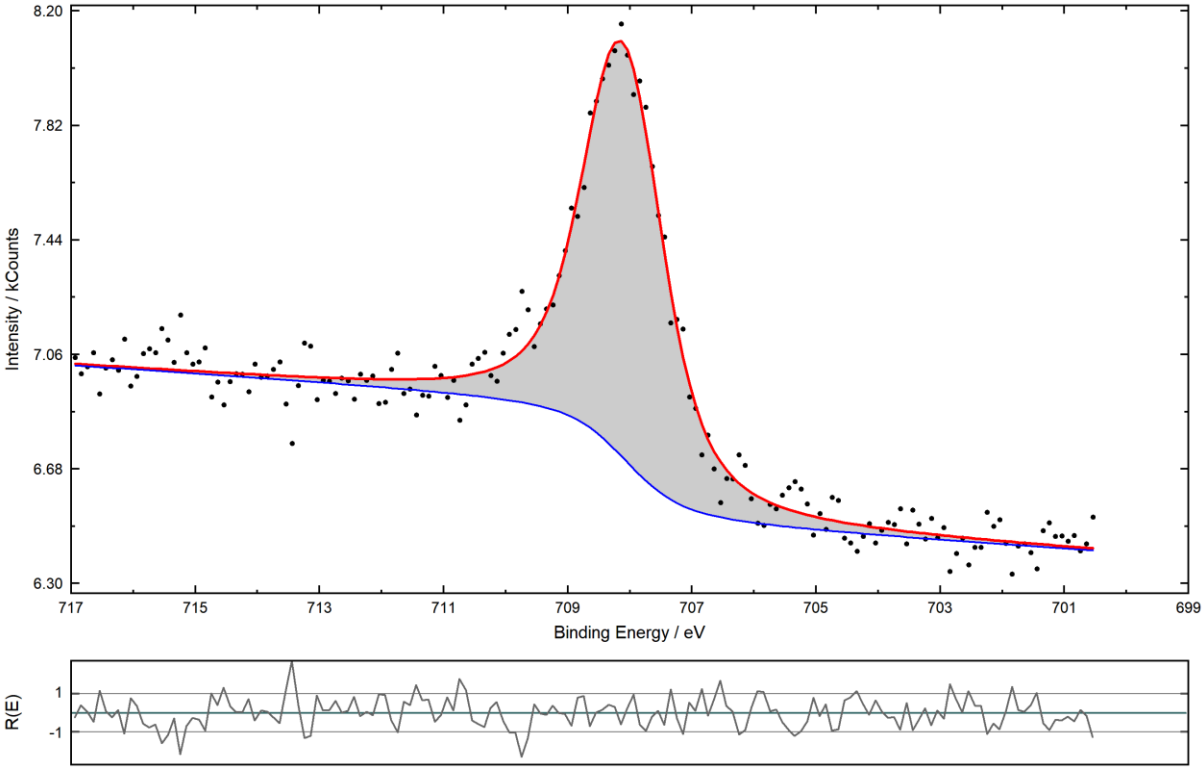

Figure 54 – CuFeA Fe $2p_{3/2}$ XPS detailed spectrum

Fe $2p_{3/2}$ signal (Figure 54) for CuFeA was found at 708.1 eV. Such value and the sharpness of the peak, as in previous powders, suggested the only presence of Fe^{II}. Literature values for Fe in CuHCF are 708.9 eV (Fe^{II}) [82], 708.6 eV (Fe^{II}) and 710.1 eV (Fe^{III}) [83] and 708.0 eV (Fe^{II}) and 709.6 eV (Fe^{III}) [84]. The E_B for Fe $2p_{3/2}$ is definitely lower than some provided by the references, but also lower than the other values obtained for Fe^{II} in the other powders. Since the binding energy values for both Cu and Fe are lower than they should supposedly be, charge correction to 397.6 eV might be responsible – the value may not be the correct one for this compound in particular and the ≡N-Cu bond might actually have a higher E_B.

A quantification table (Table 15) is provided below. The shake-up satellite related to Cu^{II} is used only qualitatively in some papers and in such cases, its contribution in quantitative analysis is therefore ignored [80]. Cu:Fe ratio is 1.9 considering the intensity coming from the shake-up satellite – higher than 1.7, which is the reported value. Without it, the Cu:Fe ratio is 1.6. Both are acceptable, but it is not possible to state which one is more correct. Na:Fe is 2.67 – too high in comparison to 1.4. The amount of Na^+ in the powder is overestimated. N:Fe is 7.18, definitely higher. Fe might be actually underestimated.

Table 15 - CuFeA XPS quantification table

Peak name	E_B /eV	Area/cps·eV	Sens. Fact.	Norm. Area	Quant./at.%	
C 1s Peak 1	284.4	3358.919	16.788	200.0786	54.04	60.98
C 1s Peak 2	286.06	244.083	16.792	14.53567	3.93	
C 1s Peak 3	288.19	187.6073	16.807	11.16245	3.01	
N 1s Peak 1	397.61	2528.596	31.08	81.35767	21.97	21.97
Na 1s Peak 1	1071.49	5855.598	193.55	30.25289	8.17	8.17
Fe 2p3 Peak 1	708.11	2328.487	205.53	11.32885	3.06	3.06
Cu 2p3 Peak 1	932.45	2864.45	350.16	8.180264	2.21	5.82
Cu 2p3 Peak 2	935.04	3524.274	350.64	10.05078	2.71	
Cu 2p3 Peak 3	943.37	1169.198	352.08	3.320801	0.9	

4.3.7 CuFeB

The survey spectrum for CuFeB will not be shown – as in the case of the TiFe samples, the spectrum is identical to the one for CuFeA.

Figure 55 shows the Cu $2p_{3/2}$ spectrum. The given interpretation is analogous to the one given for CuFeA. The resulting binding energies are 932.5 eV (Cu^I), 935.1 eV (Cu^{II}) and 943.3 eV (Cu^{II} satellite).

Fe $2p_{3/2}$ (Figure 56) was fitted with a singlet and the resulting E_B was 708.1 eV. Iron oxidation state is assigned to be Fe^{II}.

Even with CuFeB, the binding energy values are lower than expected.

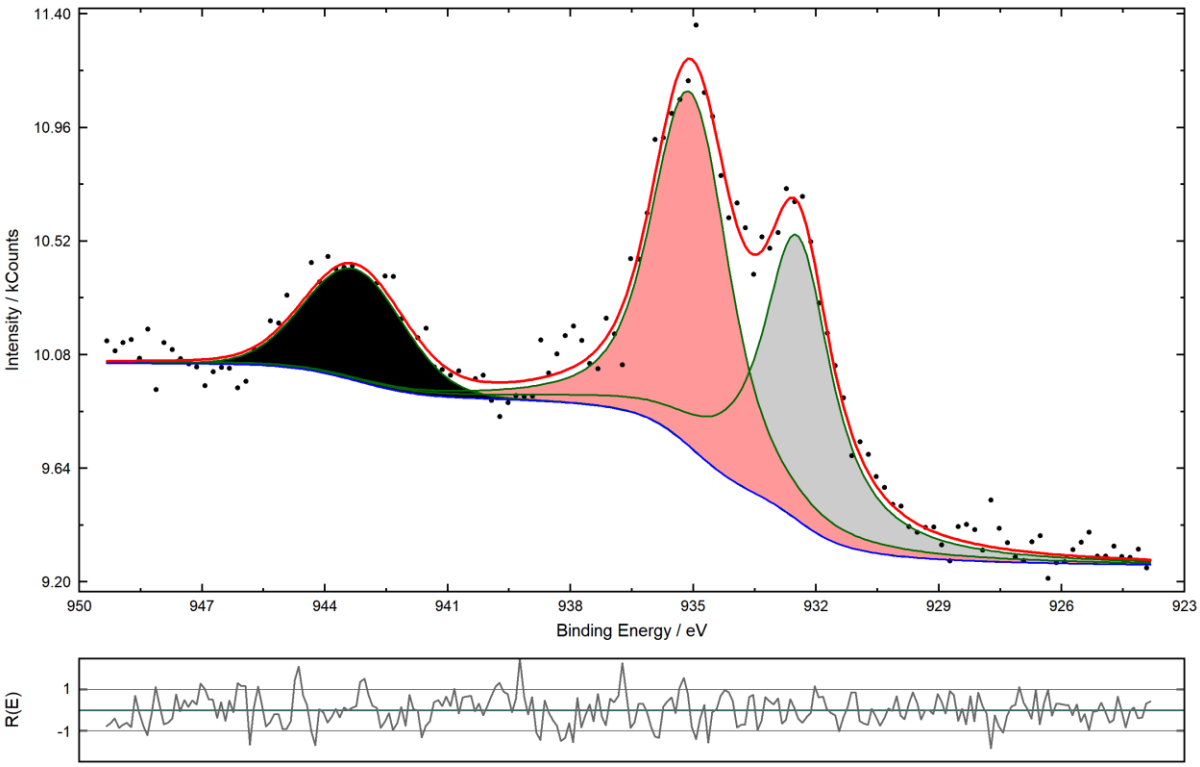

Figure 55 – CuFeB Cu $2p_{3/2}$ XPS detailed spectrum

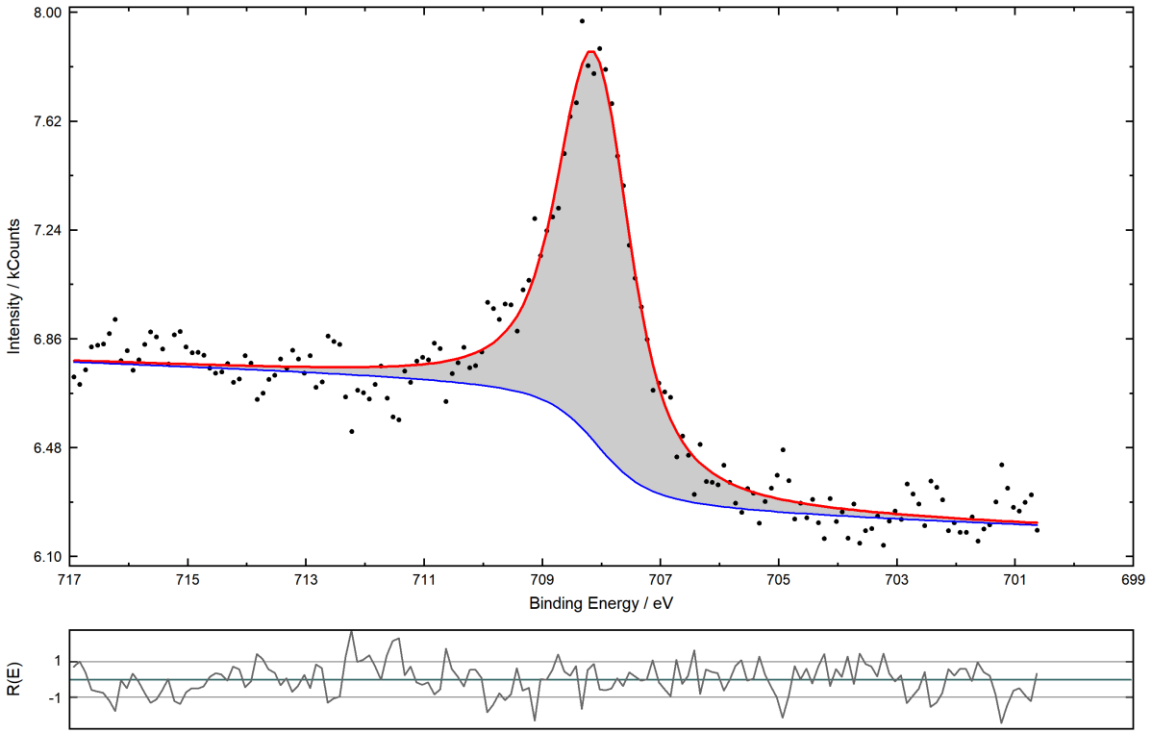

Figure 56 – CuFeB Fe $2p_{3/2}$ XPS detailed spectrum

Quantification for the sample is shown in Table 16. Cu:Fe is 1.85 with the inclusion of the satellite peak and 1.56 without it. The former value is larger than that reported in Section 3.1.2, whereas the latter confirms it. The amount of Na is exactly double than the content of Fe – totally overestimated. This also happens to N:Fe ratio, which turns out to be 7.93. This quantification is relatively similar to CuFeA: ratios do not turn out sensibly and Fe may be underestimated. A possible reason might be an unsuitable sensitivity factor.

Table 16 - CuFeB XPS quantification table

Peak name	E_B /eV	Area/cps·eV	Sens. Fact.	Norm. Area	Quant./at.%	
C 1s Peak 1	284.39	3719.182	16.788	221.5381	61.02	61.02
N 1s Peak 1	397.61	2731.284	31.08	87.87916	24.21	24.21
Na 1s Peak 1	1071.65	4291.064	193.71	22.15189	6.1	6.1
Cu 2p3 Peak 1	932.46	2730.492	350.16	7.797708	2.15	5.63
Cu 2p3 Peak 2	935.07	3319.276	350.64	9.466146	2.61	
Cu 2p3 Peak 3	943.29	1110.424	352.08	3.15387	0.87	
Fe 2p3 Peak 1	708.12	2272.687	205.53	11.05737	3.05	3.05

4.3.8 CuFeC

The survey spectrum for CuFeC will not be shown, since it is very similar to CuFeA's. The main difference consists in the lack of Na signals, as the alkali metal ion present is K^+ this time – yet its amount is indeed very small (Figure 57). Even though the signal is a doublet, it was fitted as a singlet in the same detailed spectrum as C 1s signal.

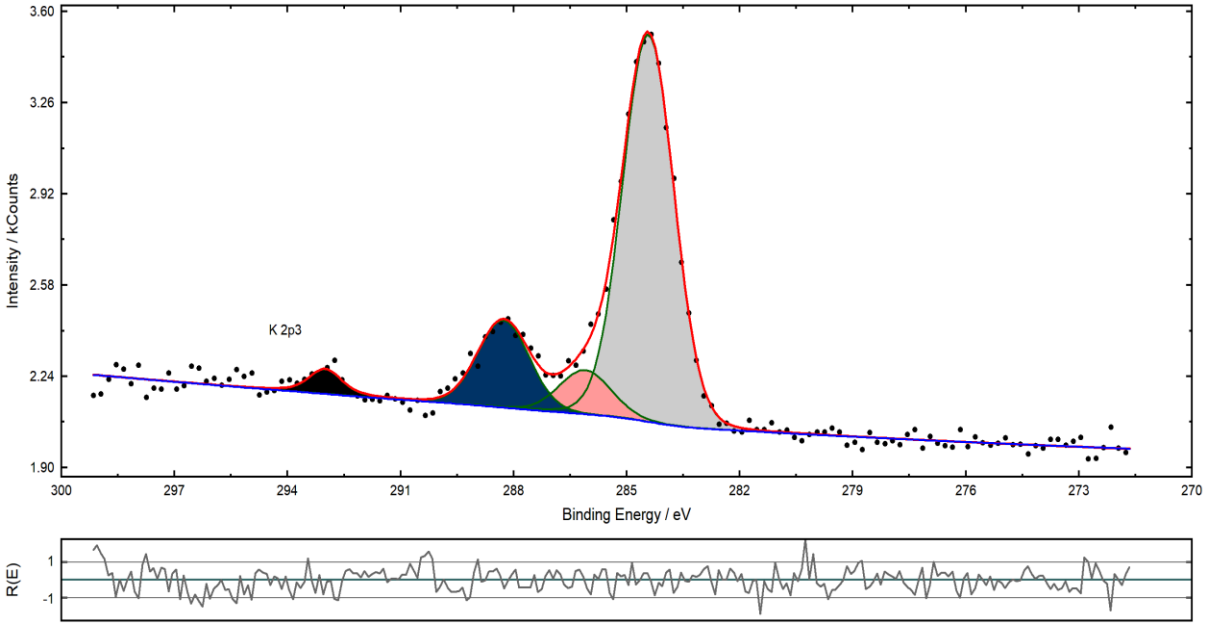

Figure 57 – CuFeC K 2p and C 1s XPS detailed spectrum

The spectrum for Cu $2p_{3/2}$ is displayed in Figure 58. The obtained E_B values are 932.8 eV (Cu^I), 935.1 eV (Cu^{II}) and 943.3 eV (Cu^{II} satellite).

The Fe $2p_{3/2}$ signal (Figure 59) is found at 708.1 eV. Also in this case, oxidation state is assumed to be Fe^{II}.

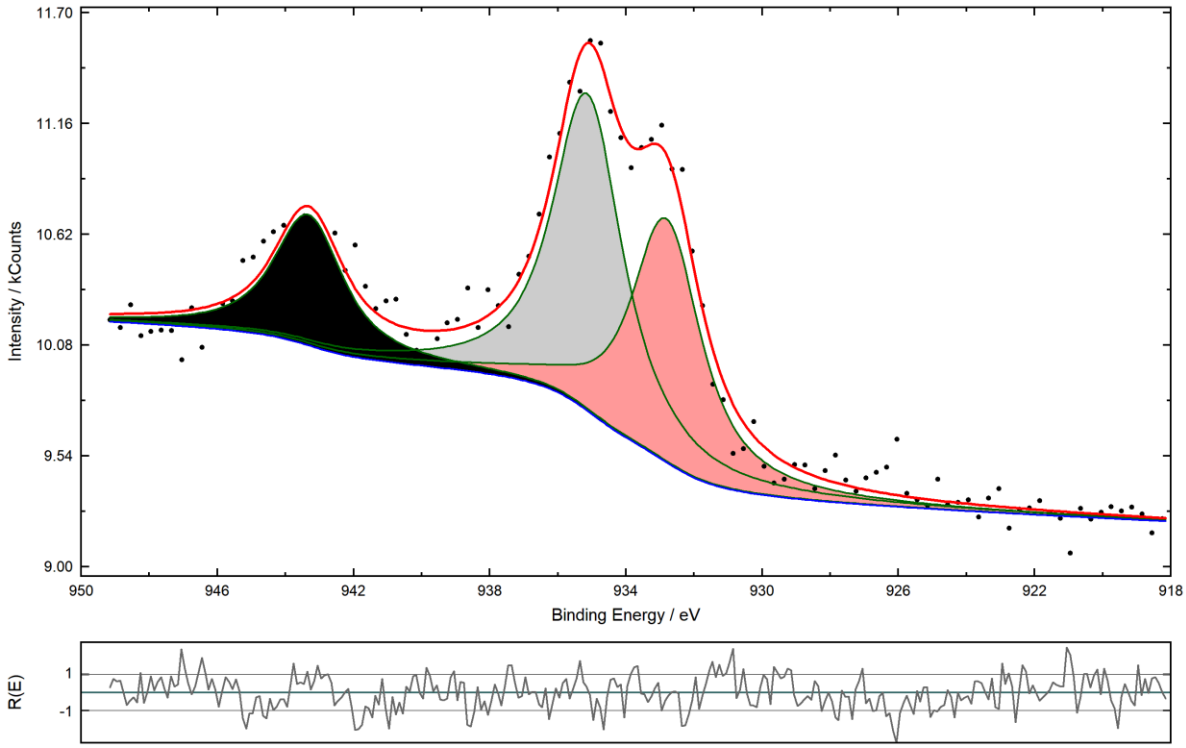

Figure 58 – CuFeC Cu $2p_{3/2}$ XPS detailed spectrum

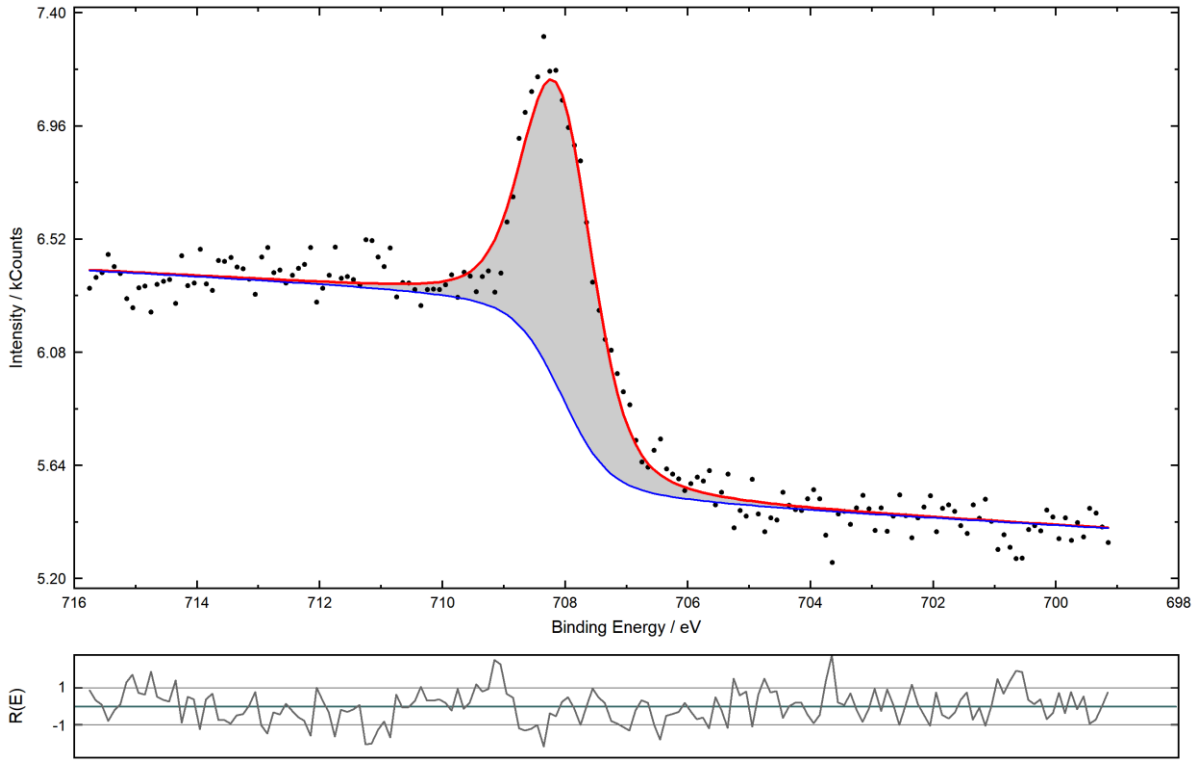

Figure 59 – CuFeC Fe $2p_{3/2}$ XPS detailed spectrum

A quantification table for CuFeC is shown (Table 17). Cu:Fe is 3.57 with consideration of the satellite peak and 2.89 without it: in both cases, the values are definitely overestimated and

not reliable. K:Fe is 0.19, very close to 0.15 – the amount of K in the sample is nevertheless little. N:Fe ratio is 9.16, which is too high. This quantification is unreliable, even to a higher degree than for the other two CuFe samples.

Table 17 - CuFeC XPS quantification table

Peak name	E_B /eV	Area/cps·eV	Sens. Fact.	Norm. Area	Quant./at.%	
C 1s_ 11 K 2p3	284.42	2110.43	16.788	125.7106	39.83	53.85
C 1s_ 11 Peak 2	286.1	242.0771	16.792	14.41622	4.57	
C 1s_ 11 Peak 3	291.08	0	16.815	0	0	
C 1s_ 11 Peak 4	288.27	475.0042	16.807	28.26228	8.96	
K 2p	293	102.2897	66.769	1.531994	0.49	
N 1s_ 15	397.6	2271.861	31.08	73.09721	23.16	34.12
N 1s_ 15	399.73	623.4888	28.471	21.89908	6.94	
N 1s_ 15	402.22	361.1325	28.478	12.6811	4.02	
Cu 2p3_ 12 Peak 1	935.16	4658.423	350.83	13.27803	4.21	9.51
Cu 2p3_ 12 Peak 2	932.83	3534.688	350.24	10.09219	3.2	
Cu 2p3_ 12 Peak 3	943.85	1464.667	352.14	4.159271	1.32	
Cu 2p3_ 12 Peak 4	942.08	870.7088	351.95	2.473907	0.78	
Fe 2p3_ 13 Peak 1	708.1	1640.373	205.53	7.980953	2.53	2.53

4.3.9 InFe02

The survey spectrum for InFe02 is displayed in Figure 60. Every expected element is present. Oxygen was also detected: probably as water or from adventitious carbon.

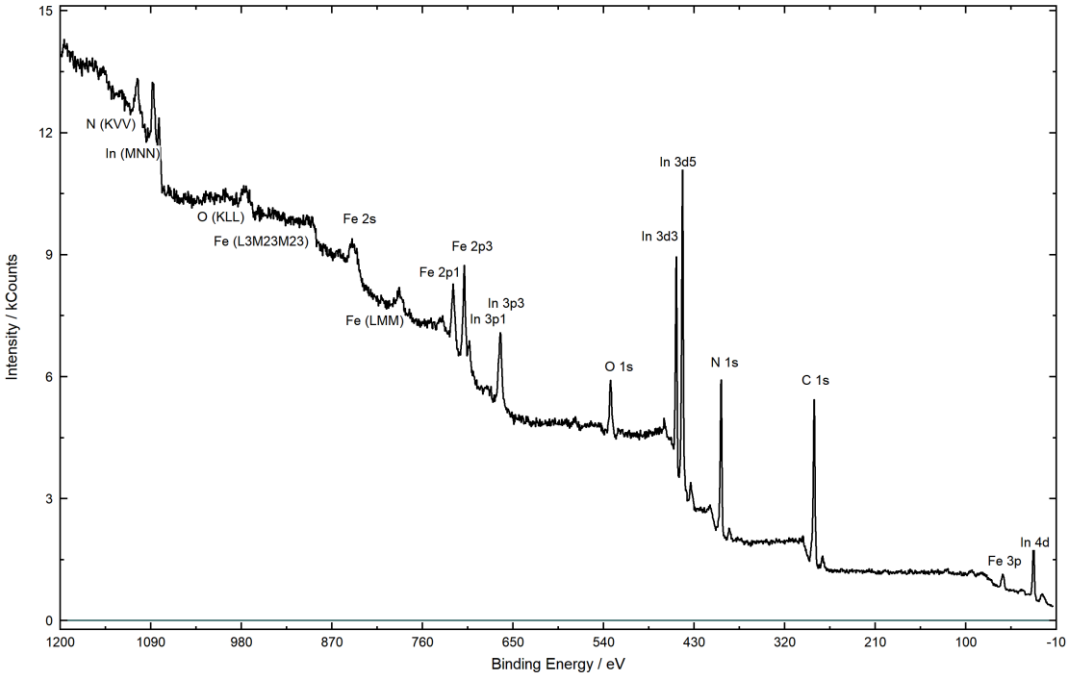

Figure 60 – InFe02 XPS survey spectrum

In 3d spectrum (Figure 61) was fitted with a single doublet. In $3d_{5/2}$ was found at 444.5 eV. Cataldi et al. [10] found 445.5 eV as E_B value. A 1.0 eV discrepancy must be taken into consideration, as the obtained result is very low in comparison. It might be that charge correction was not performed on the right value, and therefore, the ≡N-In bond has a higher binding energy – as in the case of CuFeA/B/C. Indium was previously found to be not electroactive and present only as In^{III} in InHCF [7], [10]. The metal is consequently supposed to be In^{III}.

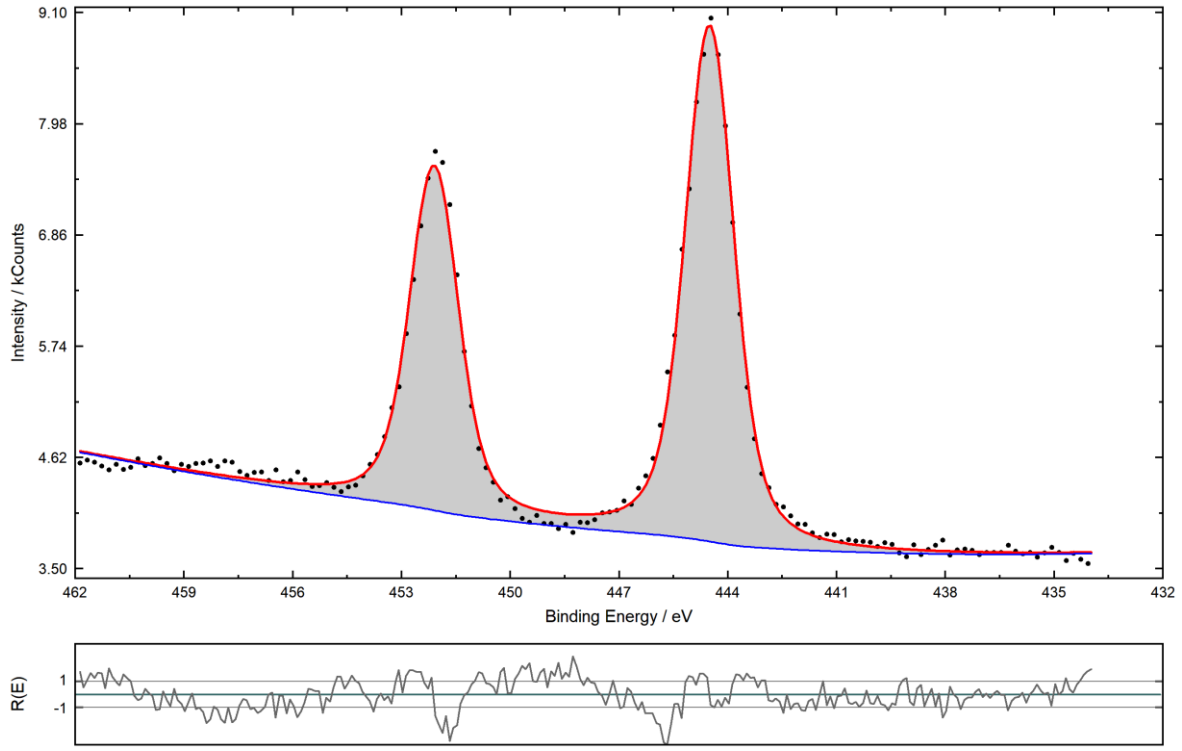

Figure 61 - InFe02 In 3d XPS detailed spectrum

Fe $2p_{3/2}$ (Figure 62) consisted of two peaks: the main one at 709.6 eV (Fe^{III}) and a second one at 708.0 eV (Fe^{II}). Fe^{II} is most likely produced by reduction of Fe^{III} due to UHV or X-ray irradiation. The black peak is In $3p_{1/2}$ peak, which is found at around 703 eV.

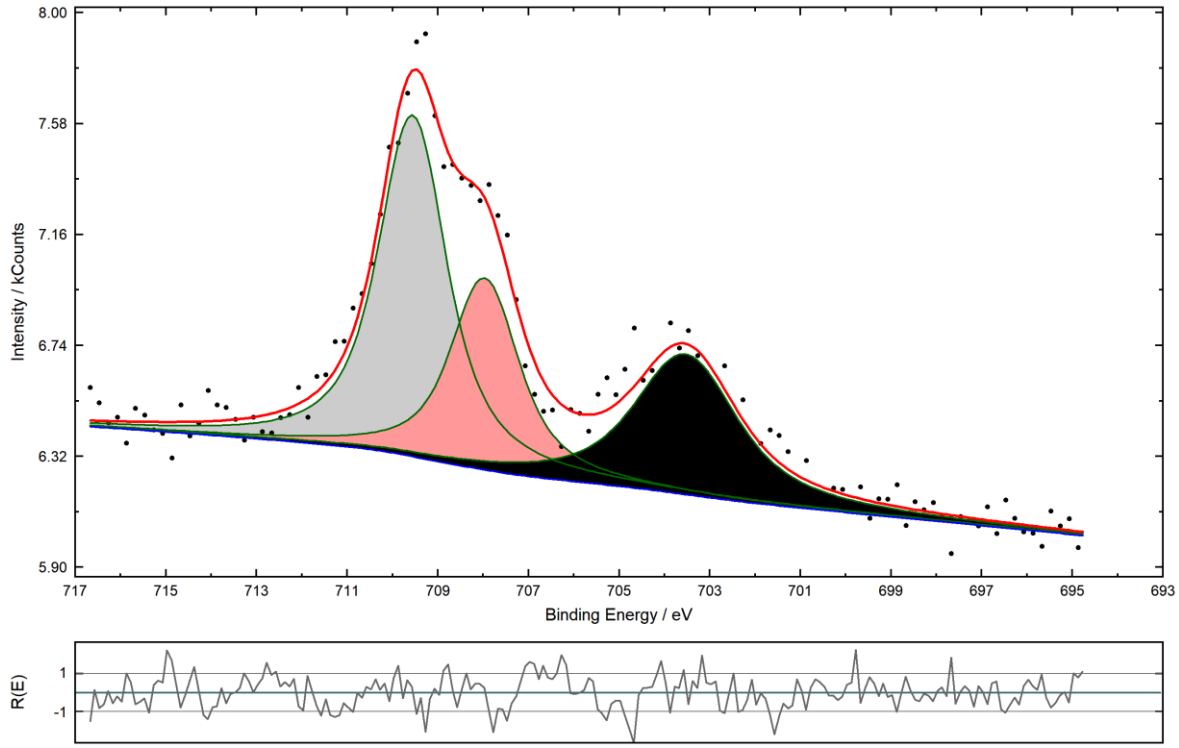

Figure 62 - InFe02 Fe $2p_{3/2}$ XPS detailed spectrum

A quantification table is provided (Table 18). No stoichiometry was determined for the powder. Cataldi et al. [10] found that the formula for the compound seemed to be $In_4[Fe(CN)_6]_3$ (insoluble Prussian Blue type). The In:Fe ratio is 1.74 – this result is acceptable and it is consistent with the idea that the synthesized powder is more similar to insoluble PB, i.e. with the presence of $Fe(CN)_6$ ion vacancies. The N:Fe ratio is 5.97, which is an excellent value. C 1s signal could be fitted with two peaks: the ratio of C1s Peak 1 in respect to N 1s is 1.25, an acceptable value. It is possible that C 1s Peak 1 (284.2 eV) is the cyanide signal, while C 1s Peak 2 (284.9 eV) is adventitious carbon. Usually, it is not possible to deconvolute two peaks less than 1.0 eV apart, yet the software was able to do so in this specific case. It was decided to take this into consideration and try quantitative analysis, even if – being the signals very close – there could be considerable relative errors. C 1s signal is displayed in Figure 63.

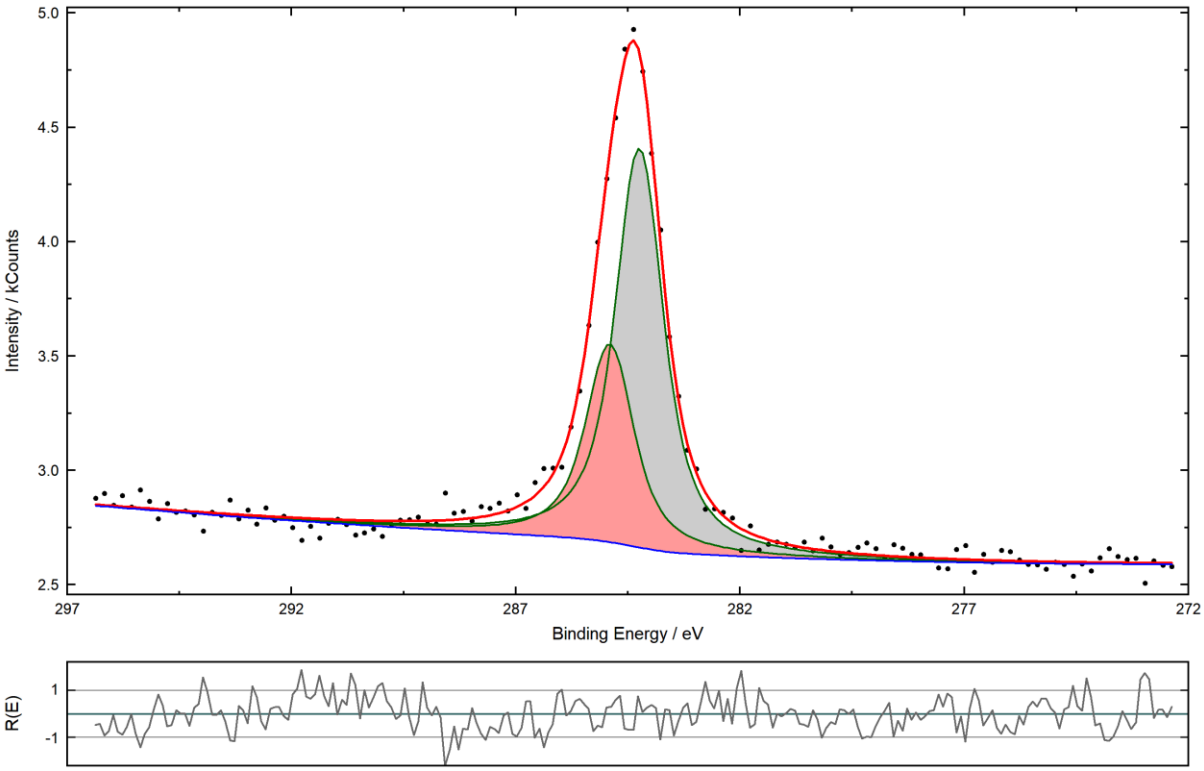

Figure 63 – InFe02 C 1s XPS detailed spectrum

Table 18 - InFe02 XPS quantification table

Peak name	E_B /eV	Area/cps·eV	Sens. Fact.	Norm. Area	Quant./at.%	
C 1s Peak 1	284.24	2621.113	16.788	156.1302	36.92	55.23
C 1s Peak 2	284.91	1300.844	16.8	77.43122	18.31	
In 3d Doublet 1	444.51	14302.16	394.07	36.29271	8.58	8.58
N 1s Peak 1	397.61	3864.654	31.08	124.3454	29.4	29.4
Fe 2p3 Peak 1	709.56	2738.397	205.73	13.31051	3.15	6.8
Fe 2p3 Peak 2	707.97	1539.525	205.67	7.485194	1.77	
In 3p	703.54	1670.535	210.46	7.93743	1.88	

4.3.10 CoNP_05

The survey spectrum for the sample is shown in Figure 64 . Every expected element is present and no impurities were detected.

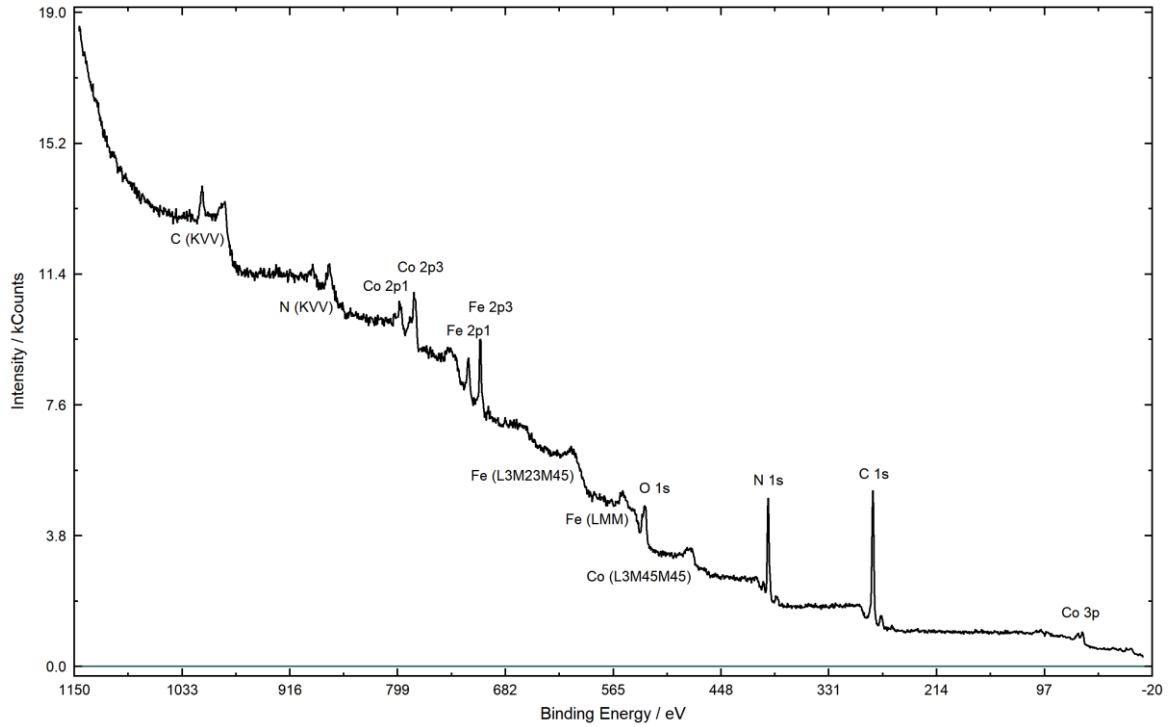

Figure 64 - CoNP_05 XPS survey spectrum

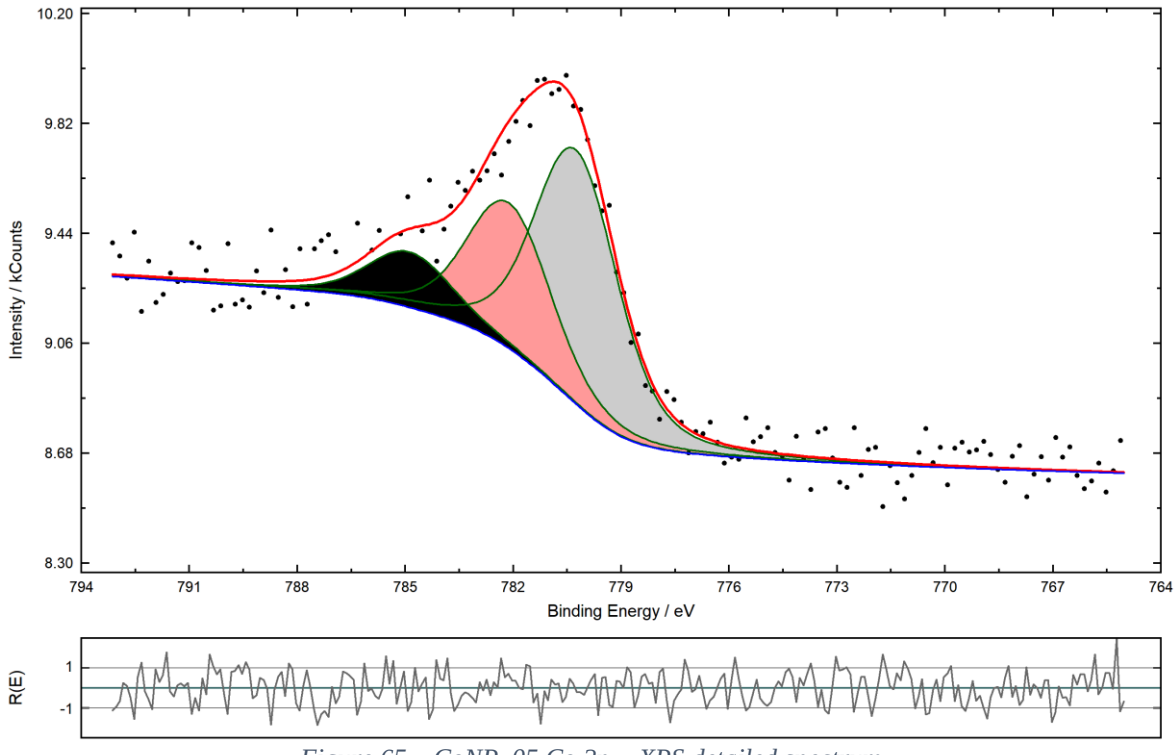

Figure 65 – CoNP_05 Co $2p_{3/2}$ XPS detailed spectrum

The Co $2p_{3/2}$ spectrum (Figure 65) was fitted with three singlets, located at 780.3 eV, 782.1 eV and 784.9 eV. The peaks were all assigned to Co^{II} – which is a d^7 cation in a high-spin environment and therefore likely to present multiplet structures features. The black peak at

784.9 eV might be a satellite. Cano et al. [30] fitted the signal with four peaks: three singlets between 780.4 eV and 784.2 eV and one broad satellite at 787.4 eV. All these signals were related to Co^{II} only.

Fe $2p_{3/2}$ signal (Figure 66) was also fitted with three singlets. The main peak, whose E_B was found at 709.8 eV, was attributed to Fe^{II} in CoNP. The interpretation of the other two peaks, respectively at 708.5 eV and at 706.8 eV, is more puzzling. The peak at 706.8 eV might be $Fe^{0,}$ since the E_B falls in the range for metallic iron. As stated in Section 4.3.1.3, metal nitroprussides undergo degradation by X-Ray irradiation. Fe^0 is believed to be produced by $CN^{\bullet}$ radicals, which are formed during decomposition of the product. Decomposition generating $CN^{\bullet}$ radicals happens both during heating of the sample – which has probably been done for all the analyzed samples – and during X-Ray irradiation [30]. Cano et al. [30] found three peaks for the Fe $2p_{3/2}$ signal as well: 710.3 eV (Fe^{II} in CoNP), 708.5 eV (high-spin Fe^{II}-$(NC)_x$) and 707.3 eV (Fe^0). The identical E_B found for the second peak might lead to the conclusion that the corresponding is high-spin Fe^{II} indeed.

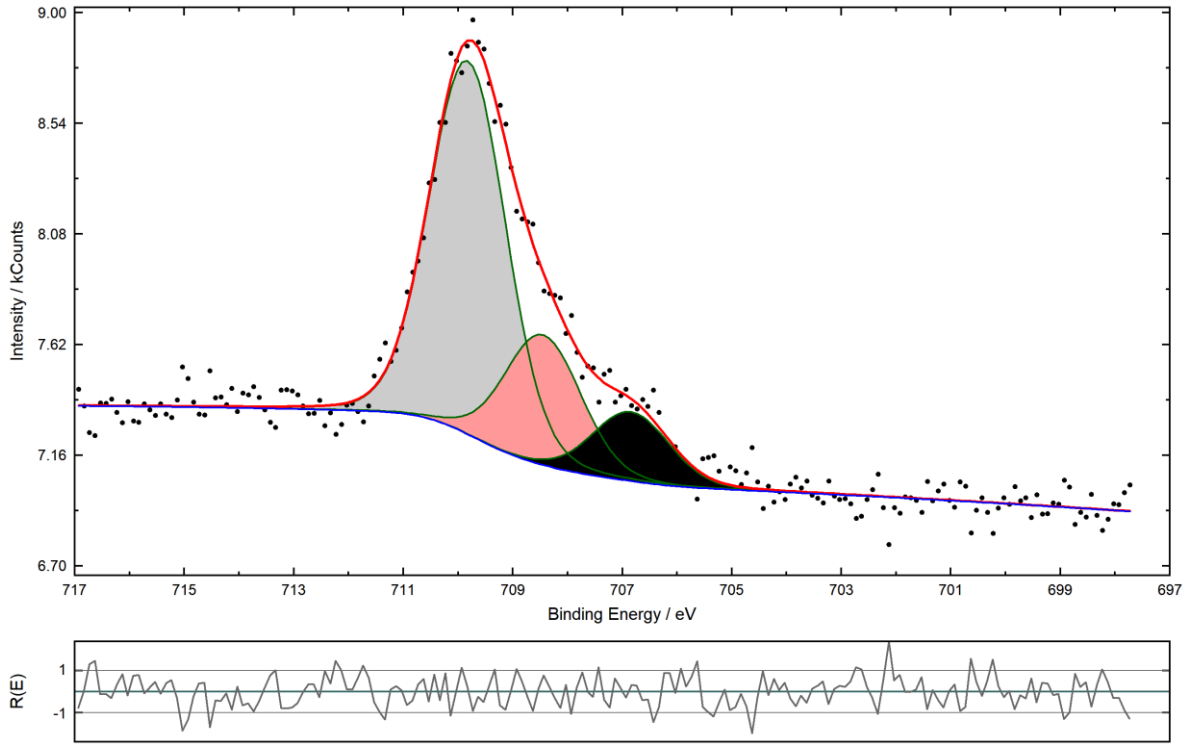

Figure 66 – CoNP_05 Fe $2p_{3/2}$ XPS detailed spectrum

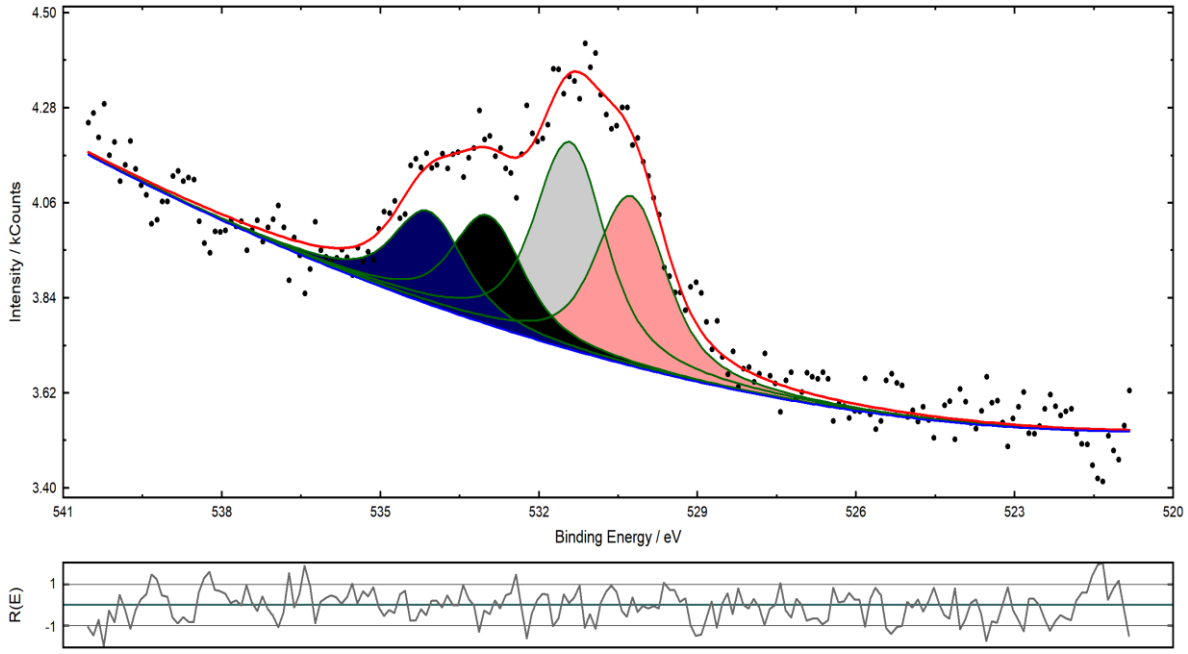

Figure 67 – CoNP_05 O 1s XPS detailed spectrum

The O 1s signal (Figure 67) was very different from that discussed in Section 4.3.1.3. This spectrum was recorded with Al-Kα (a Fe Auger line would overlap with the signal with Mg-Kα). Four singlets were deconvoluted, respectively at: 530.2 eV (which may be either CoO, Fe_3O_4 or a similar metal oxide), 531.4 eV (which may be C=O type oxygen), 532.9 eV (water) and 534.1 eV (ester-type oxygen, coming from dirt). No clear signal relatable to nitrosyl could be detected.

A quantification table (Table 19) is provided below. The Co:Fe ratio is 1:1 – this is a very good result, which matches the compound's reported stoichiometry. The N:Fe ratio is overestimated (6.86 instead of 6, taking all nitrogen into account). It is possible to notice that cyanide is overestimated, while nitrosyl is underestimated. The C:N ratio is also largely overestimated (2.48 instead of theoretical 1). The results are overall puzzling and only the M:Fe ratio seems to be fitting.

Table 19 – CoNP_05 XPS quantification table

Peak name	E_B /eV	Area/cps·eV	Sens. Fact.	Norm. Area	Quant./at.%	
C 1s Peak 1	283.67	4515.995	17.854	252.9402	58.29	58.29
N 1s -CN	397.2	3353.866	32.721	102.4989	23.62	25.64
N 1s -NO	402.11	287.5329	32.791	8.768652	2.02	
O 1s Peak 1	531.39	759.4159	55.302	13.73216	3.16	8.54
O 1s Peak 2	530.18	555.1267	55.303	10.03791	2.31	
O 1s Peak 3	532.93	408.7158	55.341	7.385406	1.7	
O 1s Peak 4	534.11	328.3562	55.38	5.929148	1.37	
Fe 2p3 Peak 1	709.82	2346.595	221.77	10.58097	2.44	3.74
Fe 2p3 Peak 2	708.45	817.7187	221.69	3.688485	0.85	
Fe 2p3 Peak 3	706.84	434.8493	221.37	1.964311	0.45	
Co 2p3 Peak 1	780.25	2445.301	267.20	9.151268	2.11	3.78
Co 2p3 Peak 2	782.12	1402.864	267.52	5.243783	1.21	
Co 2p3 Peak 3	784.88	534.1474	267.80	1.994568	0.46	

4.3.11 NiNP1

A survey spectrum is provided in Figure 68. Every expected element is present and no impurities are detected.

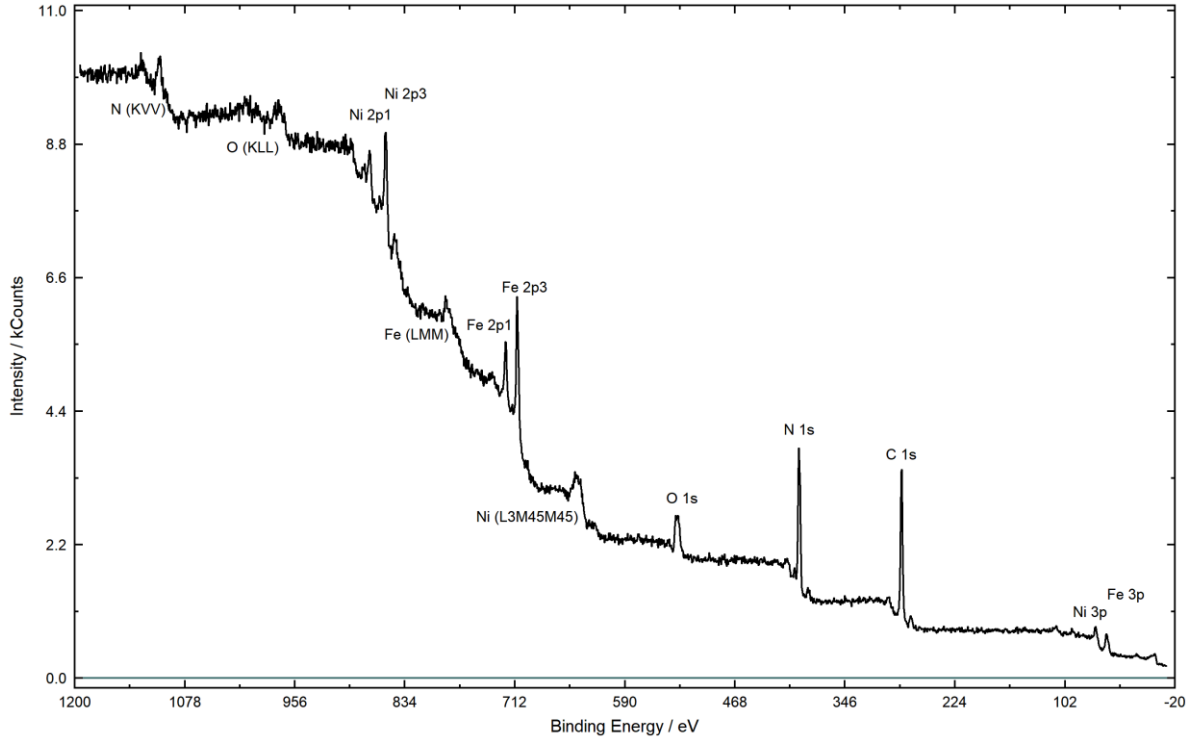

Figure 68 - NiNP1 XPS survey spectrum

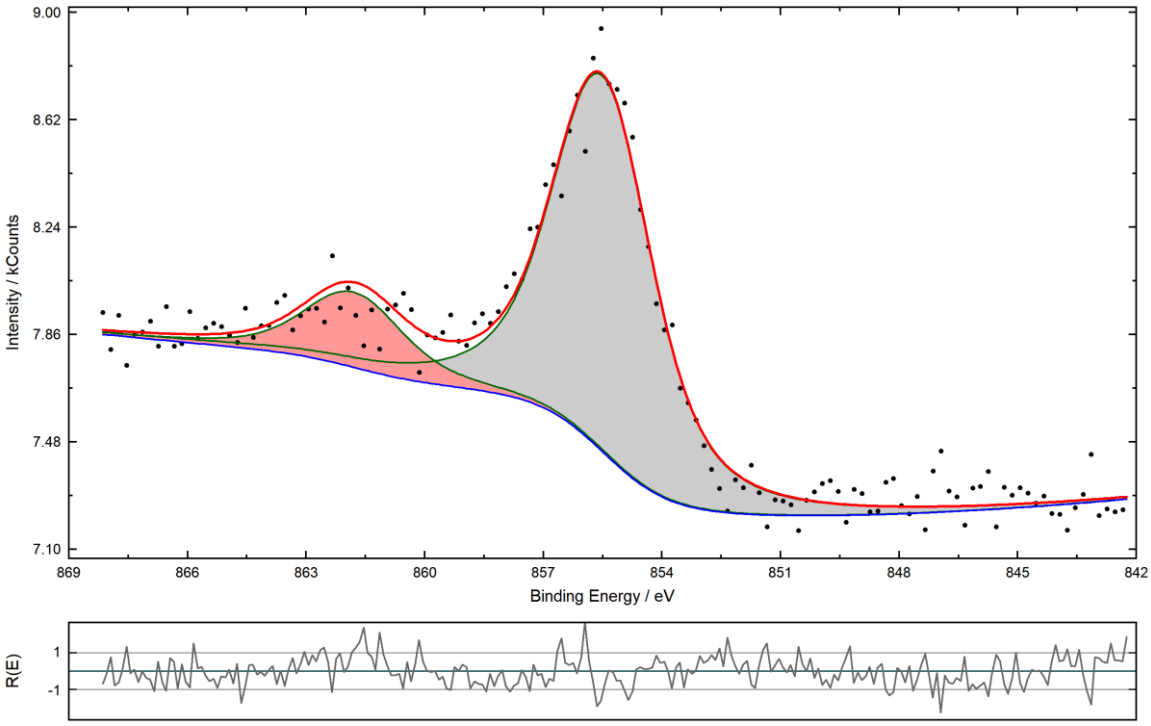

Figure 69 – NiNP1 Ni $2p_{3/2}$ XPS detailed spectrum

Ni $2p_{3/2}$ spectrum (Figure 69) was fitted with two singlets: a main peak attributed to Ni^{II} (855.5 eV) and its satellite (861.8 eV). Cano et. Al [30] assigned three peaks from 855.0 to 858.0 to Ni^{II} in NiNP and reported a broad Ni^{II} satellite at 862.8 eV.

Fe $2p_{3/2}$ (Figure 70) consists of two singlets: the main peak at 709.7 eV (attributed to Fe^{II} in NiNP) and the minor peak at 707.6 eV. The latter peak is most likely to be related to high-spin Fe^{II}-$(NC)_x$, since its E_B value is already too high for metallic Fe.

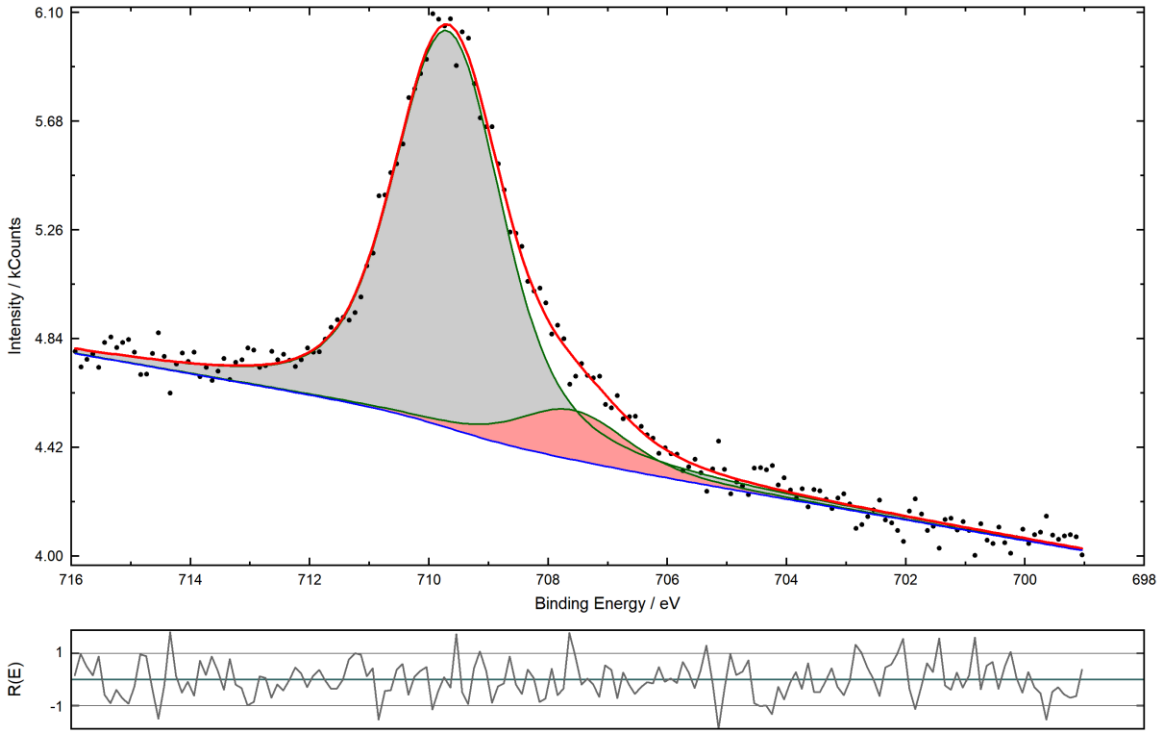

Figure 70 – NiNP1 Fe $2p_{3/2}$ XPS detailed spectrum

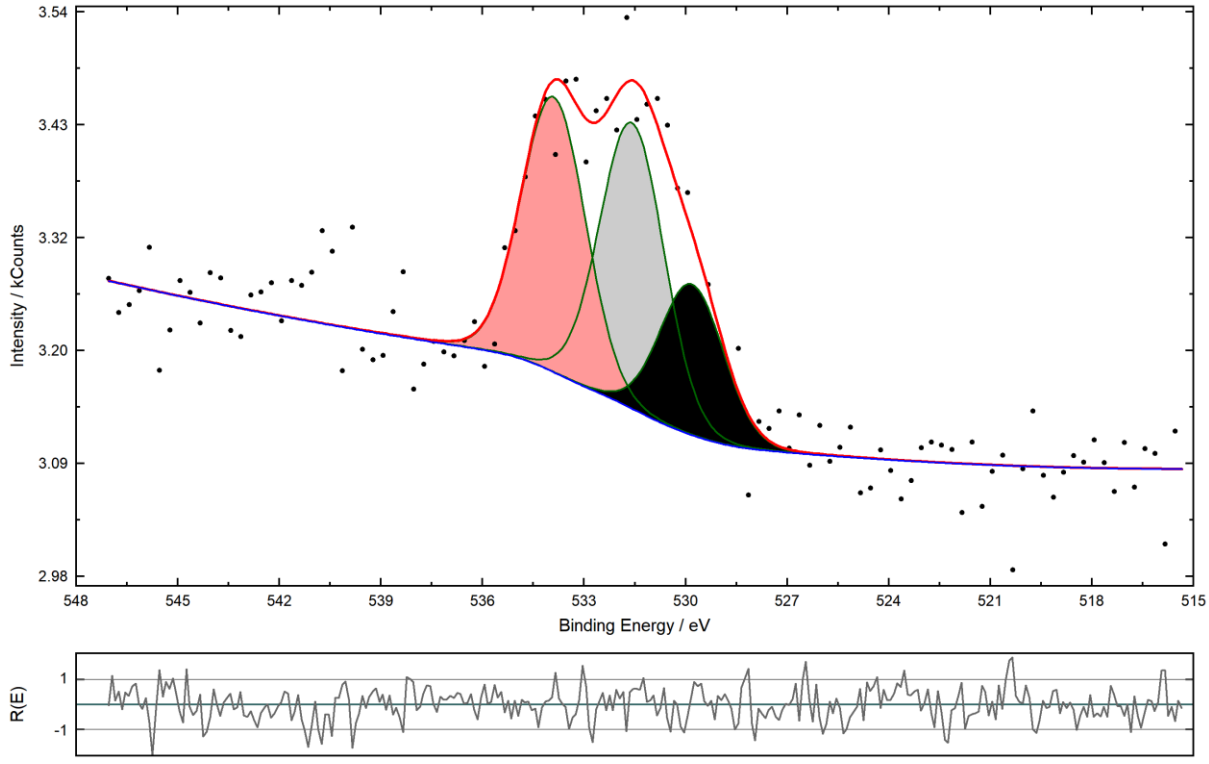

Figure 71 – NiNP1 O 1s XPS detailed spectrum

The O 1s signal (Figure 71) consisted of three peaks this time: the first at 529.8 eV (a metal oxide), and the others at 531.6 eV and 533.9 eV. These two peaks may be related to different

oxygens from dirt in the sample: the former to C=O type oxygen, the latter to ester type oxygen. Water is missing this time. Again, no distinct and clear peak could be deconvoluted for nitrosyl.

Quantification for the sample is reported below (Table 20). The Ni:Fe ratio is 0.92, which is a very good result. The overall Fe:N ratio is acceptable (1:6.17), yet nitrosyl is again underestimated while cyanide is overestimated.

Table 20 – NiNP1 XPS quantification table

Peak name	E_B /eV	Area/cps·eV	Sens. Fact.	Norm. Area	Quant./at.%	
C 1s_ 11 Peak 1	283.77	3195.504	16.788	190.3445	51.2	51.2
N 1s_ 13 Peak 1	397.21	3351.711	31.096	107.7859	28.99	31.67
N 1s_ 13 Peak 2	402.5	310.5878	31.116	9.981611	2.68	
O 1s_ 16 Peak 1	531.59	570.7199	52.558	10.85886	2.92	7.27
O 1s_ 16 Peak 2	533.9	549.1144	52.566	10.44619	2.81	
O 1s_ 16 Peak 3	529.81	300.1344	52.519	5.714777	1.54	
Ni 2p3_ 14 Peak 1	855.5	4321.531	294.70	14.66397	3.94	4.73
Ni 2p3_ 14 Peak 2	861.8	865.2955	295.45	2.928718	0.79	
Fe 2p3_ 12 Peak 1	709.69	3487.064	205.73	16.94955	4.56	5.13
Fe 2p3_ 12 Peak 2	707.58	435.7798	205.51	2.120407	0.57	

4.3.12 Overview: N 1s signal

A summary table for E_B values and the number of extra peaks is provided in Table 21. As explained, all samples showed a main peak which was attributed to cyanide and on which charge correction was performed (to 397.6 eV). Therefore, only extra peaks - from lower to higher binding energies – are summarized in the table.

Table 21 - N 1s signal: extra peaks

Sample	Second peak (eV)	Third peak (eV)
TiFe01	399.1	402.1
TiFe02	399.1	/
MnFeA02	401.2	/
MnFeA03	/	/
CuFeA	/	/
CuFeB	/	/
CuFeC	399.7	402.2
InFe02	/	/

As stated in the discussion of some of the powders, these binding energies are usually attributed to organic nitrogen. Cataldi et al. [10] discussed the N 1s signal in InHCF thin films: they attributed two extra unexpected peaks at 399.4 eV and 401.8 eV to imidic or amidic nitrogen and their protonated products, respectively. While the former peak was present from the start of the measurement and increased over exposure to X-Ray beams, the latter rose over time. These species were nevertheless regarded as degradation products, mostly due to X-ray irradiation.

Cataldi´s case implies three aspects:

1. The species responsible for the two peaks are related
2. The species are degradation products
3. Prolonged exposure to X-Rays enhances the amount and types of degradation products

In this study, time-dependence should not be taken into account to explain the results, since all measurements were carried out with four scans only.

It is also possible that the species responsible for the peaks are not necessarily related, as only two samples presented a third peak. Contamination is always possible and one of the signals might belong to organic nitrogen from adventitious carbon.

The possibility that the peaks are representative of degradation products must be taken in great consideration, since it may give insight to the material itself and its aging processes. Degradation processes may have taken also place prior to X-ray analysis, probably due to thermal effects – as discussed in Section 4.3.10 in the case of CoNP_05. Heating of PBAs is a very common practice indeed in post-synthesis treatments, in order to remove interstitial and excess water. Partial breakdown of the lattice during further heating, after removal of water, is possible. Lattice vacancies and defects are also always present. These features, if present to a relevant degree in the structure, might give rise to a different signal.

A last hypothesis could be done: extra peaks represent coordination and subdomains in the structure. In fact, the higher E_B of these peaks is representative of a nitrogen atom having less electron density at the core. In the case of TiFe samples – both are displaying a peak at 399.1 eV – it is highly possible that the species for the signal are the same. As Ti/Fe ratio were less or equal to unity, it is possible that water might be coordinated to cyanide nitrogen in lattice vacancies. Being oxygen more electronegative, electron density is taken away from nitrogen – giving rise to a higher binding energy signal.

For MnFeA02 or CuFeC, the case is different, for the ratios M:Fe were much larger than unity. Transition metal ions may be most likely located in the interstices of the structure and the N end of cyanide may consequently be coordinated to two or three transition metal ions. Nitrogen would have more metal centres to share electron density with. This particular coordination mode is named “bifurcated” and was found to exist in MnHCF [69].

Coming to a conclusion is not an easy task, since Table 21 shows that occurrence of extra peaks does not seem to be systematic and constant.

No additional peaks were detected in the analyzed metal nitroprussides. As charge correction was performed on –CN N 1s signal, only resulting –NO N 1s E_B values will be reported: 402.7 eV (reference NaNP), 402.1 eV (CoNP_05) and 402.5 eV (NiNP1).

Finally, the ≡N-M E_B value would be an interesting feature to measure – yet a different reliable signal to perform charge correction on is crucial to this kind of study.

4.3.13 Overview: C 1s signal

A table summarizing all the information concerning the C 1s signal is presented below (Table 22).

Table 22 - C 1s signal: number of peaks and binding energies

	Main peak (eV)	**Second peak (eV)**	**Third peak (eV)**	**Fourth peak (eV)**
TiFe01	284.6	286.2	287.7	289.0
TiFe02	284.7	286.3	288.3	/
MnFeA02	284.5	287.9	/	/
MnFeA03	284.5	/	/	/
CuFeA	284.4	286.1	288.2	/
CuFeB	284.4	/	/	/
CuFeC	284.4	286.1	288.3	/
InFe02	284.2	284.9	/	/

All similar sets of samples presented the same binding energy value for C 1s main peak – namely, the one attributed to cyanide. A trend is noticed: E_B value decreases as metal M atomic number increases.

Electronegativity is a property able to explain several characteristics of metal hexacyanoferrate [83], therefore it might be more interesting to explain the results from that point of view. Pauling´s electronegativity scale values are hereby considered: Ti (1.54), Mn (1.55), Cu (1.90) and In (1.78). Since In's electronegativity value is lower than Cu´s yet the E_B for InHCF is inferior, the following conclusion should be drawn for elements belonging to the same period.

As electronegativity increases along the period, the tendency of a transition metal to remove electron density from the Fe atom through cyanide ligand increases as well. Removing

electron density from Fe weakens the strength of the Fe-C bond, resulting in a lower E_B. This would have also implications in the strength of the ≡N-M bond, which would supposedly be stronger and shifted to a higher E_B. This feature would explain the surprisingly lower E_B values gained for Cu 2p and Fe 2p spectra in CuFe samples or In 3d in InFe02 – therefore confirming that the value to which charge correction was performed (the E_B for N 1s) was not right. In this case, also some C 1s cyanide E_B values would not be accurate – since they were obtained by charge correction on an incorrect value.

Main peaks overlap with adventitious carbon and they are consequently difficult to differentiate. Peak 2 for InFe02 represents an exception, for it is thought to be entirely adventitious carbon: 284.9 eV is very close to 284.8 eV, a value to which charge correction is often performed (also in studies about metal hexacyanoferrates and cyanides [30], [69], [83], [85]). Adventitious carbon would be the best signal to perform charge correction upon as it would enable identification of actual E_B values of both C 1s and N 1s cyanide signals.

All other secondary peaks might be either dirt or peaks related to degradation products of the lattice.

Third peaks are most likely to be oxygen containing dirt, as well as Peak 4 for TiFe01 (the only sample to show a fourth peak in its C 1s signal).

Metal nitroprussides all presented a single peak in the C 1s signal, found at lower binding energies than metal hexacyanoferrates: 284.1 eV (reference NaNP), 283.7 eV (CoNP_05) and 283.8 eV (NiNP1).

Chapter 5
Conclusion

A potentiodynamic method – among several found in literature – was employed to electrodeposit films of NiHCF on Ni-foam as a substrate. Deposition trials were successful and, in contrast with a previous potentiostatic method, reproducibility was improved to a high degree. Performance of such NiHCF films in Oxygen Evolution Reaction (OER) electrocatalysis was tested, both before and after cycling in potassium hydroxide: results showed that the substrate was responsible for the samples' electroactivity. NiHCF deposits actually seemed to decrease the overall performance. Therefore, NiHCF films' electrocatalytic activity could not be evaluated.

XPS was chosen as a structural probe for the electrochemically-synthesized NiHCF. Yet the porous nature of the employed substrate and the amount of deposited material (few monolayers) made the analysis unreliable in terms of quantification of the material itself – as Ni-foam was mainly responsible for the detected signals. However, XPS spectra could provide further proofs of the deposition of the material. The technique was useful in the identification of NiO and $Ni(OH)_2$ as important components of the surface of Ni-foam, which explained and confirmed its remarkable activity in OER electrocatalysis.

Electrosynthesis of NiHCF on a different, non-electroactive and even-surfaced substrate would overcome such drawbacks: OER performance could be related exclusively to NiHCF and the films'composition may be probed with XPS.

In spite of these outcomes, XPS was an optimal technique to gain information about PBA powders, especially oxidation states of metal M and Fe. Quantification of the samples is reliable only for certain elemental ratios, such as M:Fe or Fe:N – yet good fitting and appropriate sensitivity factors are crucial to get valid results. In any case, literature references must be checked to compare values and have further insight.

N 1s signal and C 1s signal often display more peaks than expected. While in C 1s these extra peaks may be attributed to contamination, many hypotheses can be made concerning their nature in N 1s signal. Most probably, these peaks are representative of either coordination chemistry in the lattice or degradation products. XPS alone cannot determine which case is

more likely to be correct. Since XPS probes only the surface, complementary bulk techniques such as XRD or XAS would be valuable in gaining more information concerning this problem. Why extra peaks appear only in one out of more batches of the same analogue is a question that remains open.

Monitoring of the E_B of ≡N-M bond would be a very interesting feature to investigate, yet another reliable signal to perform charge correction on would be necessary. Adventitious carbon in C 1s would be an ideal candidate, as long as the contributions of aliphatic carbon and cyanide can be split and well distinguished.

Bibliography

[1] M. Ware, “Prussian Blue: Artists’ Pigment and Chemists’ Sponge,” *J. Chem. Educ.*, vol. 85, no. 5, p. 612, 2009.

[2] J. F. Keggin and F. D. Miles, “Structure and formulae of the Purssian Blues and related compounds,” *Nature*, no. 137, pp. 577–578, 1936.

[3] A. Mullaliu and M. Giorgetti, “Metal Hexacyanoferrates: Ion Insertion (or Exchange) Capabilities,” *Appl. Ion Exch. Mater. Environ.*, pp. 109–133, 2019.

[4] H. J. Buser, A. Ludi, D. Schwarzenbach, and W. Petter, “The Crystal Structure of Prussian Blue: Fe4[Fe(CN)6]3·xH2O,” *Inorg. Chem.*, vol. 16, no. 11, pp. 2704–2710, 1977.

[5] F. Grandjean, L. Samain, and G. J. Long, “Characterization and utilization of Prussian blue and its pigments,” *Dalt. Trans.*, vol. 45, no. 45, pp. 18018–18044, 2016.

[6] World Health Organization, “WHO Model List of Essential Medicines - 19th List (April 2015),” *Essent. Med.*, 2015.

[7] N. R. De Tacconi, K. Rajeshwar, and R. O. Lezna, “Metal hexacyanoferrates: Electrosynthesis, in situ characterization, and applications,” *Chem. Mater.*, vol. 15, no. 16, pp. 3046–3062, 2003.

[8] M. Ventura *et al.*, “Thin layer films of copper hexacyanoferrate: Structure identification and analytical applications,” *J. Electroanal. Chem.*, vol. 827, no. September, pp. 10–20, 2018.

[9] R. O. Lezna, R. Romagnoli, N. R. De Tacconi, and K. Rajeshwar, “Spectroelectrochemistry of palladium hexacyanoferrate films on platinum substrates,” *J. Electroanal. Chem.*, 2003.

[10] T. R. I. Cataldi, G. E. De Benedetto, and A. Bianchini, “X-ray photoelectron spectroscopic investigation and electrochemistry of polynuclear indium (III) hexacyanoferrate films,” vol. 448, pp. 111–117, 1998.

[11] M. K. Carpenter, R. S. Conell, and S. J. Simko, “Electrochemistry and

Electrochromism of Vanadium Hexacyanoferrate," *Inorg. Chem.,* 1990.

[12] A. B. Bocarsly and S. Sinha, "Chemically-derivatized nickel surfaces: Synthesis of a new class of stable electrode interfaces," *J. Electroanal. Chem.,* 1982.

[13] M. Berrettoni *et al.*, "Synthesis and characterization of nanostructured cobalt hexacyanoferrate," *J. Phys. Chem. C,* 2010.

[14] M. Xie *et al.*, "Sodium titanium hexacyanoferrate as an environmentally friendly and low-cost cathode material for sodium-ion batteries," *J. Power Sources,* 2016.

[15] S. Liu, H. L. Li, M. Jiang, and P. Li, "Platinum hexacyanoferrate: A novel Prussian Blue analogue with stable electroactive properties," *J. Electroanal. Chem.,* vol. 426, no. 1–2, pp. 27–30, 1997.

[16] H. Pang, Y. Zhang, T. Cheng, W. Y. Lai, and W. Huang, "Uniform manganese hexacyanoferrate hydrate nanocubes featuring superior performance for low-cost supercapacitors and nonenzymatic electrochemical sensors," *Nanoscale,* 2015.

[17] J. Joseph, H. Gomathi, and G. P. Rao, "Modification of carbon electrodes with zinc hexacyanoferrate," *J. Electroanal. Chem.,* 1997.

[18] P. Wu, S. Lu, and C. Cai, "Electrochemical preparation and characterization of a samarium hexacyanoferrate modified electrode," *J. Electroanal. Chem.,* 2004.

[19] H. Yang, B. Lu, L. Guo, and B. Qi, "Cerium hexacyanoferrate/ordered mesoporous carbon electrode and its application in electrochemical determination of hydrous hydrazine," *J. Electroanal. Chem.,* 2011.

[20] B. Devadas, M. Rajkumar, S. M. Chen, and R. Saraswathi, "Electrochemically reduced graphene oxide/ Neodymium hexacyanoferrate modified electrodes for the electrochemical detection of paracetomol," *Int. J. Electrochem. Sci.,* 2012.

[21] X. Cui, L. Hong, and X. Lin, "Electrochemical preparation, characterization and application of electrodes modified with hybrid hexacyanoferrates of copper and cobalt," *J. Electroanal. Chem.,* vol. 526, no. 1–2, pp. 115–124, 2002.

[22] A. Safavi, S. H. Kazemi, and H. Kazemi, "Electrochemically deposited hybrid nickel-cobalt hexacyanoferrate nanostructures for electrochemical supercapacitors,"

Electrochim. Acta, 2011.

[23] P. J. Kulesza *et al.*, “Electrochemical preparation and characterization of electrodes modified with mixed hexacyanoferrates of nickel and palladium,” *J. Electroanal. Chem.*, 2000.

[24] J. H. Lee, G. Ali, D. H. Kim, and K. Y. Chung, “Metal-Organic Framework Cathodes Based on a Vanadium Hexacyanoferrate Prussian Blue Analogue for High-Performance Aqueous Rechargeable Batteries,” *Adv. Energy Mater.*, 2017.

[25] H. Tokoro and S. I. Ohkoshi, “Novel magnetic functionalities of Prussian blue analogs,” *Dalt. Trans.*, vol. 40, no. 26, pp. 6825–6833, 2011.

[26] J. Jiménez-Gallegos, J. Rodrýguez-Hernández, H. Yee-Madeira, and E. Reguera, “Structure of porous copper prussian blue analogues: Nature of their high H2 storage capacity,” *J. Phys. Chem. C*, vol. 114, no. 11, pp. 5043–5048, 2010.

[27] S. Zamponi *et al.*, “Influence of experimental conditions on electrochemical behavior of Prussian blue type nickel hexacyanoferrate film,” *Electrochim. Acta*, vol. 48, no. 28, pp. 4261–4269, 2003.

[28] C. D. Wessells, R. A. Huggins, and Y. Cui, “Copper hexacyanoferrate battery electrodes with long cycle life and high power,” *Nat. Commun.*, vol. 2, no. 1, pp. 550–555, 2011.

[29] A. A. Karyakin, “Prussian blue and its analogues: Electrochemistry and analytical applications,” *Electroanalysis*. 2001.

[30] A. Cano, L. Lartundo-Rojas, A. Shchukarev, and E. Reguera, “Contribution to the coordination chemistry of transition metal nitroprussides: A cryo-XPS study,” *New J. Chem.*, 2019.

[31] A. Mullaliu *et al.*, “The electrochemical activity of the nitrosyl ligand in copper nitroprusside: a new possible redox mechanism for lithium battery electrode materials?,” *Electrochim. Acta*, vol. 257, pp. 364–371, 2017.

[32] P. Coppens, I. Novozhilova, and A. Kovalevsky, “Photoinduced Linkage Isomers of Transition-Metal Nitrosyl Compounds and Related Complexes,” *Chem. Rev.*, 2002.

[33] M. D. Carducci, M. R. Pressprich, and P. Coppens, “Diffraction studies of photoexcited crystals: Metastable nitrosyl-linkage isomers of sodium nitroprusside,” *J. Am. Chem. Soc.*, vol. 119, no. 11, pp. 2669–2678, 1997.

[34] C. Loos-Neskovic, M. Fedoroff, E. Garnier, and P. Gravereau, “Zinc and nickel ferrocyanides: preparation, composition and structure,” *Talanta*, 1984.

[35] W. A. Steen and D. T. Schwartz, “A route to diverse combinatorial libraries of electroactive nickel hexacyanoferrate,” *Chem. Mater.*, 2003.

[36] X. Hao, Y. Li, and M. Pritzker, “Pulsed electrodeposition of nickel hexacyanoferrate films for electrochemically switched ion exchange,” vol. 63, pp. 407–414, 2008.

[37] J. Joseph, H. Gomathi, and G. Prabhakara Rao, “Electrochemical characteristics of thin films of nickel hexacyanoferrate formed on carbon substrates,” *Electrochim. Acta*, vol. 36, no. 10, pp. 1537–1541, 1991.

[38] Y. Wang, Y. Rui, F. Li, and M. Li, “Electrodeposition of nickel hexacyanoferrate/layered double hydroxide hybrid film on the gold electrode and its application in the electroanalysis of ascorbic acid,” *Electrochim. Acta*, 2014.

[39] S. Chen, “Preparation , characterization , and electrocatalytic oxidation properties of iron , cobalt , nickel , and indium hexacyanoferrate,” vol. 521, pp. 29–52, 2002.

[40] Y. Lin and X. Cui, “Electrosynthesis , characterization , and application of novel hybrid materials based on carbon nanotube – polyaniline – nickel hexacyanoferrate nanocomposites,” pp. 585–592, 2006.

[41] S. Zamponi *et al.*, “Influence of experimental conditions on electrochemical behavior of Prussian blue type nickel hexacyanoferrate film,” *Electrochim. Acta*, 2003.

[42] C. Loos-Neskovic, M. Fedoroff, and E. Garnier, “Preparation, composition and structure of some nickel and zinc ferrocyanides: Experimental results,” *Talanta*, 1989.

[43] S. Tang, L. Li, H. Ren, Q. Lv, and R. Lv, “Sodium-ion electrochemical tuning of Prussian blue analog as an efficient oxygen evolution catalyst,” *Mater. Today Chem.*, 2019.

[44] W. A. Steen *et al.*, “Structure of cathodically deposited nickel hexacyanoferrate thin

films using XRD and EXAFS," *Langmuir*, vol. 18, no. 20, pp. 7714–7721, 2002.

[45] B. Wang *et al.*, "Prussian Blue Analogs for Rechargeable Batteries," *iScience*, 2018.

[46] A. Mullaliu *et al.*, "Copper Electroactivity in Prussian Blue-Based Cathode Disclosed by Operando XAS," *J. Phys. Chem. C*, vol. 122, no. 28, pp. 15868–15877, 2018.

[47] P. J. Kulesza, M. A. Malik, S. Zamponi, M. Berrettoni, and R. Marassi, "Electrolyte-cation-dependent coloring, electrochromism and thermochromism of cobalt(II) hexacyanoferrate(III, II) films," *J. Electroanal. Chem.*, 2002.

[48] M. Giorgetti, D. Tonelli, M. Berrettoni, G. Aquilanti, and M. Minicucci, "Copper hexacyanoferrate modified electrodes for hydrogen peroxide detection as studied by X-ray absorption spectroscopy," *J. Solid State Electrochem.*, vol. 18, no. 4, pp. 965–973, 2014.

[49] C. C. Chusuei and D. W. Goodman, "X-Ray Photoelectron Spectroscopy.pdf." Encyclopedia of Physical Science and Technology, pp. 921–938, 2002.

[50] S. Hoffmann, "Surface and interface analysis," in *Kirk-Othmer Encyclopedia of Chemical Technology*, Wiley, 2016, pp. 1–48.

[51] J. F. Moulder, W. F. Stickle, P. E. Sobol, and K. D. Bomben, *Handbook of X-ray Photoelectron Spectroscopy*. Perkin-Elmer Corporation, 1992.

[52] M. Giorgetti, "Lecture notes." .

[53] A. J. Bard and L. R. Faulkner, *Electrochemical methods*, Second Edi. Wiley, 2001.

[54] N.-T. Suen, S.-F. Hung, Q. Quan, N. Zhang, Y.-J. Xu, and H. M. Chen, "Electrocatalysis for the oxygen evolution reaction: recent development and future perspectives.," *Chem. Soc. Rev.*, 2017.

[55] B. E. Conway and T. C. Liu, "Characterization of Electrocatalysis in the Oxygen Evolution Reaction at Platinum by Evaluation of Behavior of Surface Intermediate States at the Oxide Film," *Langmuir*, 1990.

[56] V. I. Birss and A. Damjanovic, "Oxygen Evolution at Platinum Electrodes in Alkaline Solutions," *J. Electrochem. Soc.*, 1987.

[57] M. Gong and H. Dai, “A mini review of NiFe-based materials as highly active oxygen evolution reaction electrocatalysts,” *Nano Research*. 2014.

[58] D. A. Corrigan, “The Catalysis of the Oxygen Evolution Reaction by Iron Impurities in Thin Film Nickel Oxide Electrodes,” *J. Electrochem. Soc.*, 2006.

[59] M. W. Louie and A. T. Bell, “An investigation of thin-film Ni-Fe oxide catalysts for the electrochemical evolution of oxygen,” *J. Am. Chem. Soc.*, 2013.

[60] C. C. L. McCrory, S. Jung, J. C. Peters, and T. F. Jaramillo, “Benchmarking heterogeneous electrocatalysts for the oxygen evolution reaction,” *J. Am. Chem. Soc.*, 2013.

[61] A. Laurita, “Elettrosintesi di Nickel esacianoferrato e suo impiego per la cattura del Cesio,” Alma Mater Studiorum University di Bologna, 2016.

[62] K. B. Yatsimirskii, V. V. Nemoshkalenko, Y. P. Nazarenko, V. G. Aleshin, V. V. Zhilinskaya, and N. A. Tomashevsky, “Use of X-ray photoelectron and Mössbauer spectroscopies in the study of iron pentacyanide complexes,” *J. Electron Spectros. Relat. Phenomena*, 1977.

[63] N. Vannerberg, “Esca-spectra of sodium and potassium cyanide and of sodium and potassium-salts of hexacyanometallates of 1st transition-metal series,” *Chem. Spricta*, 1976.

[64] I. G. Casella, M. Gatta, D. Chimica, and V. N. Sauro, “Electrochemical and XPS Characterization of Composite Modified Electrodes Obtained by Nickel Deposition on Noble Metals,” vol. 72, no. 13, pp. 2969–2975, 2000.

[65] X. Hao, D. T. Schwartz, R. V July, V. Re, M. Recei, and V. September, “Tuning Intercalation Sites in Nickel Hexacyanoferrate Using Lattice Nonstoichiometry,” no. 7, pp. 5831–5836, 2005.

[66] Y. Wang, Y. Rui, F. Li, and M. Li, “Electrochimica Acta Electrodeposition of nickel hexacyanoferrate / layered double hydroxide hybrid film on the gold electrode and its application in the electroanalysis of ascorbic acid,” *Electrochim. Acta*, vol. 117, pp. 398–404, 2014.

[67] T. R. I. Cataldi, R. Guascito, and A. M. Salvi, “XPS study and electrochemical behaviour of the nickel hexacyanoferrate film electrode upon treatment in alkaline solutions,” vol. 417, pp. 83–88, 1996.

[68] D. E. Ciurduc, “Electrodeposition of actives species on carbonaceous materials for energy applications,” Alma Mater Studiorum University of Bologna, 2017.

[69] A. Cano, J. Rodríguez-Hernández, L. Reguera, E. Rodríguez-Castellón, and E. Reguera, “On the Scope of XPS as Sensor in Coordination Chemistry of Transition Metal Hexacyanometallates,” *Eur. J. Inorg. Chem.*, 2019.

[70] A. P. Grosvenor, B. A. Kobe, M. C. Biesinger, and N. S. Mcintyre, “Investigation of multiplet splitting of Fe 2p XPS spectra and bonding in iron compounds,” no. October, pp. 1564–1574, 2004.

[71] M. Oku, K. Wagatsuma, and H. Matsuta, “Background subtraction from transition metal 2p XPS by deconvolution using ligand atom XPS : study on first transition metal cyanide complexes,” vol. 83, pp. 31–39, 1997.

[72] H. Konno, K. Sasaki, M. Tsunekawa, T. Takamori, and R. Furuichi, “X-Ray photoelectron spectroscopic analysis of surface products on pyrite formed by baterial leaching.,” *Bunseki kagaku*, 2011.

[73] M. Oku, “X-Ray Photoelectron Spectroscopic Studies on the Kinetics of Photoreduction of FeIII in Single-crystal K3(Fe,Co)(CN)6 Surfaces cleaved in situ,” *J. Chem. Soc. Fraday Trans.*, vol. 89, no. 4, pp. 743–748, 1993.

[74] M. Oku, H. Matsuta, and K. Wagatsuma, “Chemical change of nitrosylpentacyanoferrate (II) during XPS measurements : Identification of the irradiated product by DV-Xa molecular orbital calculations,” vol. 93, pp. 1061–1063, 1997.

[75] H. W. Lee, R. Y. Wang, M. Pasta, S. W. Lee, N. Liu, and Y. Cui, “Manganese hexacyanomanganate open framework as a high-capacity positive electrode material for sodium-ion batteries,” *Nat. Commun.*, 2014.

[76] Y. Wang, H. Zhong, L. Hu, N. Yan, H. Hu, and Q. Chen, “Manganese hexacyanoferrate/MnO 2 composite nanostructures as a cathode material for

supercapacitors," *J. Mater. Chem. A*, 2013.

[77] R. Agarwal, M. K. Sharma, and K. Bhattacharyya, "Prussian Blue-Manganese Hexacyanoferrate Nanocomposite as Multifunctional High Performance Electrode Material," *ChemistrySelect*, 2016.

[78] X. Sun *et al.*, "A new gridding cyanoferrate anode material for lithium and sodium electrochemical properties," *J. Power Sources*, vol. 314, pp. 35–38, 2016.

[79] Y. Luo, B. Shen, B. Guo, L. Hu, Q. Xu, and R. Zhan, "Potassium titanium hexacyanoferrate as a cathode material for potassium- ion batteries," *J. Phys. Chem. Solids*, vol. 122, no. January, pp. 31–35, 2018.

[80] M. C. Biesinger, L. W. M. Lau, A. R. Gerson, R. St, and C. Smart, "Resolving surface chemical states in XPS analysis of first row transition metals , oxides and hydroxides : Sc , Ti , V , Cu and Zn," *Appl. Surf. Sci.*, vol. 257, no. 3, pp. 887–898, 2010.

[81] E. Musella, "Surface dynamic of copper nitroprusside as a cathode material: observation by XPS and SEM," Alma Mater Studiorum University di Bologna, 2017.

[82] X. Ma, W. Jia, J. Wang, J. Zhou, Y. Wu, and Y. Wei, "Synthesis of copper hexacyanoferrate nano fl ake as a cathode for sodium-ion batteries," *Ceram. Int.*, vol. 45, no. 1, pp. 740–746, 2019.

[83] S. J. Gerber and E. Erasmus, "Electronic effects of metal hexacyanoferrates: An XPS and FTIR study," *Mater. Chem. Phys.*, vol. 203, pp. 73–81, 2018.

[84] H. Wu, J. Hu, H. Li, and H. Li, "A novel photo-electrochemical sensor for determination of hydroquinone based on copper hexacyanoferrate and platinum films modified n-silicon electrode," *Sensors Actuators B. Chem.*, vol. 182, pp. 802–808, 2013.

[85] A. Cano, Y. Avila, M. Avila, and E. Reguera, "Structural information contained in the XPS spectra of nd10 metal cyanides," *J. Solid State Chem.*, 2019.